FREE ENERGY MINIMIZATION AND MULTICOMPONENT, MULTI-PHASE LATTICE

BOLTZMANN SIMULATIONS OF VAN DER WAALS FLUID MIXTURES

A Thesis
Submitted to the Graduate Faculty
of the
North Dakota State University
of Agriculture and Applied Science

By

Kent Stephen Ridl

In Partial Fulfillment of the Requirements
for the Degree of
MASTER OF SCIENCE

Major Department:
Physics

April 2018

Fargo, North Dakota

NORTH DAKOTA STATE UNIVERSITY

Graduate School

Title

FREE ENERGY MINIMIZATION AND MULTICOMPONENT, MULTI-PHASE

LATTICE BOLTZMANN SIMULATIONS OF VAN DER WAALS FLUID

MIXTURES

By

Kent Stephen Ridl

The supervisory committee certifies that this thesis complies with North Dakota State University's regulations and meets the accepted standards for the degree of

MASTER OF SCIENCE

SUPERVISORY COMMITTEE:

Dr. Alexander Wagner
Chair

Dr. Alan Denton

Dr. Erik Hobbie

Dr. Yildirim Bora Suzen

Approved:

April 13, 2018	Dr. Sylvio May
Date	Department Chair

ABSTRACT

In this thesis, we develop a general framework for the lattice Boltzmann method to simulate multiphase systems with an arbitrary number of components. Theoretical expectations are easily visualized for binary mixtures, so we focus on characterizing the performance of the method by numerically minimizing the free energy of a binary van der Waals mixture to generate phase diagrams. Our phase diagrams contain very intriguing features that are not well-known in today's physics community but were understood by van der Waals and his colleagues at the turn of the 20th century. Phase diagrams and lattice Boltzmann simulation results are presented in a density-density plane, which best matches with LB simulations performed at constant volume and temperature. We also demonstrate that the algorithm provides thermodynamically consistent results for mixtures with larger numbers of components and high density ratios. All of the theoretical phase diagrams are recovered well by our lattice Boltzmann method.

ACKNOWLEDGEMENTS

TABLE OF CONTENTS

LIST OF FIGURES

LIST OF APPENDIX FIGURES

1. INTRODUCTION

The lattice Boltzmann (LB) method has steadily gained a reputation in the last two decades as a simple, efficient algorithm with which a wide variety of fluid dynamics problems may be modelled. As LB has gained acceptance, the evolution of the method has been driven in a direction requiring accuracy for non-equilibrium models that simulate both multiple phases and multiple components. One such early LB application used a mixture of van der Waals fluids to look at the condensation of a gas of two components into a dendritic structure of alternating fluid phases [5]. Our interest in the development of this method lies in evaporation phenomena and the effects that can occur when a change in concentration introduces phase separation fronts [6].

The development of multicomponent, multiphase methods began shortly after the introduction of lattice Boltzmann methods by McNamara et al. in 1988 [7]. There are three main categories of multiphase and multicomponent models, and other models can be generated by combining the underlying principles of these main types. The first is based on the lattice gas method by Gunstensen and Rothmann [8]. This method focuses on achieving maximal phase-separation of nearly immiscible fluids; however, its use has waned in recent years.

A second class of multiphase, multicomponent model was proposed by Shan and Chen [9] and was a straightforward extention of their "bottom-up" pseudo-potential implementation for single-component fluids. Although this method was shown early on that it can recover accurate diffusive behavior [10], it and its extensions do not address thermodynamic consistency in a natural way, i.e. equality of pressure and chemical potentials for each component in equilibrium.

An offshoot of pseudo-potential LB models that attempts to build in thermodynamic consistency is based on the minimization of an H-theorem [11, 12], which was recently extended to include multiphase behavior [13]. However, while this model was is important step towards simulating more realistic mixtures at higher Reynolds numbers, the additional complexity sometimes requires abandoning thermodynamic consistency in favor of computational simplicity.

In addition to issues with consistent thermodynamics, the models referenced above and the majority of others are based on mixtures of ideal fluids [14, 15, 16, 17]. Non-ideal behavior of mixture components is generally included by construction of a non-realistic equation of state.

1

A third class of LB simulations developed by Swift, Orlandini, and Yeomans provides inherent thermodynamic consistency are those based on the minimization of an underlying free energy [18, 19]. When a free energy functional can be defined, non-ideal behavior is a natural consequence of the realistic equations of state [20, 21]. However, inaccuracies can still arise, particular along phase interfaces when phase separation occurs far away from the critical point [22], and the models suffer from numerical stability issues.

In this thesis we introduce a LB method for multicomponent, multiphase applications which is based on the approach of [23]. It combines the thermodynamic corrections of [22] with a basic application of the findings from [24] to increase numerical stability and the range of accessible density ratios. With an eye towards eventual application, we focus first on establishing the appropriateness of our approach to recover the complex phase behavior of these mixtures, since the recovery of equilibrium behavior is a necessary condition of recovering the correct non-equilibrium behavior.

We make no assumptions about the ideality of any part of a mixture by making use the free energy for a mixture of van der Waals (VDW) fluids. Although other free energies with more degrees of freedom that allow for a better fit to specific experimental data, we focus on the generic multicomponent, multiphase behavior. Even for a simple mixture of van der Waals fluids with their restricted parameters, a remarkably complex set of phenomena can be recovered.

1.1. Preview of Results

To validate our method we separately minimized the underlying free energy to generate predictions for the phase diagrams representing several mixtures of two VDW fluids. We generated our phase diagrams in a density-density plane, which is not typical of most literature, and map our phase diagrams to the common nomenclature of van Konynenburg and Scott [25, 26].

The resulting phase diagrams show an interesting variety of structures from the simple generalization of the one component case to much more complicated phase diagrams that include asymmetric three-phase behavior. We also describe a prediction of metastable behavior defined by branches formed by the intersection of binodals in a density-density plane.

Although several literature searches failed to turn up modern descriptions of the phase diagram structures we observed, it turned out that much of this complexity was already understood by van der Waals and co-workers around the turn of the 20th century. But the interest of physicists turned to a different direction after that time, and much of this knowledge had been lost in the

physics community. Most modern studies of such fluid mixtures was often restricted to chemistry and chemical process engineering [25, 26], which do not contain descriptions of the phase behavior we observed. However, we found a recent book by Sengers [3, 27] and several papers by Meijer [28, 29, 30, 31, 32, 33] extremely enlightening. We then realized that much of our free energy minimization work consisted of re-discovering results that were already known at the beginning of the 20th century.

As in the previous work by Wagner [24], our simulations achieve high density ratios at the cost of execution speed. We also show a straightforward extension to a three component VDW mixture with four allowed phases that recovers consistent thermodyamics and density ratios near 1700, although we do not attempt to generate generic phase diagrams for more than two components.

1.2. Thesis Structure

This thesis is structured as follows. Chapter 2 develops the background thermodynamics and statistical mechanics that is necessary to understanding the behavior of a phase-separating fluid. The chapter starts by describing the continuum theory of a single component and extends the case in a general manner to mixtures composed of multiple components. Because of the standard application of LB methods to isothermal systems, we focus on the statistical mechanics of the canonical ensemble. The discretization of the corresponding multicomponent theory is then reviewed.

Chapter 3 next covers the minimization of an underlying free energy. We start the discussion from the well-known thermodynamic concept of Maxwell's common tangent construction for a single component. The two-dimensional free energy curve on which the common tangent construction is based is then extended to a three-dimensional free energy surface applicable to a binary mixture, and the common tangent is extended to a tangent plane concept. The theory of stability of binary mixtures on the free energy surface is briefly reviewed, and the concepts are brought together in a description of the free energy minimization algorithm used in this thesis. The chapter concludes with a description of the binary mixture phase diagrams that serve as theoretical predictions to which the performance of our LB model can be compared.

Chapter 4 covers the theory behind LB methods. Starting from kinetic theory concepts, we develop the formalism that shows how the evolution of a mesoscopic particle probability density

is equivalent to the well-known macroscopic governing equations of fluid flow. Once this link is established, we show how to discretize the results to obtain expressions that are able to be implemented in computer code. Chapter 5 covers the implementation of our D1Q3 LB model, so named as it implements 3 discrete velocity vectors on top of a 1-dimensional lattice.

Finally, Chapter 6 discusses the results of our simulations. We show that for a large variety complex phase diagrams the two methods give near identical results, even when we have large density ratios between different phases. We relate our results back to the common nomenclature of van Konynenburg and Scott [25, 26], which is widely used in chemistry and chemical engineering. Multiple three-phase regions are recovered, and even metastable regions are recovered. Alone the elusive four-phase point eluded a recovery by our LB method. This demonstrates that our lattice Boltzmann method is able to recover complex phase behavior with good accuracy and is a promising candidate to investigate novel non-equilibrium behavior [6].

1.3. Notes on Reading this Thesis

As I was learning the theory behind the lattice Boltzmann method, I found that it was very easy for me to lose sight of what space a particular derivative was taken over (i.e. position derivative, velocity derivative, etc.). This confusion was greatly exacerbated by the need for tensor notation in certain instances. In the hopes of helping preserve clarity, the following notation is adopted:

$$\partial_t \equiv \frac{\partial}{\partial t} \qquad \text{partial derivative with respect to time}$$

$$\nabla_\alpha \equiv \left(\frac{\partial}{\partial x}, \frac{\partial}{\partial y}, \frac{\partial}{\partial z} \right) \qquad \text{spatial gradient}$$

$$\partial_{v_\alpha} \equiv \left(\frac{\partial}{\partial v_x}, \frac{\partial}{\partial v_y}, \frac{\partial}{\partial v_z} \right) \qquad \text{velocity gradient}$$

In Chapter 2, we use standard vector notation when necessary. However, from Chapter 4 on, we make a transition to the use of tensor notation. I still have a hard time processing changes in notation, so this was intentionally done in the hopes that a natural transition point in the thesis material would help the reader to make a smoother transition than I was able to.

In tensor notation, position and velocity vectors take the form of a tensor of 1st rank

$$\vec{r} \equiv r_\alpha \qquad \vec{v} \equiv v_\alpha$$

where Greek subscripts denote spatial components ($\alpha \in \{x, y, z\}$), and the number of subscripts denote the rank of the tensor (i.e. scalars are zero rank tensors, vectors are 1st rank tensors). Repeated Greek indicies imply summation, the so-called Einstein notation. The most common application of this is for the calculation of a dot product, for example

$$\vec{u}.\vec{v} = \sum_{\alpha} u_\alpha v_\alpha \equiv u_\alpha v_\alpha$$

Notation where a vector is "squared" implies a scalar value - the vector's magnitude - is squared. For example

$$u^2 \equiv |u_\alpha|^2 = u_\alpha u_\alpha$$

"Multiplying" vectors with different Greek indices is equivalent to an outer product, which results in a matrix. A general example is

$$v_\alpha v_\beta \equiv V_{\alpha\beta}$$

where the example matrix V is a tensor of 2nd rank. The representation of this kind of tensor was introduced for the derivation of the pressure tensor in Section 2.1.1.3.

The evaluation of an expression with repeated Greek indices in tensor notation consists of contracting/eliminating the like Greek indices. In this example, the index β is contracted when we multiply a tensor of 1st rank (a force vector) by a tensor of 2nd rank, where the Kornecker delta is used to denote a general identity matrix

$$F_\beta \delta_{\alpha\beta} = F_\alpha; \qquad \text{where,} \quad \delta_{\alpha\beta} = \begin{cases} 1, & \alpha = \beta \\ 0, & \alpha \neq \beta \end{cases} \tag{1.1}$$

The letter c is overloaded in its use. When used as a subscript (e.g. θ_c), it is in reference to a critical thermodynamic property of a fluid. When used as a superscript (e.g. $\kappa^{cc'}$), it is a general identifier for a component in a multicomponent mixture.

Specific to the van der Waals constant a for a binary mixture, we use superscripts such as $a^A \equiv a^{AA}$ to reference component A interacting with itself and a^{AB} for an A-B interaction. Self-interactions are almost always written with the notational simplification a^A, a^B.

Finally, when the thesis moves into the discussion of multicomponent mixtures, the nested summations over all of the pairs of components of a mixture get cumbersome. In the binary mixture case - since that is the focus of this thesis - we define our components to be $c \in \{A, B\}$. We apply superscripts c, c' to distinguish different components in a sum, such as

$$\sum_c \sum_{c'} n^c b^{cc'}$$

In principle, an expression such as this does not prohibit c and c' from being equal. When $c = c'$, it represents a component interacting with itself; when $c \neq c'$, it represents a component interacting with another component. This is always true when a summation is explicitly written.

Occasionally self-component and cross-component interactions are written about generally. When a point is made that distinguishes between self- and cross-component traits, we occasionally use the apostrophe to differentiate a self-component property from the corresponding cross-component property. For example, the van der Waals energy constant for a general self-interaction is written as a^{cc} where c is taken to be any component from the set of all components that make up a mixture (e.g. A-A interaction or B-B interaction for a binary mixture). The general cross-component interaction parameter would be written as $a^{cc'}$, which is the A-B (or equivalently B-A) interaction in a binary mixture.

2. THERMODYNAMICS AND STATISTICAL MECHANICS OF INTERACTING FLUIDS

2.1. Continuous Theory

To establish the thermodynamics of our model, we begin with the single component case in a continuum fluid. Our model will be developed statistically for a notional macroscopic system with volume V by applying a mean field energy approximation. We then take the model in the global sense and reduce it to a local sense, which is a key concept to the free energy minimization that will follow. After establishing the continuum theory for a single component, we shall extend the treatment to multiple components.

2.1.1. Single Component

The statistical mechanics of any interacting fluid may be determined by proper manipulation of a partition function in the form [1, 34, 35]

$$\mathcal{Z} = \frac{1}{N!h^{3N}} \int_{\vec{p}^N} \int_{\vec{r}^N} e^{-\beta H(\vec{r}^N, \vec{p}^N)} d\vec{p}^N d\vec{r}^N \tag{2.1}$$

where the integrals collectively extend over all of phase space for N particles ($\vec{p}^N \equiv \vec{p_1}, \vec{p_2}, ..., \vec{p_N}$ and $\vec{r}^N \equiv \vec{r_1}, \vec{r_2}, ..., \vec{r_N}$), $\beta = (k_B T)^{-1}$, h is the Planck constant, the Hamiltonian $H(\vec{r}^N, \vec{p}^N)$ applies to all N particles in our volume V, and the Gibbs correction for indistinguishable particles $(1/N!)$ has been applied. The art of evaluating this partition function starts with constructing the Hamiltonian.

As with all Hamiltonians, this one is composed of kinetic and potential energies ($H = K + U$), but we assume there are no external potentials for this analysis. The kinetic energy term for each particle is well-known and is a function of the momentum of a particle $\vec{p}$, and we sum these momenta over all N particles. The potential energy term for a single particle is constructed by interactions among all pairs of particles and is thus a function of the positions of all N particles. The double sum below ensures all particles are accounted for and each particle pair is counted only

once. The pair interaction $u(\vec{r_{ij}})$ depends on the separation between particles of a given pair $(\vec{r_{ij}})$

$$K(\vec{p^n}) = \sum_{i=1}^{N} \frac{\vec{p_i}^2}{2m}; \qquad U(\vec{r}^N) = \sum_{i=1}^{N} \sum_{j=i+1}^{N} u(\vec{r_{ij}}); \qquad \vec{r_{ij}} = \vec{r_i} - \vec{r_j} \qquad (2.2)$$

The lattice Boltzmann simulations presented later in this thesis were conducted in an isothermal environment with fixed particle counts and volume, which makes treatment in the canonical ensemble appropriate. In the canonical ensemble where the particle count N, volume V, and temperature T are held constant, the numerous pair interactions are accounted for by averaging over the entire ensemble

$$\langle U(\vec{r}^N) \rangle = \frac{\int U(\vec{r}^N) e^{-\beta U(\vec{r}^N)} d\vec{r}^N}{\int e^{-\beta U(\vec{r}^N)} d\vec{r}^N} \qquad (2.3)$$

Since the momenta and configuration of the particles are separated into the kinetic and potential energy terms respectively, the denominator of the mean-field approximation for the potential depends only on the configuration of the fluid. This integral is the configurational partition function (Z_U).

$$Z_U = \int e^{-\beta U(\vec{r}^N)} d\vec{r}^N \qquad (2.4)$$

We wish for our model to account for phase coexistence. While in a global, macroscopic sense a fluid that has separated into multiple phases is not isotropic, in a local, microscopic sense it is. In an fluid that is locally isotropic, the average energy can be greatly simplified by considering a single reference pair of particles separated by distance $\vec{r_{12}}$ with interaction energy $u(\vec{r_{12}})$. All particle pairs in such an isotropic, mean-field situation have the same interaction energy, so after substituting the potential energy from Eq. (2.2) into Eq. (2.3), the double sum in the integral may be replaced by simply scaling by the number of particle pairs in the fluid corrected for double-counting $[\frac{1}{2}N(N-1)]$:

$$\langle U(\vec{r}^N) \rangle = \frac{\int (\sum_{i=1}^{N} \sum_{j=i+1}^{N} u(\vec{r_{12}})) e^{-\beta U(\vec{r}^N)} d\vec{r}^N}{Z_U}$$

$$= \underbrace{\frac{1}{2}N(N-1)}_{\text{number of particle pairs}} \underbrace{\frac{\int u(\vec{r_{12}}) e^{-\beta U(\vec{r}^N)} d\vec{r}^N}{Z_U}}_{\text{mean potential of a single pair}} \qquad (2.5)$$

8

At this point, we pause to recall a few probability definitions [36] that will be necessary to proceed further from Eq. (2.5). The probability of anything in the canonical ensemble is a Boltzmann factor divided by a partition function. In working with just the potential energy portion of the Hamilitonian, the configurational partition function of Eq. (2.4) is appropriate for our probability, so we have

$$P(\vec{r}^N) = \frac{e^{-\beta U(\vec{r}^N)}}{Z_U} \tag{2.6}$$

as the probability of finding a volume with N specific distinguishable particles in a particular spatial configuration given by $\vec{r}^N$. By definition, integrating Eq. (2.6) over all of coordinate space equals 1. Since we approximate the potential with interactions between pairs, we need only concern ourselves with a joint probability of just 2 particles. This is given by

$$P^{(2)}(\vec{r_1}, \vec{r_2}) = \frac{\int e^{U(\vec{r}^N)} d\vec{r}_3 d\vec{r}_4 ... d\vec{r}_N}{Z_U} = \frac{\int e^{-\beta U(\vec{r}^N)} d\vec{r}^{N-2}}{Z_U} \tag{2.7}$$

where since we are only concerned with "Particle 1" and "Particle 2" specifically, we can integrate out the coordinates of the remaining particles $\{3, 4, ..., N\}$. While particles in our model at this point are still distinguishable, we don't care which particle is designated "Particle 1" and which is designated "Particle 2." This allows us to correct Eq. (2.7) by a permutation factor to define

$$\rho^{(2)}(\vec{r_1}, \vec{r_2}) = N(N-1)P^{(2)}(\vec{r_1}\vec{r_2}) \tag{2.8}$$

Note that since the correction for double counting is applied in Eq. (2.5) and the Gibbs correction for indistinguishable particles is applied in Eq. (2.20), we need not worry about those here.

If we assume that the two particles we choose are independent and hence uncorrelated in probability, such as in the treatment of an ideal fluid, the joint probability distribution in Eq. (2.8) is separable into the product of two general single-particle distributions

$$\rho^{(2)}(\vec{r_1}, \vec{r_2}) \rightarrow \rho^{(1)}(\vec{r_1})\rho^{(1)}(\vec{r_2}) = NP^{(1)}(\vec{r_1})(N-1)P^{(1)}(\vec{r_2}) \tag{2.9}$$

where $P^{(1)}$ is defined similarly to Eq. (2.7) with the exception that it is integrated over an additional particle $(d\vec{r}^{N-1})$.

To allow for non-ideal behavior, we define a local density with a length scale δx that is far greater than the length scale of a density fluctuation ξ ($\delta x >> \xi$) yet small enough to resolve the width of an interface between densities w ($\delta x << w$). Within the control volume defined by δx we can treat the fluid as an isotropic ideal fluid with a constant density such that $\rho^{(1)}(\vec{r}) = \rho(\vec{r})$. The local density is defined via the single-particle probability distribution $P^{(1)}$

$$\rho(\vec{r}) = NP^{(1)}(\vec{r}) \tag{2.10}$$

Combining Eq. (2.8) with Eq. (2.9) allows the definition of a pair correlation function, also known as a radial distribution function, which measures how "much" a fluid deviates from ideal behavior within the scope of our control volume

$$g(\vec{r_{12}}) = \frac{\rho^{(2)}(\vec{r_1}, \vec{r_2})}{\rho(\vec{r_1})\rho(\vec{r_2})} \tag{2.11}$$

We note that this expression for $g(\vec{r_{12}})$ is defined with respect to the local densities around two reference particles, $\vec{r_1}$ and $\vec{r_2}$, and since we assume isotropy in a volume element, the separation between these particles $\vec{r_{12}}$ is what drives the correlation between them.

With our probability concepts defined, we can now return to Eq. (2.5). By choosing our "Particle 1" and "Particle 2", we can redefine Eq. (2.5) in terms of the integral over the positions of only those two particles. Algebraic manipulation of the permutation factor $N(N-1)$ allows us to re-cast the ensemble average energy in terms of the pair distribution function $g(\vec{r_{12}})$, which reveals more clearly the dependence on the structure of the interacting fluid:

$$\langle U(\vec{r}^N) \rangle = \frac{1}{2} \int \int u(\vec{r_{12}}) N(N-1) \frac{\int e^{-\beta U(\vec{r}^N)} d\vec{r}^{N-2}}{Z_U} d\vec{r_1} d\vec{r_2}$$
$$= \frac{1}{2} \int \int u(\vec{r_{12}}) \rho(\vec{r_1}) \rho(\vec{r_2}) g(\vec{r_{12}}) d\vec{r_1} d\vec{r_2} \tag{2.12}$$

The expected potential energy given by Eq. (2.12) is for a globally inhomogeneous fluid, i.e. one that has phase separated. Yet, it isn't clear how the formation of an interface affects the energy. This can be revealed by changing variables to a set that emphasizes the previously-defined $\vec{r_{12}}$. Given the particle separation and the center of mass between the two particles $\vec{r} = \frac{1}{2}(\vec{r_1} + \vec{r_2})$

10

(which assumes equal mass for simplicity), the substitutions follow

$$\vec{r_1} = \vec{r} + \frac{1}{2}\vec{r_{12}} \qquad \vec{r_2} = \vec{r} - \frac{1}{2}\vec{r_{12}} \tag{2.13}$$

This variable change allows us separate terms that depend only on particle separation $\vec{r_{12}}$ by performing Taylor expansions to second order on the two local density terms

$$
\begin{aligned}
\langle U(\vec{r}^N)\rangle =& \frac{1}{2}\int\int u(r_{12})\rho(\vec{r}+\frac{1}{2}\vec{r_{12}})\rho(\vec{r}-\frac{1}{2}\vec{r_{12}})g(r_{12})d\vec{r}dr_{12} \\
=& \frac{1}{2}\int\int \left\{ \left[\rho(\vec{r}) + \frac{1}{2}\vec{r_{12}}\nabla\rho(\vec{r}) + \left(\frac{1}{2}\vec{r_{12}}\right)^2\nabla^2\rho(\vec{r}) + \cancel{O(\partial^3)} \right] \right. \\
& \left. \left[\rho(\vec{r}) - \frac{1}{2}\vec{r_{12}}\nabla\rho(\vec{r}) + \left(-\frac{1}{2}\vec{r_{12}}\right)^2\nabla^2\rho(\vec{r}) + \cancel{O(\partial^3)} \right] \right\} u(\vec{r_{12}})g(\vec{r_{12}})d\vec{r}dr_{12} \\
=& \frac{1}{2}\int\int\left[\rho(\vec{r})\rho(\vec{r}) - \cancel{\frac{1}{2}\vec{r_{12}}\rho(\vec{r})\nabla\rho(\vec{r})} + \frac{1}{8}r_{12}^2\rho(\vec{r})\nabla^2\rho(\vec{r}) \right. \\
& + \cancel{\frac{1}{2}r_{12}^2\rho(\vec{r})\nabla\rho(\vec{r})} - \frac{1}{4}r_{12}^2\nabla\rho(\vec{r})\nabla\rho(\vec{r}) + \cancel{\frac{1}{16}r_{12}^3\nabla\rho(\vec{r})\nabla^2\rho(\vec{r})} \\
& \left. \frac{1}{8}r_{12}^2\rho(\vec{r})\nabla^2\rho(\vec{r}) - \cancel{\frac{1}{16}r_{12}^3\nabla\rho(\vec{r})\nabla^2\rho(\vec{r})} + \cancel{O(\partial^4)} \right] u(\vec{r_{12}})g(\vec{r_{12}})d\vec{r}dr_{12} \\
=& \frac{1}{2}\int\int \left\{ \rho(\vec{r})\rho(\vec{r}) + \frac{1}{4}r_{12}^2\left[\rho(\vec{r})\nabla^2\rho(\vec{r}) - \nabla\rho(\vec{r})\nabla\rho(\vec{r}) \right] \right\} u(\vec{r_{12}})g(\vec{r_{12}})d\vec{r}dr_{12} \\
=& \frac{1}{2}\int \rho(\vec{r})\rho(\vec{r})d\vec{r}\int u(\vec{r_{12}})g(\vec{r_{12}})dr_{12} + \frac{1}{4}\int \rho(\vec{r})\nabla^2\rho(\vec{r})d\vec{r}\int r_{12}^2 u(\vec{r_{12}})g(\vec{r_{12}})dr_{12} \tag{2.14}
\end{aligned}
$$

where for the second-to-last step, we leverage the fact that $\langle U\rangle$ is really a functional of $\rho(\vec{r})$. As such, we are free to partially integrate the term in brackets

$$\int \rho(\vec{r})\nabla^2\rho(\vec{r})d\vec{r} = \cancel{\left.\rho(\vec{r})\nabla\rho(\vec{r})\right|_V}^0 - \int \nabla\rho(\vec{r})\nabla\rho(\vec{r})d\vec{r} \tag{2.15}$$

make a substitution, and combine the two terms into the single term $[2\rho(\vec{r})\nabla^2\rho(\vec{r})]$. Note that the first term in the partial integration vanishes since the density gradients at the limits of our control volume V are assumed to be equal.

The laplacian of the density that has appeared in Eq. (2.14) will account for interfacial effects for phase interfaces within our volume. We can further simplify the differential $\vec{r_{12}}$ in both terms by again leveraging the local isotropy of the fluid to integrate out the directional dependence

11

and transform $d\vec{r}_{12} = 4\pi(r_{12})^2 dr_{12}$, which is the volume of a spherical shell around our reference position $\vec{r}$.

Several options exist to approximate $g(r_{12})$ [37], to include simply setting it equal to 1 for models that account for only long-range interactions. Since the integrals over dr_{12}, which include the distribution function $g(r_{12})$, represent the approximations for inter-particle interactions, we can absorb them into two constants, $-a$ and $-\kappa$. However, since our model is mesoscopic in nature and needs to capture density differences across an interface, we need to keep integrals over $d\vec{r}$. Our final expected value for the internal energy is

$$\langle U(\vec{r}^N) \rangle = \int \rho^2(\vec{r}) d\vec{r} \underbrace{2\pi \int u(r_{12}) g(r_{12})(r_{12})^2 dr_{12}}_{-a} + \int \rho(\vec{r}) \nabla^2 \rho(\vec{r}) d\vec{r} \underbrace{\pi \int u(r_{12}) g(r_{12})(r_{12})^4 dr_{12}}_{-\frac{1}{2}\kappa}$$

(2.16)

With Eq. (2.16), we finally have the full Hamiltonian that is used in evaluating the partition function

$$H(\vec{p}^N, \vec{r}^N) = \sum_{n=1}^{N} \frac{\vec{p}_n^2}{2m_n} + \int \left[-a\rho^2(\vec{r}) - \frac{1}{2}\kappa\rho(\vec{r})\nabla^2\rho(\vec{r}) \right] d\vec{r}$$

(2.17)

We turn our attention back to the full partition function in Eq. (2.20). As usual, the kinetic energy term separates and is easily integrated out, giving

$$\mathcal{Z} = \frac{1}{N!\Lambda^{3N}} \int_{\vec{r}^N} e^{-\beta U(\vec{r}^N)} d\vec{r}^N$$

(2.18)

where $\Lambda = \sqrt{\frac{h^2}{2\pi m k_b T}}$ with m as the mass of a particle, T as the temperature of the fluid, and k_B is Boltzmann's constant. The partition function is now a function of only particle positions. The potential energy term is replaced by our constant mean field approximation $\langle U(\vec{r}^N) \rangle$, and the exponential can thus be removed from the integral, which leaves just the integral over the space of the control volume.

Recall that in principle $u(r_{12})$ can be any number of possible models (e.g. hard sphere, Lennard-Jones, Yukawa, etc.); however, all will specify a region of volume excluded by a repulsive interaction. Figure 2.1 shows a sketch of a Lennard-Jones potential to highlight the physical source of the excluded volume.

12
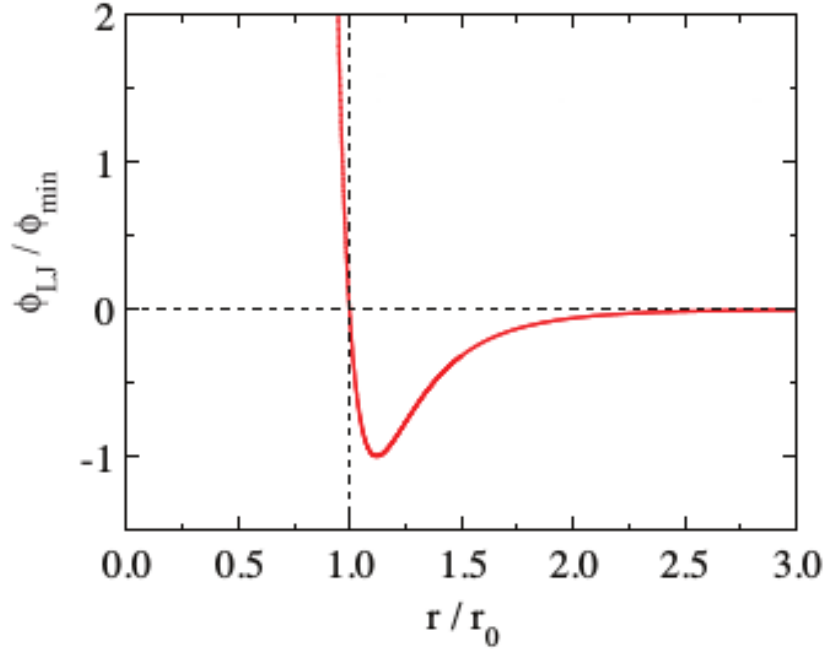
Figure 2.1. This sketch of a Lennard-Jones potential illustrates the physical source of the van der Waals excluded volume. The image is adapted from [1]. We identify $\phi_{LG} \equiv u(r_{12})$, and the intermolecular separation $r/r_0 \equiv r_{12}$. The particle separation that corresponds to the minimum value of the potential, ϕ_{min}, is $r_{12} = \sigma$. The repulsive behavior is the region $r_{12} < \sigma$, which is the left side of the diagram, and is the source of the excluded volume.

The distance between a pair of particles at the minimum of the potential is $r_{12} = \sigma$, and this is the point that separates the attractive behavior from the repulsive behavior. The repulsive side of the potential acts as a "keep out" zone for other particles and thus excludes that part of the overall volume. The volume excluded by a single particle is defined by σ, and it has the mathematical effect of changing the limits of the spatial integrals in Eq. (2.18). This excluded volume will affect the remaining spatial integral, and all N particles will contribute the same to the exclusion. For a control volume with side length R, the lower limit of the spatial integrals changes from zero to σ, giving

$$\int d\vec{r}^N = \int d\vec{r_1} \int d\vec{r_2} ... \int d\vec{r_N} = \left[\int d\vec{r} \right]^N = \left[\int_\sigma^{R_x} \int_\sigma^{R_y} \int_\sigma^{R_z} dx dy dz \right]^N = (V - Nb)^N \quad (2.19)$$

where we identify the volume excluded by a single particle with the van der Waals parameter b. With all approximations applied and integrals computed, we have a partition function $\mathcal{Z}$ that can

be used to determine the thermodynamics of a single-component van der Waals (VDW) fluid

$$\mathcal{Z} \equiv Z_{VDW1} = \frac{(V - Nb)^N}{N!\Lambda^{3N}} e^{-\beta \int \left[-a\rho^2(\vec{r}) - \frac{1}{2}\kappa\rho(\vec{r})\nabla^2\rho(\vec{r}) \right] d\vec{r}} \tag{2.20}$$

The partition function can be immediately evaluated by standard statistical mechanics to determine the the Helmholtz free energy $F(N, V, T)$ of our VDW fluid. Since the density $\rho(\vec{r})$ is allowed to vary macroscopically to form interfaces and is thus a function of position $\vec{r}$, the free energy of the system is in turn a functional of the density $F[\rho(\vec{r})]$. Recalling that $1/\beta = k_B T$, the free energy is

$$F(N, V, T) \equiv F[\rho(\vec{r})] = - k_B T ln Z_{VDW1}$$

$$= - Nk_B T \left\{ ln \left[\frac{(V - Nb)}{N\Lambda^3} \right] + 1 \right\} + \int \left[-a\rho^2(\vec{r}) - \frac{1}{2}\kappa\rho(\vec{r})\nabla^2\rho(\vec{r}) \right] d\vec{r}$$

$$= \int \left[\rho(\vec{r})k_B T \left\{ ln \left[\frac{\rho(\vec{r})}{(1 - b\rho(\vec{r}))} \right] - 1 \right\} - a\rho^2(\vec{r}) - \frac{1}{2}\kappa\rho(\vec{r})\nabla^2\rho(\vec{r}) \right] d\vec{r} \tag{2.21}$$

In the last step, we take $\Lambda = 1$ for simplicity since mass and temperature are both constant in our system. We also include the first term into the overall functional by expressing it in terms of the local density instead of particle number.

Finally, we leverage the partial integration substitution from Eq. (2.15) to write the free energy functional in a more traditional form

$$F[\rho(\vec{r})] = \int \left[\rho(\vec{r})\theta \left\{ ln \left(\frac{\rho(\vec{r})}{(1 - b\rho(\vec{r}))} \right) - 1 \right\} - a\rho^2(\vec{r}) + \frac{1}{2}\kappa\nabla\rho(\vec{r}).\nabla\rho(\vec{r}) \right] d\vec{r} \tag{2.22}$$

2.1.1.1. Free Energy Density

The free energy in Eq. (2.22) is the total free energy of our system, and it represents the free energy over the entire volume V containing our VDW fluid. This volume is allowed to vary in density so that interfaces between coexisting phases may form.

But the term in brackets in Eq. (2.22) - the free energy density - is also of use. The free energy density ψ is

$$\psi = \rho\theta \left\{ ln \left[\frac{\rho}{(1 - b\rho)} \right] - 1 \right\} - a\rho^2 + \frac{1}{2}\kappa(\nabla\rho)^2 \tag{2.23}$$

where we redefine the temperature $\theta = k_B T$. At any given location $\vec{r}$, we assume the VDW fluid is in local equilibrium, so the position dependence of ρ can be dropped in the free energy density. This is equivalent to defining a mesoscopic control volume (i.e. a subvolume of the overall volume V) that is small enough to have a constant density yet large enough when compared to the interaction range between individual particles ($\vec{r_{12}}$) that the mean field approximation is still valid.

From ψ, it is customary to separate the bulk terms ψ_B from the interface terms ψ_I

$$\psi_B = \rho\theta \left\{ ln\left[\frac{\rho}{(1-b\rho)}\right] - 1 \right\} - a\rho^2 \tag{2.24}$$

$$\psi_I = \frac{1}{2}\kappa(\nabla\rho)^2 \tag{2.25}$$

such that when one looks at the full free energy $F[\rho(\vec{r})]$

$$F[\rho(\vec{r})] = \int [\psi_B + \psi_I]d\vec{r} \tag{2.26}$$

it becomes apparent that ψ_I is the energy "cost" that is paid to form an interface.

2.1.1.2. Chemical Potential

A condition for any system to exist in thermodynamic equilibrium is a constant chemical potential across all parts of the system. In our case, we will be modeling a mulitphase system, so this implies the chemical potential in one phase must be equal to the chemical potential in another. We can derive the chemical potential directly from the free energy functional of Eq. (2.22) by computing the functional derivative with respect to $\rho(\vec{r})$

$$\mu(\rho,\theta) = \frac{\delta F[\rho(\vec{r})]}{\delta\rho} = \theta ln\left[\frac{\rho\Lambda^3}{(1-b\rho)}\right] + \frac{b\rho\theta}{1-b\rho} - 2a\rho - \kappa\nabla^2\rho \tag{2.27}$$

Note that the position dependence carried by ρ is implicit from this point forward.

2.1.1.3. Pressure

Unfortunately, evaluating the intensive thermodynamic properties is not quite as easy. Pressure derived from standard statistical mechanics principles assumes a homogenous system in equilibrium. We may use standard means to identify the local equilibrium pressure in our bulk phases

P_B, but density differences across an interface between phases drives a variational approach to determining interface contributions to the pressure P_I [38, 39].

Equivalently, we can leverage the Gibbs-Duhem relation from thermodynamics to derive the correct pressure. For a single-component system, the full Gibbs-Duhem relation is [40]

$$SdT - VdP + Nd\mu = 0 \tag{2.28}$$

Our simulations are for an isothermal system ($dT = 0$), and we take our system volume to be fixed at $V = 1$. Applying these constraints gives

$$\nabla_\beta P_{\alpha\beta} = \rho \nabla_\alpha \mu \tag{2.29}$$

where we have spatially generalized the relation. With our known chemical potentials, we can enforce this relation to ensure the pressure tensor $P_{\alpha\beta}$ is divergence-free in equilibrium.

2.1.1.3.1. Bulk Pressure

To derive the pressure from the partition function in Eq.(2.20), we set $\kappa = 0$. Calculating the appropriate volume derivative gives the well-known VDW equation of state for the bulk pressure P_B

$$\begin{aligned}
P_B(N, V, T) &= k_B T \frac{\partial ln Z_{VDW1}}{\partial V} \\
&= \frac{N k_B T}{(V - Nb)} - \frac{aN^2}{V^2}
\end{aligned} \tag{2.30}$$

$$P_B(\rho, \theta) = \frac{\rho\theta}{(1 - b\rho)} - a\rho^2 \tag{2.31}$$

There is another general and completely equivalent form of the bulk pressure that is common in literature. This form is developed from equilibrium bulk thermodynamics and is very useful for developing the justification for the free energy minimization algorithm in the next section. Note that for this derivation it is implicit that we are working with bulk quantities, so tensor notation is not important.

As noted in the Section 2.1.1.1, the total free energy can be written in terms of a bulk free energy density $\psi_B(\rho)$ that is dependent on particle density ρ. The standard thermodynamic

definition of pressure can then be written as

$$P_B = -\frac{\partial F}{\partial V} = -\frac{\partial}{\partial V}[V\psi_B(\rho)] \tag{2.32}$$

where the total free energy is simply the free energy density times the volume of a container. The volume derivative can be applied via the chain rule to give

$$P_B = -\psi_B(\rho) - V\frac{\partial\psi_B(\rho)}{\partial\rho}\frac{\partial\rho}{\partial V} \tag{2.33}$$

We can recognize that the chemical potential appears by

$$\frac{\partial\psi_B(\rho)}{\partial\rho} = \frac{\partial\psi_B(\rho)}{\partial(N/V)} = \frac{V\partial\psi_B(\rho)}{\partial N} = \frac{\partial F}{\partial N} = \mu_B(\rho) \tag{2.34}$$

and the volume derivative of density gives

$$\frac{\partial\rho}{\partial V} = \frac{\partial(N/V)}{\partial V} = N\frac{\partial(V^{-1})}{\partial V} = -\frac{\rho}{V} \tag{2.35}$$

Substituting these into Eq. (2.33) and simplifying gives the general bulk pressure

$$P_B = -\psi_B(\rho) - \cancel{V}\mu_B(\rho)\left(-\frac{\rho}{\cancel{V}}\right)$$
$$P_B = \rho\mu_B(\rho) - \psi_B(\rho) \tag{2.36}$$

2.1.1.3.2. Interface Pressure

The free energy is written to include gradient terms at the interfaces between components ($\psi_I = \kappa\nabla\rho\nabla\rho$). As a result, a gradient terms also appears in the chemical potential ($\mu_I = -\kappa\nabla^2\rho$). By demanding the Gibbs-Duhem relation is satisfied ($\nabla_\beta P_{\alpha\beta} \overset{!}{=} \rho\nabla_\alpha\mu$), we can use this gradient term to construct the gradient terms that comprise the rest of the pressure tensor while demanding that Gibbs-Duhem holds. Given μ_I, the right-hand side of the Gibbs-Duhem relation is

$$\rho\nabla_\alpha\mu_I = -\kappa\rho\nabla_\alpha\nabla^2\rho \tag{2.37}$$

17

If we can construct pressure interface terms P_I that yield this result when we apply the gradient operation to them, Gibbs-Duhem will be satisfied.

The P_I terms can be constructed iteratively by guessing an initial form for P_I, applying the gradient operation to it, identifying extraneous terms that do not satisfy Gibbs-Duhem, and modifying the P_I guess by inspection of extraneous terms. Using the right-hand side μ_I result directly as a first guess

$$P_{\alpha\beta} \equiv P_I \overset{?}{=} -\kappa\rho\nabla^2\rho\delta_{\alpha\beta} \tag{2.38}$$

Applying the Gibbs-Duhem gradient operation to this term reveals an extraneous term to be cancelled

$$\nabla_\beta P_I = -\nabla_\beta\kappa\rho\nabla^2\rho\delta_{\alpha\beta} \tag{2.39}$$

$$= -\kappa\nabla_\alpha\rho\nabla^2\rho - \underbrace{\kappa\rho\nabla_\alpha\nabla^2\rho}_{\text{extra term}} \tag{2.40}$$

To produce a term that will cancel the first above but keep the second (which is the chemical potential portion of the Gibbs-Duhem relation we need to preserve), we modify the pressure tensor gradient terms to

$$P_{\alpha\beta} \equiv P_I \overset{?}{=} -\kappa\delta_{\alpha\beta}\rho\nabla^2\rho + \kappa\nabla_\alpha\rho\nabla_\beta\rho \tag{2.41}$$

The derivative of this new term modifies the pressure tensor gradient by

$$\nabla_\beta P_I = \nabla_\beta\left(-\kappa\delta_{\alpha\beta}\rho\nabla^2\rho + \kappa\nabla_\alpha\rho\nabla_\beta\rho\right) \tag{2.42}$$

$$= -\cancel{\kappa\nabla_\alpha\rho\nabla^2\rho} - \kappa\rho\nabla_\alpha\nabla^2\rho + \kappa\nabla_\alpha\nabla_\beta\rho\nabla_\beta\rho + \cancel{\kappa\nabla_\alpha\rho\nabla_\beta\nabla_\beta\rho} \tag{2.43}$$

$$= -\kappa\rho\nabla_\alpha\nabla^2\rho + \underbrace{\kappa\nabla_\alpha\nabla_\beta\rho\nabla_\beta\rho}_{\text{extra term}} \tag{2.44}$$

The previous extraneous term has been eliminated (since $\nabla^2 \equiv \nabla_\beta\nabla_\beta$), but a new one remains. Another modification to the guess for the interfacial pressure and application of the

18

gradient operation yields

$$P_{\alpha\beta} \equiv P_I \overset{?}{=} -\kappa\delta_{\alpha\beta}\rho\nabla^2\rho + \kappa\nabla_\alpha\rho\nabla_\beta\rho - \frac{1}{2}\kappa\nabla_\gamma\rho\nabla_\gamma\rho\delta_{\alpha\beta} \tag{2.45}$$

$$\nabla_\beta P_I = \nabla_\beta\left(-\kappa\delta_{\alpha\beta}\rho\nabla^2\rho + \kappa\nabla_\alpha\rho\nabla_\beta\rho - \frac{1}{2}\kappa\nabla_\gamma\rho\nabla_\gamma\rho\delta_{\alpha\beta}\right) \tag{2.46}$$

$$= \cancel{-\kappa\nabla_\alpha\rho\nabla^2\rho} - \kappa\rho\nabla_\alpha\nabla^2\rho + \kappa\nabla_\alpha\nabla_\beta\rho\nabla_\beta\rho \tag{2.47}$$

$$+ \cancel{\kappa\nabla_\alpha\rho\nabla_\beta\nabla_\beta\rho} - \frac{1}{2}\kappa\left(\nabla_\alpha\nabla_\gamma\rho\nabla_\gamma\rho + \nabla_\gamma\rho\nabla_\alpha\nabla_\gamma\rho\right) \tag{2.48}$$

$$= -\kappa\rho\nabla_\alpha\nabla^2\rho + \cancel{\kappa\nabla_\alpha\nabla_\beta\rho\nabla_\beta\rho} - \frac{1}{2}\cancel{2\kappa\nabla_\alpha\nabla_\beta\rho\nabla_\beta\rho} \qquad \text{(relabel } \gamma \equiv \beta) \tag{2.49}$$

$$= -\kappa\rho\nabla_\alpha\nabla^2\rho \tag{2.50}$$

No extra terms exist, so these gradient terms will satisfy the Gibbs-Duhem relation. Simplifying a bit, we have for the interfacial pressure contributions

$$P_I = -\kappa\left[\left(\rho\nabla^2\rho + \frac{1}{2}\nabla_\gamma\rho\nabla_\gamma\rho\right)\delta_{\alpha\beta} - \nabla_\alpha\rho\nabla_\beta\rho\right] \tag{2.51}$$

Combining the bulk pressure P_B from Eq. (2.36) - which appears only on the diagonal of the resulting pressure tensor - and the interface pressures P_I from Eq. (2.51) and simplifying a bit, we have constructed the final single-component pressure tensor ($P_{\alpha\beta} = P_B\delta_{\alpha\beta} + P_I$)

$$P_{\alpha\beta} = \left[\rho\mu_B(\rho) - \psi_B(\rho) - \kappa\left(\rho\nabla^2\rho + \frac{1}{2}\nabla_\gamma\rho\nabla_\gamma\rho\right)\right]\delta_{\alpha\beta} - \kappa\nabla_\alpha\rho\nabla_\beta\rho \tag{2.52}$$

2.1.1.4. van der Waals Constants

The critical properties of a fluid - temperature θ_c, pressure p_c, and density ρ_c - are related to the constants a and b in the VDW equation of state (EOS) of Eq. (2.31) [1]. As a fluid transitions through a range of temperatures, an isotherm in the pressure-density (volume) plane develops an inflection at the point where a phase transition begins, the critical point. This transition is shown below in Figure 2.2
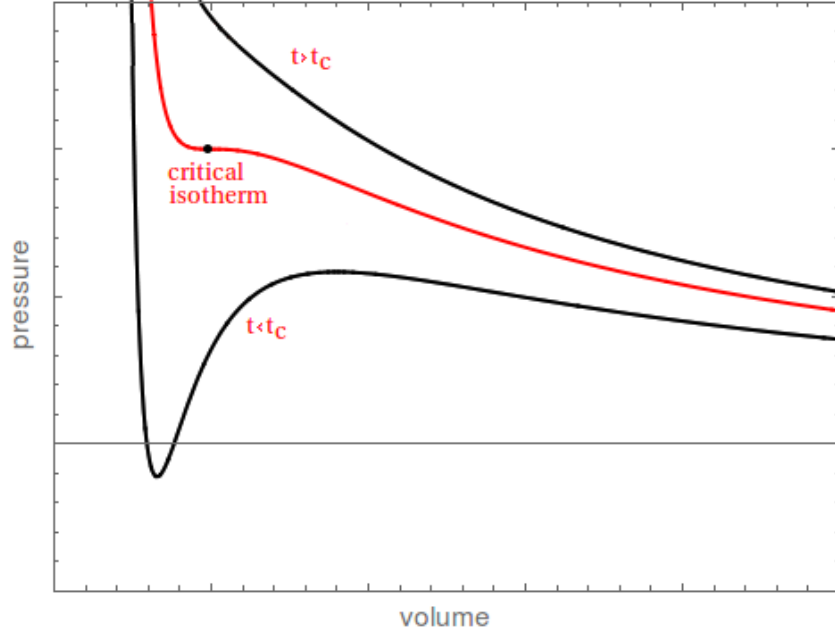
Figure 2.2. Isotherms of the VDW EOS are shown above, at, and below the critical temperature $(t_c \equiv \theta_c)$. The red isotherm is the critical isotherm where the fluid temperature is equal to its critical temperature. The point on the critical isotherm is the inflection point which identifies the critical pressure and density. The image is adapted from [2].

The inflection point is defined by the facts

$$\frac{\partial P}{\partial V} = 0 \qquad \frac{\partial^2 P}{\partial V^2} = 0 \tag{2.53}$$

Computing these derivatives and solving the system of equations for the critical properties in terms of the constants a and b gives

$$\theta_c = \frac{8a}{27b} \qquad p_c = \frac{a}{27b^2} \qquad V_c = 3Nb \tag{2.54}$$

Although these relations would be sufficient to specify the properties of a fluid we wish to simulate, we can invert these relations to specify the constants a and b in terms of the critical properties. The reason we do this is because pressure, temperature, and volume have a concrete,

20

intuitive meaning that can be measured directly. If we divide θ_c by p_c and simplify, we find

$$b = \frac{\theta_c}{8p_c} \tag{2.55}$$

Proceeding to a, squaring θ_c before dividing by p_c gives

$$a = \frac{27\theta_c^2}{64p_c} \tag{2.56}$$

Note that specifying b in terms of the critical temperature and pressure sets the value of the critical density. In reality, we could specify any two of the critical traits and derive the third by constructing

$$Z_c = \frac{p_c}{\rho_c\theta_c} = \frac{3}{8} \tag{2.57}$$

which is known as the universal compressibility ratio. This is a consequence of van der Waals' law of corresponding states.

2.1.2. Multiple Components

The extension of the single component theory just outlined to multiple components is straightforward. For a mixture composed of N_C components, we extend the double summation over all particle pairs in Eq. (2.2) to also sum over all pairs of components

$$U(\vec{r}^N) = \sum_c^{N_C} \sum_{c'}^{N_C} \sum_{i=1}^{n^c} \sum_{j=i+1}^{n^{c'}} u^{cc'}(\vec{r_{ij}}) \tag{2.58}$$

where c, c' are general components in the mixture and $n^c, n^{c'}$ are the numbers of particles of those components, respectively. The total number of particles in the mixture is now given by $\sum_c^{N_C} n^c = N$. We clarify that lower-case c used as a subscript as in the previous section denotes a critical trait and c used as a superscript here is a general component identifier.

Specifying the particle pair interactions in this manner will allow us to separate the cross-component interactions ($u^{cc'}$ for $c \neq c'$) from the self-interactions (u^{cc}). This manifests explicitly

21

when the extension of Eq. (2.16) gives

$$\langle U(\vec{r}^N)\rangle = \sum_c \sum_{c'} (-a^{cc'} \int \rho^c \rho^{c'} d\vec{r} - \kappa^{cc'} \int \rho^c \nabla^2 \rho^{c'} d\vec{r}) \quad \text{for } c \neq c' \tag{2.59}$$

where each cross-component $(a^{cc'}, \kappa^{cc'})$ and self-interaction (a^{cc}, κ^{cc}) picks up its own pair of VDW and interfacial energy constants. The rules by which mixing unlike components c and c' result in the cross-component interaction constants vary. The choice of mixing rules is usually by an arbitrary balance among the need for precision, generality, computational simplicity, and other concerns [3].

In principle, each component can also have it's own molecular size, and the combinations of different components would exclude varying volumina. Generally, this would be denoted $b^{cc'}$, which flows into the excluded volume expression in Eq. (2.19). This modifies the excluded volume to

$$\int d\vec{r}^N = (V - \frac{1}{2} \sum_c \sum_{c'} n^c b^{cc'})^N \tag{2.60}$$

The volume excluded by a given pair $b^{cc'}$ must be prescribed much like for $a^{cc'}$ and $\kappa^{cc'}$. For the remainder of this thesis, we make the simplest assumption that cross-component excluded volumina are adequately accounted for by the individual components (i.e. $b^{cc'}$ when $c \neq c'$ is captured by $b^{cc} \equiv b^c$) and we only need to linearly combine each component [3, 26]. We modify our excluded volume to the simple-to-implement

$$\int d\vec{r}^N = (V - \sum_c n^c b^c)^N \tag{2.61}$$

These corrections flow seamlessly into the partition function for a single component. Since the mean field approximations now contain the effects of all components, we are free to treat each component independently to construct the partition function for a mixture of VDW fluids

$$Z_{VDW} = \prod_c^{N_C} \left[\frac{(V - \sum_{c'} n^{c'} b^{c'})^{n^c}}{(\Lambda^c)^{3n^c} n^c!} e^{-\beta \int \rho^c \sum_{c'} (-a^{cc'} \rho^{c'} - \kappa^{cc'} \nabla^2 \rho^{c'}) d\vec{r}} \right] \tag{2.62}$$

Eq. (2.62) can be a little difficult to pick apart. Since the vast majority of this thesis deals specifically with a binary mixture of VDW fluids, Appendix A explicitly shows the partition function expansion of the two-component case and the derivation of two-component thermodynamics. We

also include the construction of the multicomponent pressure tensor in Appendix B. The examples in the appendices can be easily generalized as follows for N-component thermodynamics

$$F = \int \sum_{c}^{N_C} \left[\rho^c \theta ln \left(\frac{\rho^c (\Lambda^c)^3}{1 - \sum_{c'} b^{c'} \rho^{c'}} \right) - \theta \sum_{c'} \rho^{c'} - \sum_{c'} a^{cc'} \rho^c \rho^{c'} + \sum_{c'} \kappa^{cc'} \nabla \rho^c . \nabla \rho^{c'} \right] d\vec{r} \quad (2.63)$$

$$\mu^c = \theta ln \left(\frac{\rho^c (\Lambda^c)^3}{1 - \sum_{c'} b^{c'} \rho^{c'}} \right) + \frac{b^c \rho^c \theta}{1 - \sum_{c'} b^{c'} \rho^{c'}} - 2 \sum_{c'} a^{cc'} \rho^{c'} - \sum_{c'} \kappa^{cc'} \nabla^2 \rho^{c'} \quad (2.64)$$

$$P_{\alpha\beta} = \sum_{c} \left[\rho^c \theta + \frac{b^c (\rho^c)^2 \theta}{1 - \sum_{c'} b^{c'} \rho^{c'}} - \sum_{c'} a^{cc'} \rho^c \rho^{c'} \right.$$
$$\left. - \sum_{c'} \kappa^{cc'} (\nabla_\gamma \rho^c \nabla_\gamma \rho^{c'} + \rho^c \nabla^2 \rho^{c'}) \right] \delta_{\alpha\beta} + \sum_{cc'} \kappa^{cc'} \nabla_\alpha \rho^c \nabla_\beta \rho^{c'} \quad (2.65)$$

2.1.2.1. Two-Component Mixture VDW Constants

When mixing two or more fluids together, each component is defined by its own critical properties. Extending the definitions of the VDW constants from Section 2.1.1.4 to their usage in the general thermodynamic equations given above in Eqs. (2.63), (2.64), and (2.65), we can specify the terms for the two-component free energy we seek to minimize.

Components A and B are defined by the critical traits $(\theta_c^A, p_c^A, \rho_c^A)$ and $(\theta_c^B, p_c^B, \rho_c^B)$ respectively. The VDW constants for each individual component are

$$a^A = \frac{27(\theta_c^A)^2}{64 p_c^A} \qquad b^A = \frac{\theta_c^A}{8 p_c^A} \qquad (2.66)$$

$$a^B = \frac{27(\theta_c^B)^2}{64 p_c^B} \qquad b^B = \frac{\theta_c^B}{8 p_c^B} \qquad (2.67)$$

where $a^{cc} \equiv a^A, a^B$ and $b^c \equiv b^A, b^B$. Fully specifying the components of our mixtures requires us to choose 4 of the 6 critical traits, 2 for each component. We can then use the universal compressibility ratio from Eq. (2.57) to fix the fifth and sixth traits. In practice, we will always choose the critical density of component A to equal 1 ($\rho_c^A = 1$) as a further simplification.

A new trait must be introduced to characterize the interaction between components A and B. Given the VDW constants a^A and a^B, which capture the energy of self-interactions for components A and B respectively, we define

$$a^{AB} = \nu \sqrt{a^A a^B} \qquad (2.68)$$

23

to capture the energy of interaction between components. This is an application of the geometric mixing rule used by the physical chemist van Laar, who was a contemporary of van der Waals [41]. We include the parameter ν to allowing for deviations from the neutral mixing rule [28, 42]. With this rule in place, a neutral interaction corresponds to $\nu = 1$, which is also exactly what van Laar used. A repulsive interaction corresponds to $\nu < 1$, and an attractive interaction corresponds to $\nu > 1$.

2.2. Discrete Theory

Having fully defined the statistical mechanical and thermodynamic continuum theory for a multicomponent, multiphase mixture, we now turn to the discrete case. Discretizing our thermodynamic properties properly is a key piece to implementing conservative forcing in a mixture and to ensuring the simulations are thermodynamically consistent. Although the notation can get somewhat cumbersome, the actual discretization is really straightforward when read in the context of the continuous theory.

At a high level, all that really changes is that the densities pick up a position dependence $\rho(x)$, where x designates a lattice site which is a subvolume of our overall control volume V. We note that although we use the notation x to denote a specific lattice position, it should be understood that the lattice is in principle multidimensional. As a result, all of the thermodynamic quantities we are interested in implicitly depend on lattice site x as well through $\rho(x)$.

To complete the discretization of our free energy, we first convert the integral over V for the free energy functional into a sum over x. We also rewrite the $a^{cc'}$ and $\kappa^{cc'}$ terms from Eq. (2.63) as a single term in $\phi^{cc'}(\Delta x)$, which serves as a general lattice interaction parameter that is a function of the distance to lattice neighbors. We assume here that the interaction parameter is spatially symmetric $\phi^{cc'}(-\Delta x) = \phi^{cc'}(\Delta x)$ and symmetric between a pair of given components $\phi^{cc'}(\Delta x) = \phi^{c'c}(\Delta x)$. This interaction is applied by summing across an arbitrary number of neighbor lattice sites Δx

$$F = \sum_c \sum_x \left[\rho^c(x)\theta ln\left(\frac{\rho^c(x)}{1 - \sum_{c'} b^{c'}\rho^{c'}(x)}\right) - \rho^c(x)\theta + \sum_{c'}\sum_{\Delta x} \phi^{cc'}(\Delta x)\rho^c(x)\rho^{c'}(x + \Delta x) \right] \quad (2.69)$$

where we take $\Lambda = 1$. By applying the same approach used to show how $u(r_{12})$ and $g(r_{12})$ both relate to a and κ in the derivation of Eq. (2.16), the relationship between $\phi^{cc'}$ and $a^{cc'}, \kappa^{cc'}$ becomes

clear after Taylor expanding the term $\rho^{c'}(x + \Delta x)$. Showing only the interaction terms with the lattice neighbor dependence of $\phi^{cc'}$ implied, we have

$$\sum_{c'}\sum_{\Delta x}\phi^{cc'}\rho^c(x)\left(\rho^{c'}(x) + \Delta x \overset{\text{0 by isotropy}}{\cancel{\nabla \rho^{c'}(x)}} + \frac{1}{2}(\Delta x)^2\nabla^2\rho^{c'}(x) + \cancel{O(\partial^3)}\right)^{\cancel{0}} \tag{2.70}$$

$$= \sum_{c'}\sum_{\Delta x}\phi^{cc'}\rho^c(x)\rho^{c'}(x) + \frac{1}{2}\sum_{c'}\sum_{\Delta x}\phi(\Delta x)^2\rho^c(x)\nabla^2\rho^{c'}(x) \tag{2.71}$$

$$= \sum_{c'}\underbrace{\sum_{\Delta x}\phi^{cc'}}_{-a}\rho^c(x)\rho^{c'}(x) + \sum_{c'}\frac{1}{2}\underbrace{\sum_{\Delta x}\phi^{cc'}(\Delta x)^2}_{-\kappa}\rho^c(x)\nabla^2\rho^{c'}(x) \tag{2.72}$$

which shows the interaction parameters $a^{cc'}, \kappa^{cc'}$ as "moments" of the lattice interaction parameter $\phi^{cc'}$

$$-a^{cc'} = \sum_{\Delta x}\phi^{cc'} \tag{2.73}$$

$$-\kappa^{cc'} = \sum_{\Delta x}\phi^{cc'}(\Delta x)^2 \tag{2.74}$$

As will be seen in Section 5.4, these "moments" can be exploited to derive an appropriate gradient stencil for a specific LB implementation.

The discrete chemical potentials and pressure also pick up the same dependence on lattice position as the free energy. Moreover, the lattice interaction parameter $\phi^{cc'}$ carries through to the chemical potentials, driving the same definitions of $a^{cc'}, \kappa^{cc'}$, and a gradient stencil. This results in the same forms for the chemical potentials as Eq. (2.64) and pressure as Eq. (2.65).

3. FREE ENERGY MINIMIZATION AND MULTICOMPONENT PHASE DIAGRAMS

Our forthcoming LB simulations exist in a mechanically closed, isothermal system, the dynamics of which are governed by the minimum energy principle. Part and parcel to developing the LB simulations is having a method by which we can judge the accuracy of the results. Minimizing a Helmholtz free energy will allow us to generate predictions for the behavior of a given system, and we can use these predictions to characterize the performance of our simulations.

The theoretical phase diagrams by which we judged the performance of the LB method were created by numerically minimizing the underlying free energy of a multicomponent mixture of van der Waals fluids, given by Eq. (2.63). This section outlines the development of the free energy minimization, beginning with single-component concepts and extending them to the multi-component case. These concepts are used to help develop the intuition of the minimization process. This section concludes with a description of the quasi-brute force minimization algorithm used is presented to accentuate the underlying physics of the mixture.

3.1. Gibbs Phase Rule

In order to architect an adequate free energy minimization algorithm, one must have an idea of how many phases a given mixture might exhibit in equilibrium. We can apply the Gibbs phase rule to set an upper limit on how many phases can be allowed [40]

$$f = N_C - M + 2 \tag{3.1}$$

where N_C is the number of components in a mixture, M is the number of possible phases, and f is the number of thermodynamic degrees of freedom. The maximum number of phases M possible is when $f = 0$.

Specific to the binary mixture ($N_C = 2$) that is the main focus of this thesis, we find that the two components may exist in at most four phases. With no remaining thermodynamic degrees of freedom, the can occur only at a single temperature, pressure, and set of densities for each component. But this does not preclude the possibility of accessing a 1-, 2-, or 3-phase region, each

of which have degrees of freedom available to generate phase diagrams. With this in mind, we proceed to build the physical intuition of an algorithm that minimizes the free energy of a binary mixture while allowing for three coexisting phases.

3.2. Common Tangent Construction

Under appropriate conditions, a homogeneous fluid will self-organize into distinct phases as a way to lower the free energy of the system. The free energy can be modelled by a linear combination of the resulting phases. For the standard example of a single component separating into two coexisting phases, the free energy is [43]

$$F = V_1 \psi(\rho_1) + V_2 \psi(\rho_2) \tag{3.2}$$

where the subscripts $1, 2$ for the volume V, and density ρ denote the two phases. The densities are with regards to the number of particles and the volume of each respective phase ($\rho_1 = N_1/V_1, \rho_2 = N_2/V_2$). Rewriting the total free energy F as a product of the average free energy density and total volume (both unsubscripted), we find that each phase contributes to the free energy in a manner that is weighted by relative volumina

$$\psi = \frac{V_1}{V}\psi(\rho_1) + \frac{V_2}{V}\psi(\rho_2) \tag{3.3}$$

The constraint that the relative volumina of each phase must conserve the total volume of the system ($V_1 + V_2 = V$) means we can parameterize the free energy as a line.

$$\psi = (1 - s)\psi_1 + s\psi_2 \tag{3.4}$$

where we simplify the notation by $\psi_1 \equiv \psi(\rho_1)$ and $\psi_2 \equiv \psi(\rho_2)$. The bulk free energy density of each phase is given by the bulk pressure expression of Eq. (2.36)

$$\psi_1 = \mu_1 \rho_1 - P_1 \tag{3.5}$$

$$\psi_2 = \mu_2 \rho_2 - P_2 \tag{3.6}$$

Substituting into Eq. (3.4) gives

$$\psi = (1 - s)(\mu_1 \rho_1 - P_1) + s(\mu_2 \rho_2 - P_2) \tag{3.7}$$

In thermodynamic equilibrium, the chemical potentials and pressures in each phase must be equal ($\mu_1 = \mu_2 = \mu, P_1 = P_2 = P$). This allows us to simplify

$$\begin{aligned}
\psi =& (1 - s)(\mu \rho_1 - P) + s(\mu \rho_2 - P) \\
=& \mu \rho_1 - P - s\mu \rho_1 + \cancel{sP} + s\mu \rho_2 - \cancel{sP} \\
=& \mu \underbrace{[(1 - s)\rho_1 + s\rho_2]}_{\rho} - P \tag{3.8}
\end{aligned}$$

Because the total particle number/mass is conserved ($N_1 + N_2 = N$), this equation shows a single parameterized line at average density ρ with a slope of μ and a y-axis intercept of P. This is the common tangent construction, illustrated in Figure 3.1.
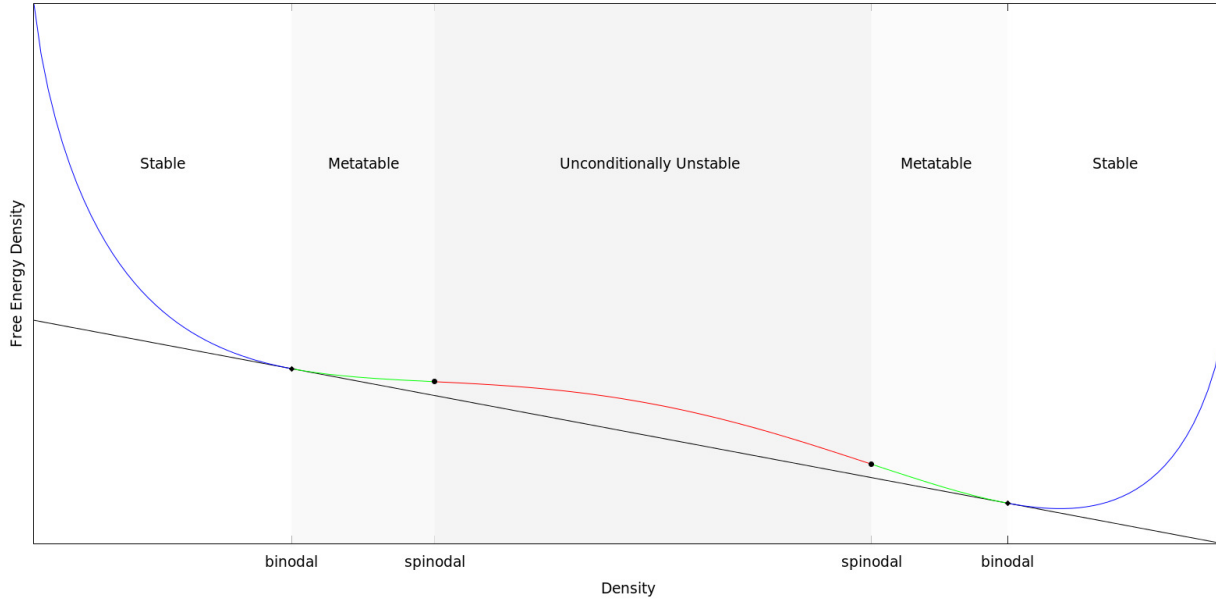
Figure 3.1. Curve depicting a notional isothermal free energy at a temperature below the critical temperature of a fluid. Binodal points are defined by the two points at which the line $(\mu\rho - P)$ beneath the curve is tangent to the curve ψ (i.e. $(1-s)\rho_1$ and $s\rho_2$ in Eq. 3.8). Spinodal points are defined by changes of curvature of the free energy curve. Metastability exists between binodal and spinodal points. Fluids at any density in the unconditionally unstable (red) region of the graph will separate into two phases with densities defined by the binodal points. Equilibrium chemical potential is the slope of the tangent line, and the equilibrium pressure is the y-axis intercept of the tangent line.

The curve in Figure 3.1 is isothermal. Generating a series of these curves for several temperatures and performing a common tangent construction for each allows us to plot the locus of binodal points that result. This results in the well-known density-vs-temperature phase diagram for a single van der Waals fluid, which is shown below in Figure 3.2.

29
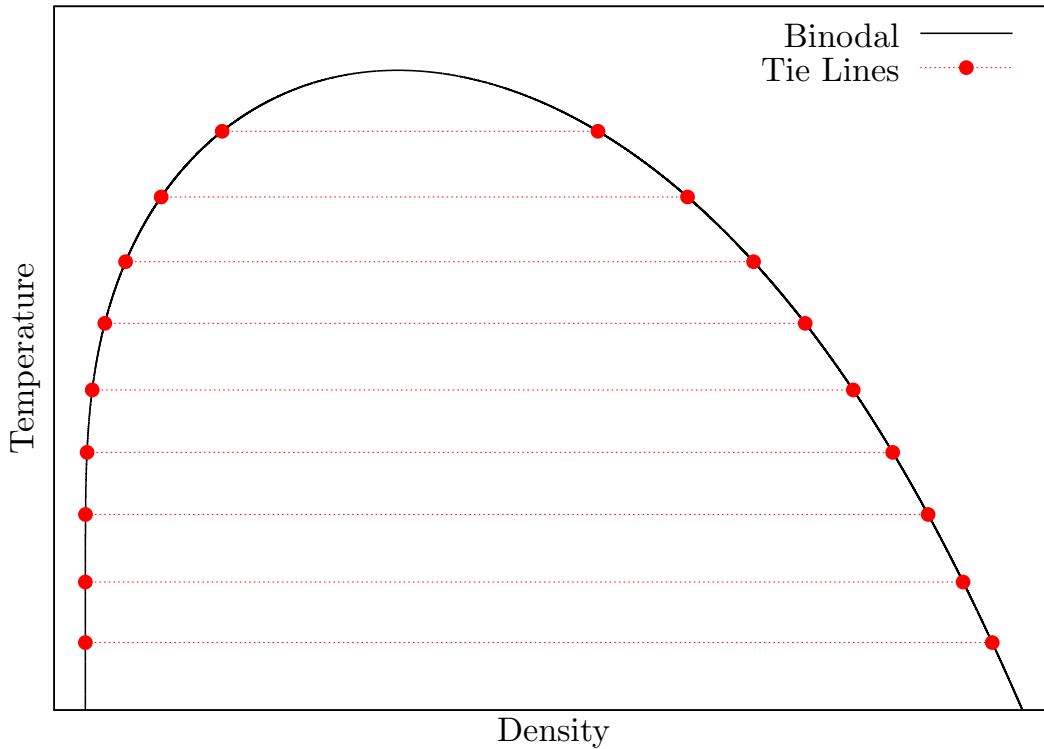
Figure 3.2. A free energy surface for a single VDW fluid would project this phase diagram onto the density-temperature plane. The binodal is the locus of points where a tangent plane that touches the surface is rolled across the fold in the surface.

The apex of the curve is the critical point, above which a fluid will not separate into multiple phases. The thermodynamic characteristics at this point (temperature, density, and pressure) were noted earlier in Sections 2.1.1.4 and 2.1.2.1, and we use them to specify the components of a mixture in our simulations in Chapter 6.

3.3. Multicomponent Free Energy Surface

The original research of van der Waals was extended from the free energy curve used to model a single component to a free energy surface for modelling situations with more than one component. van der Waals and his contemporary, Korteweg, performed a large part of their research by considering the Helmholtz free energy of a binary mixture as such a surface [3, 27]. A photo of an actual wooden carving used by van der Waals to show the topography of such a surface and an accompanying figure from a Korteweg analysis are shown in Figure 3.3.
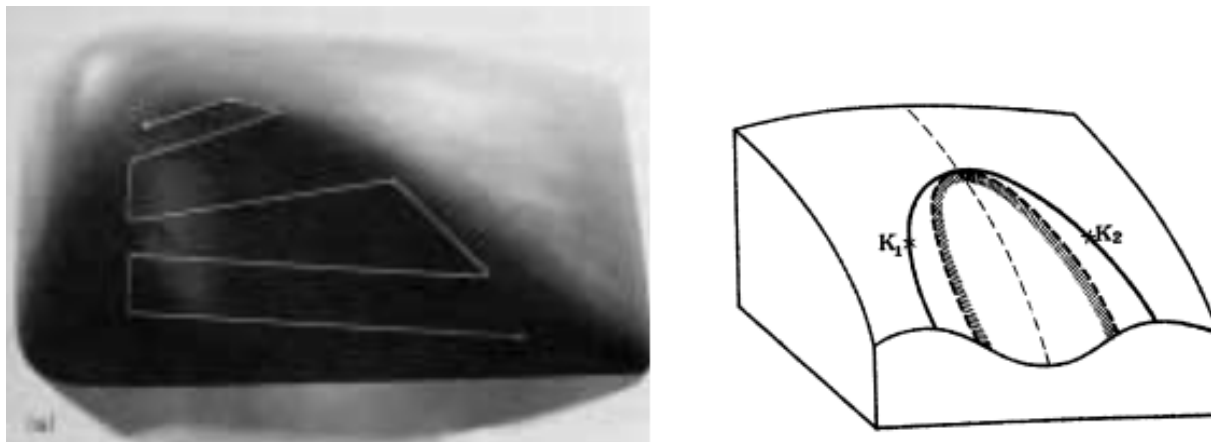
Figure 3.3. A wooden carving used by van der Waals to illustrate the concept of a free energy surface [3]. To the right is a sketch used by Korteweg in the analysis of an analogous surface. The surface has a fold in it which corresponds to the unstable region of the free energy. One can imagine laying a plane on the surface such that it is tangent to the surface at two points, which correspond to the coexisting densities at a given temperature. Rolling the plane along the surface to trace out a locus of tangent points would produce a binodal similar to the common density-vs-temperature phase diagram for a single component shown in Figure 3.2.

The unstable region of the surface forms a fold, or "plait," in the surface. If one were to place a tangent plane on top of this surface across the fold, the plane would contact the surface at two points. Figure 3.3 also illustrates how pairs of these points form tie lines that span the plait to define phase coexistence. Rolling the tangent plane over the surface traces the ends of the set of tie lines (i.e. coexisting densities) that span the plait. The plait terminates at a plait point, which corresponds to what is now called a critical point, where the plane is tangent to the free energy surface at a single point.

The concept for a binary fluid mixture was even shown with 3-phase coexistence. A photograph of van der Waals' original wooden carving showing 2-component, 3-phase behavior is shown in Figure 3.4. The surface in this case contains multiple plaits which merge with each other. The tangent plane begins by contacting the surface at only two points, as usual. However, a region is encountered where due to the intersecting plaits, a third point of contact is discovered. This defines the three densities that coexist.

Figure 3.4. This wood carving used by van der Waals as a teaching aid to depict the topography of a free energy surface corresponding to a hypothetical binary mixture. A plane rolled along the surface would transition from two points of contact (2-phase behavior) to three points of contact (3-phase behavior). [3]

Since a tie line across a three-dimensional free energy surface defines phase coexistence, it is by definition an isothermal slice of the surface. Considering just that slice of the surface allows a projection down to a two-dimensional free energy curve. This gives us an intuitive basis to extend the development of the common tangent construction from Section 3.2 to account for the addition of a second component. The bulk free energy density from the single-component, 2-phase case simply adds the third phase into the mix when a second component is added

$$\psi = \frac{V_1}{V}\psi_1 + \frac{V_2}{V}\psi_2 + \frac{V_3}{V}\psi_3 \tag{3.9}$$

$$\psi = (1 - s - t)\psi_1 + s\psi_2 + t\psi_3 \tag{3.10}$$

The multicomponent free energy in Eq. (2.63) is the basis for the free energy densities ψ_1, ψ_2, and ψ_3. In principle, the pressure term of the free energy density will always be the same in each phase, but each component of a mixture will contribute its own chemical potential term to each phase. We illustrate the two component free energy densities here since the bulk of this thesis

32

involves two components with three phases allowed

$$\psi_1 = \mu_1^A \rho_1^A + \mu_1^B \rho_1^B - P_1 \tag{3.11}$$

$$\psi_2 = \mu_2^A \rho_2^A + \mu_2^B \rho_2^B - P_2 \tag{3.12}$$

$$\psi_3 = \mu_3^A \rho_3^A + \mu_3^B \rho_3^B - P_3 \tag{3.13}$$

where the letter parts of the subscripts denote the component and the numeric parts of the scripts denote the phase. Substituting these free energy density expressions for each phase into the parameterized average free energy density and simplifying under conditions of equilibrium (i.e. equal pressures and chemical potentials for each component), we have

$$
\begin{aligned}
\psi =& (1 - s - t)(\mu^A \rho_1^A + \mu^B \rho_1^B - P) + s(\mu^A \rho_2^A + \mu^B \rho_2^B - P) + t(\mu^A \rho_3^A + \mu^B \rho_3^B - P) \\
=& \mu^A \rho_1^A + \mu^B \rho_1^B - P - s\mu^A \rho_1^A - s\mu^B \rho_1^B + \cancel{sP} + s\mu^A \rho_2^A + s\mu^B \rho_2^B - \cancel{sP} \\
& - t\mu^A \rho_1^A - t\mu^B \rho_1^B + \cancel{tP} + t\mu^A \rho_3^A + t\mu^B \rho_3^B - \cancel{tP} \\
=& \mu^A \underbrace{[(1 - s - t)\rho_1^A + s\rho_2^A + t\rho_3^A]}_{\rho^A} + \mu^B \underbrace{[(1 - s - t)\rho_1^B + s\rho_2^B + t\rho_3^B]}_{\rho^B} - P \tag{3.14}
\end{aligned}
$$

Geometrically, our common tangent line has just become a common tangent plane in three-dimensional space. Coordinates in this space are given in density-density-energy triples (ρ^A, ρ^B, ψ). The parameterized equation for each component density indicates that the plane can touch the free energy surface at one, two, or three locations, depending on the values of each parameter. The slopes of each side of the plane are defined by the chemical potentials of each component, and the intercept of the plane on the free energy density axis is defined by the equilibrium pressure of the system.

Generally speaking, this method is very easily extensible, and the description is intuitively simple. For each additional component added to the mixture, add another term to the free energy density for each allowed phase with the maximum possible phases set by Gibbs' phase rule. For each additional phase, add another free energy density weighted by the relative volume of that phase. We preserved this simplicity in the algorithm we used to minimize the free energy of a two-component system while allowing for three coexisting phases.

33

3.4. Stability Analysis

Key to the free energy minimization of a given mixture is how stable or unstable the mixture is [36, 44]. The stability of a mixture is determined by the local curvature of the free energy surface. Analysis of the surface's curvature at the location of a mixture of interest allows us to predict if the mixture is prone to phase separation. Additionally, if it turns out the mixture is unstable, the stability analysis also gives us a direction in which the phase separation will proceed.

Were our fluid made of a single component, the sign of the second free energy density derivative with respect to the component density is all we would need to determine stability - a positive second derivative indicates a metastable (or stable) fluid and a negative second derivative indicates the fluid is unstable and will exhibit phase separation. Referencing Figure 3.1 in the single-component case, the concave (red) portion of the curve is where the second derivative is negative, which corresponds to unconditional instability of a fluid. Since our mixture is specifically two components (ρ^A, ρ^B), our stability analysis is a bit more complicated (see Figure 3.5).
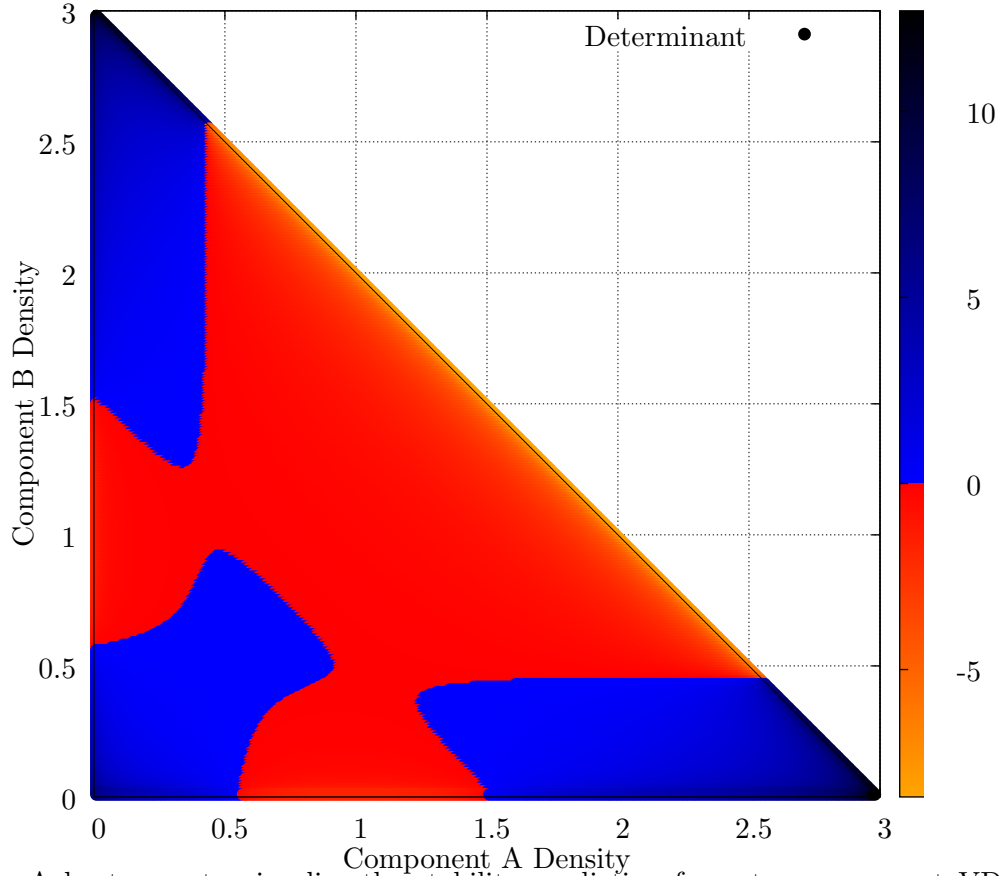
Figure 3.5. A heat map to visualize the stability prediction for a two-component VDW fluid. Each point is a (ρ^A, ρ^B) density pair representing a homogeneous mixture. The color of the point shows the value of the determinant of the Hessian matrix at that point, which is the product of the two eigenvalues of the Hessian. Negative determinants have a single negative eigenvalue and predict phase separation for the mixture at the given point. Positive determinants indicate both eigenvalues are positive and the mixture is located on a stable (or metastable) point on the free energy surface. There are no points with two negative eigenvalues. The diagonal line is the van der Waals singularity where $1 = \rho^A b^A + \rho^B b^B$.

We must use a *matrix* of second derivatives of the free energy density. There is a second derivative with respect to each component in the mixture as well as cross components (i.e. mixed derivatives). This matrix is known as the Hessian matrix $\mathbf{H}$

$$\mathbf{H} = \begin{bmatrix} \frac{\partial^2 \psi}{\partial (\rho^A)^2} & \frac{\partial^2 \psi}{\partial \rho^B \partial \rho^A} \\ \frac{\partial^2 \psi}{\partial \rho^A \partial \rho^B} & \frac{\partial^2 \psi}{\partial (\rho^B)^2} \end{bmatrix} \qquad (3.15)$$

By definintion, the first density derivative of a free energy density is a chemical potential, so the second density derivative of a free energy density reduces to a derivative of a chemical potential

$$\frac{\partial^2 \psi}{\partial (\rho^A)^2} = \frac{\partial \mu^A}{\partial \rho^A}, \qquad \frac{\partial^2 \psi}{\partial (\rho^B)^2} = \frac{\partial \mu^B}{\partial \rho^B}, \qquad \frac{\partial^2 \psi}{\partial \rho^B \partial \rho^A} = \frac{\partial \mu^A}{\partial \rho^B}, \qquad \frac{\partial^2 \psi}{\partial \rho^A \partial \rho^B} = \frac{\partial \mu^B}{\partial \rho^A} \tag{3.16}$$

so our Hessian can be simplified to

$$\mathbf{H} = \begin{bmatrix} \frac{\partial \mu^A}{\partial \rho^A} & \frac{\partial \mu^A}{\partial \rho^B} \\ \frac{\partial \mu^B}{\partial \rho^A} & \frac{\partial \mu^B}{\partial \rho^B} \end{bmatrix} \tag{3.17}$$

Mathematically, the stability analysis for a multicomponent mixture involves solving an eigenvalue-eigenvector problem of the Hessian. Instead of the signs of the second derivatives themselves, the signs of the eigenvalues of the Hessian indicate if the free energy surface is stable or unstable. When one computes the expressions for $\partial \mu^A / \partial \rho^B$ and $\partial \mu^B / \partial \rho^A$, we find that they are equal. We can make the following substitutions to help simplify the notation of the eigenvalues to come

$$a = \frac{\partial \mu^A}{\partial \rho^A} \qquad b = \frac{\partial \mu^B}{\partial \rho^B} \qquad c = \frac{\partial \mu^A}{\partial \rho^B} = \frac{\partial \mu^B}{\partial \rho^A} \tag{3.18}$$

Setting the determinant of the Hessian equal to zero and solving for the eigenvalues, we find that two eigenvalues exist for our mixture of two components

$$\begin{vmatrix} a - \lambda & c \\ c & b - \lambda \end{vmatrix} = (a - \lambda)(b - \lambda) - c^2 = \lambda^2 + (-a - b)\lambda + (ab - c^2) = 0$$

$$\therefore \quad \lambda^{(1)} = \frac{1}{2} \left[(a + b) + \sqrt{(a - b)^2 + 4c^2} \right] \tag{3.19}$$

$$\lambda^{(2)} = \frac{1}{2} \left[(a + b) - \sqrt{(a - b)^2 + 4c^2} \right] \tag{3.20}$$

If the sign of either one of these eigenvalues is negative, the mixture given by (ρ^A, ρ^B) is unstable and can be expected to phase separate.

The eigenvalues of the Hessian identify the unstable regions of a free energy surface, of which Figure 3.3 is an example. An example mixture in the middle of the plait in Figure 3.3 is on the free energy density surface at a point with negative curvature (remember, the surface is

36

shown inverted), and that point would separate into phases defined by the sketched binodal line. But which two points on that binodal are the points that our mixture will separate into? This question is equivalent to identifying the tie line along which the surface may be sliced into a curve resembling Figure 3.1. The eigenvector of the Hessian's negative eigenvalue is used to identify the orientation of the tie line, which in turn intersects the binodal at the correct points. Finishing the eigenvalue-eigenvector problem, our two eigenvectors are

$$\vec{x}^{(1)} = \begin{bmatrix} \frac{2c}{b-a+\sqrt{(a-b)^2+4c^2}} \\ 1 \end{bmatrix} \tag{3.21}$$

$$\vec{x}^{(2)} = \begin{bmatrix} \frac{2c}{b-a-\sqrt{(a-b)^2+4c^2}} \\ 1 \end{bmatrix} \tag{3.22}$$

The eigenvector $\vec{x}^{(1)}$ corresponds to the eigenvalue $\lambda^{(1)}$, and likewise for the second eigenvector. Also note that in the course of solving the problem, the definition of the eigenvectors such that the B-component of each equals 1 was an arbitrary choice.

There is one final note for the multicomponent stability analysis. In principle, both of the eigenvalues of a Hessian could be negative, which would indicate that there are multiple tie lines a mixture could follow while phase separating. As will be seen in subsequent sections, there are many phase diagrams where this would intuitively appear to be likely, principally within the 3-phase regions of phase diagrams. To the contrary, in all of the phase diagrams we produced, we only ever observed unstable mixtures with a single negative eigenvalue.

3.5. Minimization Algorithm

There are several computational techniques available to minimize our multicomponent van der Waals free energy in Eq. (2.63). The suitability of a technique is generally driven by how much information one has about the function to be optimized: the ability to compute derivatives of that function, whether or not the function has discontinuities, and the constraints that must be satisfied.

Reference [45] contains descriptions of several C-language optimization algorithms. These algorithms all aim to optimize a function in the most efficient manner possible, which for a computer usually means using as few processor cycles as possible. However, the trade-off to gaining speed is

usually an obfuscation of the underlying process, creating a "black box" that isn't always the best tool to use for developing one's intuition. Many of these algorithms may also fail to converge to a solution.

In this thesis, a primary goal was to prioritize the development of physical intuition above all else. As such, a deliberate decision was made to implement a brute force minimization algorithm to help accentuate the physics of the free energy minimization. A side benefit is that brute force methods are easy to architect in such a way that they will always converge. This "white box" optimization was designed to force the direct manipulation of only the physical degrees of freedom, which are the raw particles numbers of each component and the volumes of each possible phase. The only computational optimizations were to ignore unphysical mixtures (i.e. not possible due to the discontinuity in the VDW equation) and mixtures that were determined to be stable by a stability analysis. All research code and data sets are available at [46].

We generated phase diagrams to visualize the results of a bulk free energy minimization ($\kappa = 0$). For each phase diagram, the critical properties $\theta_c^A, \rho_c^A = 1, \theta_c^B, \rho_c^B$ were chosen, and the VDW compressibility ratio was used to determine p_c^A, p_c^B to fully define the traits of each component. The parameter ν was chosen, Eqs. (2.66), (2.67), and (2.68) set the VDW constants for the two-component mixture $(a^A, a^B, a^{AB}, b^A, b^B)$, and the free energy for the mixture was minimized. A high-level sketch of the free energy minimization algorithm follows:

1. Loop over all (A, B) particle pairs below the line connecting van der Waals discontinuities for each component. A is the number of particles of component A, and B is the number of particles of component B.

2. Perform a stability analysis of the free energy at the point (A, B) via second derivatives with respect to component densities (Eq. 3.15).

   (a) If the point is stable, phase separation is not expected. Continue to the next (A, B) test point in Step 1.

   (b) If the point is not stable, proceed to Step 3 to attempt to minimize the free energy.

3. Initialize the free energy of the mixture, and choose an initial step size by which to vary the particle counts and volumina for each phase.

(a) Assume equal volumina for the 3 allowed phases $(V1, V2, V3)$. For simplicity, we constrain the total volume of the system to equal 1, so each phase is initially allocated $1/3$.

(b) Use the eigenvector associated with the negative eigenvalue to divide the (A, B) particles between phases 1 $(A1, B1)$ and 2 $(A2, B2)$. Phase 3 is initially empty.

4. Create a 6x3 array of free energy trial values.

   (a) For the 6 physical degrees of freedom (phase 1: $A1, B1, V1$; phase 2: $A2, B2, V2$), vary each independently by a positive, negative, and neutral step.

   (b) Determine phase 3 $(A3, B3, V3)$ by applying the conservation statements $N_A = A1 + A2 + A3$, $N_B = B1 + B2 + B3$, $V = V1 + V2 + V3$.

5. Evaluate the free energy trial array to see if the minimum free energy in the array is less than that of the current particle/volume phase combinations.

   (a) If the the array has a new minimum free energy, declare that a phase change has occurred and save the associated particle/volume combination. Keep the current step size and return to Step 4 for the next iteration.

   (b) If the minimum free energy is unchanged, halve the step size used to populate the free energy trial array and return to Step 4 for the next iteration.

   (c) Declare the free energy has been sufficiently minimized when the change in free energy is less than a chosen threshold (we use a threshold of 10^{-12}). Continue to Step 6.

6. Divide the particle counts for each component by the volumina of each phase to create the resulting densities of each phase. Examine the densities that correspond to the minimum free energy to classify the resulting phase behavior.

   (a) If there was no phase change, return to Step 1 to evaluate the next (A,B) pair.

   (b) If a stability analysis of the resulting densities shows a phase is still unstable, adjust the particles allocated to each phase to attempt another minimization. We make this adjustment by packing the two stable phases together - which in this implementation

have densities equal to 10^{-4} - into phase 1 and go to Step 3 to split the unstable phase according to its unstable eigenvector for additional minimization iterations.

(c) If the phase change resulted in 2 or 3 stable phases, log the associated particle/volume data for use in creating the phase diagram for the mixture. Go to Step 1 to evaluate the next (A, B) particle pair.

We must note that our specific implementation contains an unphysical effect that causes the algorithm to occasionally identify metastable 2-phase and 3-phase points that lie on the same tie line, leading to a contoured appearance to the three-phase region of some phase diagrams. Slight modifications to the direction of phase separation (Step 3b above) resulted in changes to the 3-phase contours. However, all implementations correctly identified where unconditionally unstable 3-phase behavior was to be expected, and the contours never strayed outside of the full three-phase region. Since metastability within the three-phase region by definition means a mixture can exhibit 2-phase behavior, we chose to identify a mixture as a 3-phase point in our phase diagrams only if it predicts unconditionally unstable behavior.

3.6. Multicomponent Phase Diagrams

To comprehensively test our method, we created phase diagrams for several two-component mixtures spanning a range of component properties to which we could compare a series of LB simulations. All of the LB simulations are on an isothermal lattice with a constant mixture volume, so the natural way to present our data is to plot coexistence curves on a density-density plane (Component A Density vs. Component B Density). Since every point on this plane represents a mixture that in principle exists with its own equilibrium pressure, our graphs essentially represent an isothermal slice from a more conventional pressure-temperature phase diagram for a binary mixture.

Our two-component phase diagrams are also easily related to the taxonomy first developed by van Konynenburg and Scott [25, 26] (K&S), which classifies phase behavior based on characteristics of pressure-temperature (P-T) phase diagrams. They define five classes of behavior based on the number of critical lines, the existence of a line of 3-phase behavior, the intersections of critical and 3-phase lines, and the existence of upper and/or lower critical end points (please see the references for further details). Because of the fundamental differences between P-T phase diagrams

and our density-density phase diagrams, we cannot explicitly visualize the features used by K&S to define their taxonomy. However, Figure 3.6 has been adapted from [4] to outline where the phase diagrams that follow fall within the context of their classification.
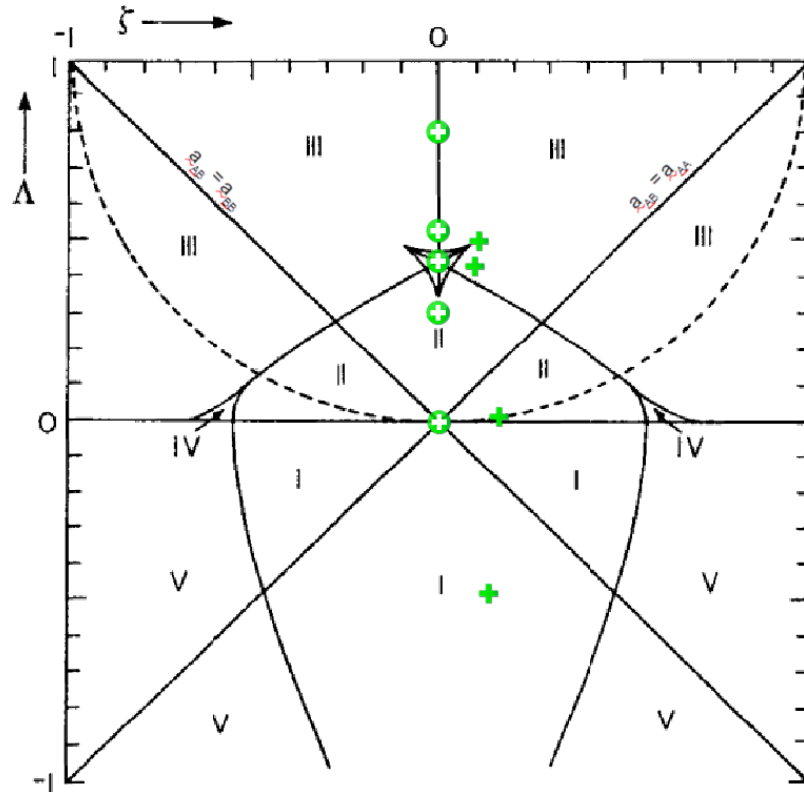
Figure 3.6. The global phase diagram for a binary van der Waals fluid mixture shows five regions (I-V) reproducible by the VDW EOS with cross symbols approximating the state of phase diagrams depicted in this thesis. The 5 open symbols along the constant value $\zeta = 0$ (i.e. along a vertical from the origin up through the center of the figure) indicate symmetric mixtures with equal molecular sizes for each component ($\xi = 0$), and the 4 solid symbols with positive ζ values indicate asymmetric mixtures for unequal molecular sizes ($\xi \neq 0$). The dashed curve depicts neutral cross-component interactions ($\nu = 1$) for the geometric mixing rule in Eq. (2.68). Azeotropy is not relevant to the current study and is not depicted here. See Chapter 6 for all phase diagrams and the LB simulation results for each. Adapted from [4].

The following three parameters are used to classify phase diagrams in the K&S taxonomy

$$\xi = \frac{b^B - b^A}{b^A + b^B} \tag{3.23}$$

$$\zeta = \left(\frac{a^B}{(b^B)^2} - \frac{a^A}{(b^A)^2} \right) \bigg/ \left(\frac{a^A}{(b^A)^2} + \frac{a^B}{(b^B)^2} \right) \tag{3.24}$$

$$\Lambda = \left(\frac{a^A}{(b^A)^2} - \frac{2a^{AB}}{b^A b^B} + \frac{a^B}{(b^B)^2} \right) \bigg/ \left(\frac{a^A}{(b^A)^2} + \frac{a^B}{(b^B)^2} \right) \tag{3.25}$$

The relative molecular size is characterized by ξ, with equal sizes corresponding to $\xi = 0$. This is reflected in Figure 3.6 by the symmetry about the $\zeta = 0$ vertical axis. For non-zero values of ξ, the vertical axis shifts left or right and the regions for each phase diagram type compress or expand accordingly. However, the relationships among phase diagram types remain the same. In our case specifically, the values of ξ given by our parameter choices were $-0.1 <= \xi <= 0$, which has a negligible effect on the layout of Figure 3.6. The parameter ζ is recognized as a relative difference in critical pressures between the two components when one recalls the VDW critical pressure definition $p_c = a^c/27(b^c)^2$. And given the dependence on the cross-component interaction parameter a^{AB}, the parameter Λ can be seen as a measure of the strength of the interaction between components. For $\Lambda > 0$ the interaction is repulsive, and vice versa, given the original approximation used by van der Waals for a^{AB} [3, 25]. Although we used a different mixing rule to generate a^{AB} (Eq. 2.68), Λ is still a good predictor of interaction strength for our work as well given the narrow slice of ζ that our phase diagrams explore.

At this point we note that although we were able to sample a variety of Λ values, our ability to sample a wide array of ζ values was limited, as can be seen in Figure 3.6. This was due to the dependence of the $a^{cc'}$ and b^c parameters on the critical temperatures of the components. Moderate to large values of ζ drove the selection of critical temperatures that very quickly lead to instability of the LB simulations. We were able to remedy the issue somewhat by application of stabilization methods outlined later in this section, but low values of ζ were the only ones that were able to be automated reliably.

We use Figure 3.7 as a baseline example of a free energy minimization. In all graphs that follow, binodal lines are all depicted by solid black lines and indicate the theoretical values the densities of separated phases can be expected take. The edges of the light grey regions approximate the

spinodal regions, which we refer to as quasi-spinodals since discrete implementations are not exact. The quasi-spinodals delineate regions where a homeogeneous mixture at the given temperature and pressure can be expected to be unconditionally unstable towards phase separation.
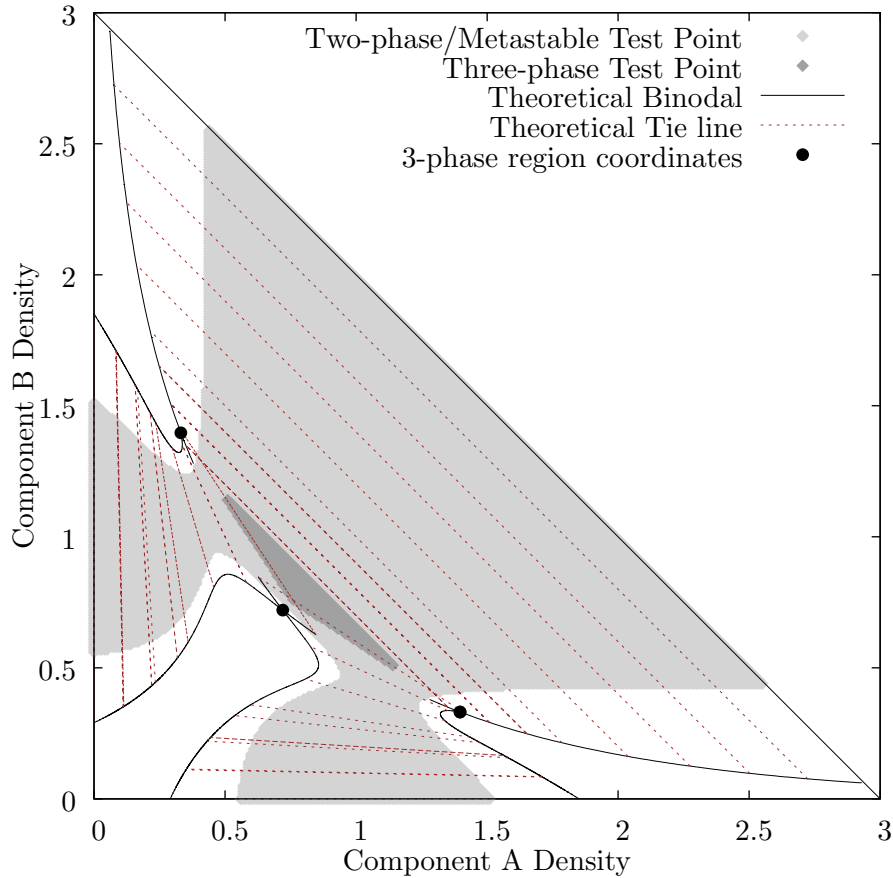
Figure 3.7. A phase diagram for a binary mixture of VDW fluids. The horizontal axis is the density of Component A, and the vertical axis is the density of Component B. This phase diagram can be used to predict single-phase, 2-phase, metastable, and 3-phase behavior.

The kind of phase separation that can be expected - and whether or not a phase is metastable - depends on where on the phase diagram the mixture is located in its homogeneous state. If the mixture begins between two and only two binodals in the quasi-spinodal region, then 2-phase behavior is expected. Phase separation should proceed along a tie line, the end points of which terminate on the two binodals that indicate the A- and B-component densities in each phase. However, if the mixture starts out between the binodal and quasi-spinodal, metastable behavior is expected, and a large enough fluctuation is needed to initiate nucleation.

Closer examination of Figure 3.7 shows that the binodals defining each of the three main regions of the phase diagram actually intersect at the points where regions merge. These intersections are highlighted by the black circles in the figure, which correspond to the theoretical densities for 3-phase behavior. These three points are also the vertices of a triangle that inscribe a region where 3-phase behavior can be expected. After intersecting, binodals continue until they terminate at the quasi-spinodal region. The tie lines that exist at the ends of each of the three pairs of binodals in Figure 3.7 trace out the dark grey region, within which a mixture is anticipated to be unconditionally unstable towards 3-phase behavior. But if a mixture begins in the light grey portion of the 3-phase region, 2-phase metastable behavior is initially expected, and a strong-enough fluctuation will provoke the formation of a third phase. The structural details of the three-phase region are further highlighted in Figure 6.6.

The crossing of binodal lines was at first very surprising. Our intuition was that when phase diagram regions merged, their respective binodals would connect smoothly and result in a single, continuous line. Several literature searches failed to turn up any descriptions of intersecting binodals, but the history of the development of fluid mixing physics as told by Sengers [3] was - once found - an invaluable resource and was heavily referenced. One has to look back to van der Waals himself, who first indirectly raised the possibility of crossing binodals in his description of multiple "plaits", or folds, on a free energy surface [47]. But the first full description of this phenomena and a relation to metastability was given by Korteweg, a mathematician and close friend of van der Waals [3, 27]. The Korteweg description appears to be the only complete description. Other Dutch contemporaries of van der Waals - most noteable theoretical chemist van Laar [41, 48] - had discovered all types of phase diagrams describable by the van der Waals equation of state by the early 20th century. However, due mostly to the inaccuracy of the van der Waals equation of state when compared to alternatives (e.g. Peng-Robinson, Redlich-Kwong), the Korteweg knowledge seems to have been mostly forgotten. Scott and van Konynenburg, who first characterized a global phase diagram for the van der Waals Equation of state using numerical methods in 1968 [25, 26], reference the early Dutch work save that of Korteweg. Since their work explictly considers only stable regions of a phase diagram, neither intersecting binodals nor metastability are pertinent and are thus not mentioned. Aside from that, a small slice of the work of physicist Meijer [28, 29, 30, 31, 32, 33] in the 1990s used numerical methods to confirm the majority of the early Dutch work;

this work appears to be the only modern account of this phenomena which cites Korteweg. To our knowledge, we are the first to apply the lattice Boltzmann method to such a description of phase diagrams.

In investigating the robustness of the method, we generated almost two dozen phase diagrams with varying degrees of asymmetry, quench depths, and interaction strengths between the two components. Only a subset of our examples predict 3-phase behavior, but all predict 2-phase behavior. A representative set of the recovered phase diagrams are depicted relative to the Scott and van Konynenburg global phase diagram in Figure 3.6; the details of each are shown in Chapter 6, Figures 6.8 through 6.13. In terms of the Scott and van Konynenburg classification [25, 26], our phase diagrams cover Types I (Figure 6.10), II (Figures 6.5 and 6.8), and III (Figures 6.6, 6.9, 6.7, 6.11). Figure 6.4 is on the boundary of Types I and II. Finally, Figures 6.12 and 6.13 border Types II and III in the "shield" region, which is the enclosed region around $\zeta = 0, \Lambda = 0.4364$ in Figure 3.6 where 4-phase behavior for a binary mixuture is theoretically possible [4].

4. LATTICE BOLTZMANN THEORY

Chapters 2 and 3 have laid the physical groundwork for why mixtures of van der Waals fluids phase separate and how the minimization of the underlying free energy can be used to predict the phase separation behavior. We now transition to describe the theoretical basis of our tool of choice to model phase separation behavior, lattice Boltzmann.

A great deal of this chapter is referenced to [49] and to other references contained within. We begin the chapter with an overview of kinetic theory concepts necessary to develop the Boltzmann equation. We proceed to derive the continuous hydrodynamic conservation equations that can be represented by the Boltzmann equation, and we follow by presenting the discrete equivalents. We conclude this chapter by specifically detailing the one-dimensional lattice Boltzmann model for the single- and multicomponent cases that the present research is based on.

4.1. Kinetic Theory

The ability of a fluid to separate into multiple phases was described using equilibrium statistical mechanics and thermodynamics in Chapter 2. However, although our simulations are of systems near equilibrium, they are still fundamentally non-equilibrium models, and we must account for the dynamic behavior of the system.

The principles of kinetic theory apply [50]. This section resumes the microscopic discussion of a particle distribution function from Chapter 2 and describes how the distribution evolves with the Boltzmann Transport Equation. We outline the equilibrium state that is achieved by the particle distribution function, and we finally show how these dynamics are equivalent to the well-known equations of macroscopic fluid motion.

4.1.1. Particle Distribution Function

The kinetic theory background needed to develop lattice Boltzmann (LB) actually takes us back to Section 2.1.1 [36]. In that section, the probability Eq. (2.6) from which the statistical mechanics of interacting fluids was defined was a function of only the spatial variables r_α^N. Now, we keep the dependence on particle momenta p_α^N and also specify the time dependence to definea more general probability. Making use of the partition function Eq. (2.20) and a time-dependent

Hamiltonian for N particles, we have

$$P(r_\alpha^N, p_\alpha^N, t) = \frac{e^{-\beta H(r_\alpha^N, p_\alpha^N, t)}}{\mathcal{Z}} \tag{4.1}$$

which, like all probabilities, is normalized to $\int P(r_\alpha^N, p_\alpha^N, t) dr^N dp^N dt = 1$.

We can similarly expand our earlier definition of a single-particle distribution function to depend on both position and momenta

$$f(r_\alpha, p_\alpha, t) = N \int P(r_\alpha^N, p_\alpha^N, t) dr^{N-1} dp^{N-1} \tag{4.2}$$

by integrating out the positions and momenta of all particles except a single reference particle, and the prefactor N is because the particles are indistinguishable. Other distribution functions such as the two-particle distribution function $f^{(2)}$ can also be extended in this manner. If we integrate Eq. (4.2) over the position and momentum of the reference particle at time t, we get

$$\int f(r_\alpha, p_\alpha, t) dr dp = N \tag{4.3}$$

which is the total number of particles in our system. It is in this fashion that the statistical moments of the single-particle distribution function are the connections between kinetic theory and the physical world.

As before, we restrict our analysis to a mesoscopic perspective where the size of a control volume is small enough that macroscopic features are resolved yet large enough to contain on the order of 10^{23} particles. This restriction implies that once a control volume comes to a local equilibrium, the fluid can be treated independent of position. This gives

$$\int dr \int f(r_\alpha, p_\alpha, t) dp = N$$
$$V \int f(r_\alpha, p_\alpha, t) dp = N$$
$$\int f(r_\alpha, p_\alpha, t) dp = n(r_\alpha) \tag{4.4}$$

where $n(r_\alpha)$ is the number density. We simplify the notation going forward by dropping the explicit position dependence of our local quantities.

It is common to find the moments of the distribution function f given in terms of velocity v_α rather than momentum. The only difference would be that our normalization condition is defined in terms of velocity instead of momentum, and we arrive at the same result. In terms of velocity, this gives what is referred to as the zeroth moment of the distribution function

$$\int f(r_\alpha, v_\alpha, t)dv = n \tag{4.5}$$

By demanding that the higher velocity moments equal specific values, we can impose additional constraints on the system that connect the distribution function to corresponding physical principles. The first velocity moment is used to demand that in a uniform system, fluctuations about the mean velocity average out to nothing. The deviation of a particle's velocity from the mean $(v_\alpha - u_\alpha)$ - known as the peculiar velocity - is used to construct the higher order moments. Under this restriction, the first velocity moment becomes

$$\int f(r_\alpha, v_\alpha, t)(v_\alpha - u_\alpha)dv = 0$$
$$\int f(r_\alpha, v_\alpha, t)v_\alpha dv - \int f(r_\alpha, v_\alpha, t)u_\alpha dv = 0$$
$$\int f(r_\alpha, v_\alpha, t)v_\alpha dv = u_\alpha \int f(r_\alpha, v_\alpha, t)dv$$
$$\int f(r_\alpha, v_\alpha, t)v_\alpha dv = nu_\alpha \tag{4.6}$$

where we have used Eq. (4.5). We can also recognize that the first velocity moment is also equivalent in form to a statistical expectation value, in this case $\langle v \rangle$. This defines our average macroscopic velocity u_α and connects the particle distribution to the fluid's momentum.

Finally, we want to connect the distribution function to energy. We can start by using the peculiar velocity in the definition of kinetic energy and calculating the expectation value

$$
\begin{aligned}
\int f(r_\alpha, v_\alpha, t)\frac{1}{2}m(v_\alpha - u_\alpha)^2 dv &= \frac{1}{2}m\int f(r_\alpha, v_\alpha, t)(v_\alpha v_\alpha - 2v_\alpha u_\alpha + u_\alpha u_\alpha)dv \\
&= \frac{1}{2}mn\langle v^2 \rangle - mnu_\alpha\langle v_\alpha \rangle + \frac{1}{2}mnu^2 \\
&= \frac{1}{2}\rho\left(\langle v^2 \rangle - u^2\right)
\end{aligned}
\tag{4.7}
$$

where we have used the definition of an expectation value and the fact $\langle v_\alpha \rangle = u_\alpha$. The quantity in parenthesis in Eq. (4.7) is statistically the variance of the energy distribution, i.e. the width of the energy distribution, which is an expression of temperature. We can use this fact to leverage the equipartition theorem to identify the velocity variance in terms of the temperature $\theta = k_B T$

$$
\frac{3}{2}\theta = \frac{1}{2}m\langle (v_\alpha - u_\alpha)^2 \rangle
\tag{4.8}
$$

$$
\frac{3\theta}{m} = \langle v^2 \rangle - u^2
\tag{4.9}
$$

and finalize the distribution function-to-energy connection

$$
\begin{aligned}
\int f(r_\alpha, v_\alpha, t)\frac{1}{2}m(v_\alpha - u_\alpha)^2 dv &= \frac{1}{2}\rho(\frac{3\theta}{m}) \\
m\int f(r_\alpha, v_\alpha, t)v_\alpha v_\alpha dv - \rho u_\alpha u_\alpha &= 3\rho\theta \\
\int f(r_\alpha, v_\alpha, t)v^2 dv &= nu^2 + 3n\theta
\end{aligned}
\tag{4.10}
$$

In a slightly indirect manner, the square velocity moment given by Eq. (4.10) enforces adherence to the equipartition theorem.

It is important to note that at this point, the moments defined are for a general, non-equilibrium particle distribution function. We will now explore how this non-equilibrium distribution evolves in time and space.

4.1.2. Boltzmann Transport Equation

The derivation of the Boltzmann Transport Equation (BTE) begins with the Liouville equation from statistical mechanics

$$\frac{d\rho^{(N)}}{dt} = 0 \tag{4.11}$$

which governs the evolution of a full N-particle distribution function $\rho^{(N)}$ through phase space. The Liouville equation is a fully general and exact description of the evolution of the N-particle distribution function. However, its dependence on $6N$ variables (position and velocity components for each of the N particles) is not at all practical.

At its core, the construction of the single-particle distribution function $f \equiv f(r_\alpha, v_\alpha, t)$ we use is a useful simplification of the N-particle distribution function [51, 52]. It can be shown that f is related to the two-particle distribution function $f^{(2)}$, which in turn is related to the three-particle distribution function $f^{(3)}$ and so on. Reference [50] contains a detailed description about how these relations form a hierarchy of equations known as the BBGKY hierarchy (Bogoliubov, Born, Green, Kirkwood, and Yvon) that can be truncated to arrive at the Boltzmann Transport Equation (BTE)

$$\partial_t f + v_\alpha \nabla_\alpha f + \frac{F_\alpha}{m} \partial_{v_\alpha} f = \Omega_f \tag{4.12}$$

where a general term Ω_f is introduced to capture the effects of particle collisions caused by the dependence of f on $f^{(2)}$. These collisions cause friction, which is a non-conservative force that gives rise to viscosity.

The collision term Ω_f can be represented in several ways. Boltzmann initially considered the mechanics of colliding objects and defined Ω_f as an integral over all possible ways two specific reference particles can collide [50, 53]. The BBGKY hierarchy expresses an integral involving the two-particle distribution function explicitly [50, 54]. Strictly speaking, the original Boltzmann collision integral applies only to a rarified gas. Both of these approaches share the disadvantage of being very difficult to explicitly solve, sometimes impossible. For our purposes, we adopt the common BGK (Bhatnagar, Gross, and Krook) approximation

$$\Omega_f = \frac{1}{\tau}(f^0 - f) \tag{4.13}$$

which embodies the simple logic based on the 2nd law of thermodynamics that all collisions serve to relax the distribution function f to some local equilibrium, given by f^0. The rate of relaxation is given by the constant τ.

With this approximation for Ω_f, the form of the BTE that we shall use for the remainder of this thesis is

$$\partial_t f + v_\alpha \nabla_\alpha f + \frac{F_\alpha}{m} \partial_{v_\alpha} f = \frac{1}{\tau}(f^0 - f) \tag{4.14}$$

4.1.3. Maxwell-Boltzmann Distribution

The form of the local distribution function f^0 that is a solution to the BTE must be determined. We begin with Boltzmann's $\mathcal{H}$-functional [50, 55, 56]

$$\mathcal{H} = \int f \ln f \, dv \tag{4.15}$$

which is a quantity that is minimized as collisions in a fluid occur and a system relaxes from f to an equilibrium given by f^0. The quantity $\mathcal{H}$ can be thought of as an entropy-like quantity that changes monotonically as a system evolves, only it is minimized instead of maximized. We can determine the form of f^0 by using the method of Lagrange multipliers to analytically minimize Eq. (4.15) given the physical constraints of mass, momentum, and energy conservation.

The variational form of $\mathcal{H}$ to minimize is - since f is a function of several variables - given by the functional derivative of Eq. (4.15) with respect to f

$$\frac{\delta \mathcal{H}}{\delta f} = 0 = \frac{\delta}{\delta f} \int f \ln f \, dv$$
$$0 = \int [1 + \ln f] \delta f \, dv \tag{4.16}$$

The derivatives of the conserved quantities with respect to f is also zero (i.e. conserved quantities are constant). Our expressions for the conservation laws are given by the moments of the distribution function f in Eqs. (4.5), (4.6), and (4.10). Taking the derivative of each conservation equation

and using the Lagrange multipliers $\lambda_1, \lambda_{2\alpha}$(a vector)$, \lambda_3$, we can add the constraints to Eq. (4.16)

$$0 = \int [1 + lnf]\delta f dv - \lambda_1 \int \delta f dv - \lambda_{2\alpha} \int \delta f v_\alpha dv - \lambda_3 \int \delta f v^2 dv$$

$$0 = \int [1 + lnf - \lambda_1 - \lambda_{2\alpha}v_\alpha - \lambda_3 v^2]\delta f dv \qquad (4.17)$$

Since the variation δf is by definition a non-zero value, the term in brackets must equal zero

$$0 = 1 + lnf - \lambda_1 - \lambda_{2\alpha}v_\alpha - \lambda_3 v^2 \qquad (4.18)$$

Rearranging for lnf, defining a new constant $c = \lambda_1 - 1$, and completing the square, we get

$$lnf = c - \frac{\lambda_{2\alpha}\lambda_{2\alpha}}{4\lambda_3} + \lambda_3 \left(v_\alpha + \frac{\lambda_{2\alpha}}{2\lambda_3} \right)^2 \qquad (4.19)$$

Combining constants as

$$lnA = c - \frac{\lambda_{2\alpha}\lambda_{2\alpha}}{4\lambda_3} \qquad (4.20)$$

$$b_\alpha = -\frac{\lambda_{2\alpha}}{2\lambda_3} \qquad (4.21)$$

and exponentiating, we have

$$f = Ae^{\lambda_3(v_\alpha - b_\alpha)^2} \qquad (4.22)$$

This equation is of the Maxwell-Boltzmann form, but we have three constants that need to be determined - A, b_α, and λ_3. The three moments of the distribution function f we determined in Eqs. (4.5), (4.6), and (4.10) can be used to resolve them.

Substituting the form of f from Eq. (4.22) into the zeroth moment, Eq. (4.5), using the substitution $c_\alpha = v_\alpha - b_\alpha$, and performing the three Gaussian integrals (one for each velocity coordinate) allows us to identify

$$n = \int Ae^{\lambda_3 c_\alpha^2} dc_\alpha = A \left(\frac{\pi}{\lambda_3} \right)^{\frac{3}{2}} \qquad (4.23)$$

We will move on for the moment; this form will come in handy shortly.

Substituting Eq. (4.22) into the first moment, Eq. (4.6), and using the same substitution for c_α (while remembering that b_α is a constant) gives

$$
nu_\alpha = \int A e^{\lambda_3 (c_\alpha)^2} (c_\alpha + b_\alpha) dc_\alpha
$$
$$
u_\alpha = \frac{A}{n} \int e^{\lambda_3 c_\alpha^2} c_\alpha dc_\alpha + \frac{A b_\alpha}{n} \int e^{\lambda_3 c_\alpha^2} dc_\alpha \tag{4.24}
$$

The first integral is an odd integral of c_α and evaluates to zero. However, the second integral - when paired with the constant A - equals n. After cancellation, we can identify the average velocity as

$$
u_\alpha = b_\alpha \tag{4.25}
$$

We now substitute Eq. (4.22) into the energy moment from Eq. (4.10). Rearranging to cast it in terms of the peculiar velocity and using our new definition of the average velocity u_α, we have

$$
\frac{3}{2} n\theta = \int A e^{\lambda_3 (v_\alpha - u_\alpha)^2} \frac{1}{2} m (v_\alpha - u_\alpha)^2 dv
$$
$$
3n\theta = Am \int c_\alpha^2 e^{\lambda_3 c_\alpha^2} dc_\alpha
$$
$$
3n\theta = Am \left(\frac{1}{2} \sqrt{\frac{\pi}{\lambda_3}} \right)^3 \tag{4.26}
$$

Between Eqs. (4.23) and (4.26), we now have two equations for our remaining two undetermined constants, A and λ_3. Solving this system lets us identify the values of each and fully define the Maxwell-Boltzmann distribution, which we denote by f^0

$$
f^0(r_\alpha, v_\alpha) = n \left(\frac{m}{2\pi\theta} \right)^{\frac{3}{2}} e^{-\frac{m(v_\alpha - u_\alpha)^2}{2\theta}} \tag{4.27}
$$

We note that the exponent of the normalization constant, $D/2$, is formally determined by the dimensionality of our system D. In this case, we have determined the value for a 3-dimensional system $D = 3$. It is also noteworthy that Maxwell-Boltzmann distribution is often defined in the context of the probability that a *single* particle is at a given velocity. In our case, the prefactor of the average number density n means this particular version of the distribution applies to a group

of particles in a control volume centered on r_α, which will map conceptually to the definition of a lattice site in Section 4.2.2.

For the remainder of this thesis, we shall refer to the 1-dimensional version of f^0 with the additional simplifying assumption that $m = 1$

$$f^0(r_\alpha, v_\alpha) = \frac{n}{(2\pi\theta)^{\frac{3}{2}}} e^{-\frac{(v_\alpha - u_\alpha)^2}{2\theta}} \tag{4.28}$$

Eq. (4.28) is the local equilibrium distribution we use for the upcoming LB simulations by way of the BGK collision term in the BTE (refer to Eq. 4.14). However we do not as of yet have all of the tools we need to determine what the exact equations of motion will be simulated in our model. To do this, we need the velocity moments of the local equilibrium distribution f^0.

4.1.3.1. Moments of the Maxwell-Boltzmann Distribution

The moments of the Maxwell-Boltzmann distribution are critical to deriving the equations of motions that our LB model simulate. To ensure conservation of mass and momentum, the first two moments of f^0 must be identical to the first two moments of f

$$\int f^0 dv = n \tag{4.29}$$

$$\int f^0 (v_\alpha - u_\alpha) dv = 0 \tag{4.30}$$

For the second order moment, we begin by defining it as such in terms of the peculiar velocity

$$\int f^0 (v_\alpha - u_\alpha)(v_\beta - u_\beta) dv = n\theta\delta_{\alpha\beta} \tag{4.31}$$

which can be algebraically rearranged to

$$\int f^0 v_\alpha v_\beta dv = nu_\alpha u_\beta + n\theta\delta_{\alpha\beta} \tag{4.32}$$

This is equivalent to defining the pressure on each face of our control volume by use of the ideal gas equation of state ($p = n\theta$). This result can be directly determined by substituting the Maxwell-Boltzmann distribution into Eq. (4.31) and directly evaluating the Gaussian integrals. However,

we can develop an intuition for the physical justification of this definition by imagining an arbitrary surface dS placed inside of our control volume [56].

The rate at which mass flows across the surface is given by the density ρ, the area of our surface dS, and the velocity of n that is normal to the surface, which we define as v_β

$$\frac{dm}{dt} = \langle \rho \vec{v}.\hat{n}dS \rangle = \rho dS \langle v_\beta \rangle \tag{4.33}$$

The momentum flow is the mass flow times the momentum carried for each unit of mass ($mv_\alpha/m = v_\alpha$). So the rate at which momentum carried by the particles across dS is simply

$$\frac{d\vec{p}}{dt} = \rho dS \langle v_\beta (mv_\alpha/m) \rangle = \rho dS \langle v_\alpha v_\beta \rangle \tag{4.34}$$

which defines the momentum flux tensor

$$\Pi_{\alpha\beta} = \frac{d\vec{p}}{dtdS} = \rho \langle v_\alpha v_\beta \rangle \tag{4.35}$$

By definition, the elements of this tensor have units of force per unit area, which is equivalent to pressure. Moreover, since the Maxwell-Boltzmann distribution is an equilibrium distribution, the velocities are isotropic. The uniform velocities mean that the momentum flux tensor has non-diagonal elements equal to zero and all diagonal elements are equal to each other, meaning

$$\Pi_{\alpha\beta} \equiv P_{\alpha\beta} = P\delta_{\alpha\beta} \tag{4.36}$$

where P is the total pressure on a given face of our control volume. We recognize that the velocity v_α is made up of two parts, a mean velocity u_α and a deviation from that mean c_α. This allows us to separate the total pressure into two parts

$$\begin{aligned} P_{\alpha\beta} &= \rho \langle (u_\alpha + c_\alpha)(u_\beta + c_\beta) \rangle \\ &= \rho(u_\alpha u_\beta + u_\alpha \langle c_\beta \rangle^{0} + u_\beta \langle c_\alpha \rangle^{0} + \langle c_\alpha c_\beta \rangle) \\ &= \rho \langle c_\alpha c_\beta \rangle + \rho u_\alpha u_\beta \end{aligned} \tag{4.37}$$

The first term in Eq. (4.37) *is* Eq. (4.31) by definition of an expectation value with respect to the particle distribution, which connects the second order moment to pressure. In addition, we know the first term can only refer to a scalar pressure p since $\alpha = \beta$ are the only terms present because of isotropy, so

$$\int f^0 (v_\alpha - u_\alpha)(v_\beta - u_\beta) dv = p\delta_{\alpha\beta} \tag{4.38}$$

By making use of the ideal gas equation of state $p = n\theta$, we can make a simple substitution to arrive at Eq. (4.31).

The third order velocity moment is in general equal to a rank 3 tensor

$$Q_{\alpha\beta\gamma} = \int f^0 (v_\alpha - u_\alpha)(v_\beta - u_\beta)(v_\gamma - u_\gamma) dv \tag{4.39}$$

However, given the assumption of perfectly isotropic velocities in equilibrium, this is an odd integral; therefore, it must equal zero. In systems where this assumption does not hold, the resulting dynamics may violate Galilean invariance. We use that fact to simplify the third moment as follows

$$\int f^0 (v_\alpha - u_\alpha)(v_\beta - u_\beta)(v_\gamma - u_\gamma) dv = 0$$

$$\int f^0 (v_\alpha v_\beta v_\gamma - u_\alpha v_\beta v_\gamma - v_\alpha u_\beta v_\gamma - v_\alpha v_\beta u_\gamma$$

$$+ u_\alpha u_\beta v_\gamma + v_\alpha u_\beta u_\gamma + u_\alpha v_\beta u_\gamma - u_\alpha u_\beta u_\gamma) dv = 0$$

$$\int f^0 v_\alpha v_\beta v_\gamma dv = \rho u_\alpha u_\beta u_\gamma + \rho\theta(u_\alpha \delta_{\beta\gamma} + u_\beta \delta_{\alpha\gamma} + u_\gamma \delta_{\alpha\beta}) \tag{4.40}$$

With these moments of our equilibrium distribution defined, we are ready to prove that our simulations that use the BTE will actually be modelling well-known hydrodynamic conservation equations: the continuity equation and the Navier-Stokes momentum equations.

4.1.4. Hydrodynamic Conservation Equations

The Boltzmann equation can be shown to be identically equivalent to the fluid flow conservation equations. This process can be generalized by deriving a master equation of motion for any given quantity Q [51]. The master moment equation can then be used to determine the full set of

equations of motion by mapping a conserved physical quantity of interest (particle number, mass, momentum, energy) to Q, substituting, and integrating the transport equation.

4.1.4.1. Master Moment Equation

In general, starting with equation 4.14 and using Q to represent a generalized moment

$$\int Q\left(\partial_t f + v_\alpha \nabla_\alpha f + F_\alpha \partial_{v_\alpha} f\right) dv = \int Q\Omega dv$$

$$\int Q\partial_t f dv + \int Qv_\alpha \nabla_\alpha f dv + \int QF_\alpha \partial_{v_\alpha} f dv = \int Q\Omega dv \tag{4.41}$$

When Q is a conserved moment - such as mass, momentum, and energy - it can be shown that the right hand side of the above is always equal to zero. And it also follows logically since the particle collisions must not add to or take away from any conserved quantity.

$$\int Q\partial_t f dv + \int Qv_\alpha \nabla_\alpha f dv + \int QF_\alpha \partial_{v_\alpha} f dv = 0 \tag{4.42}$$

On the left hand side, the first integral is simplified by realizing that neither Q nor f have a time dependence, so it may be pulled outside of the integral. What remains can be simplified by using the definition of an expectation value:

$$\int Q\partial_t f dv = \partial_t \int Qf dv = \partial_t\left(n\langle Q\rangle\right) \tag{4.43}$$

The second integral on the left hand side is simplified by realizing that in its present form, it is part of an entire product rule derivative: $\nabla_\alpha\left(Qv_\alpha f\right) = f\nabla_\alpha\left(Qv_\alpha\right) + Qv_\alpha \nabla_\alpha f$, so

$$\begin{aligned}
\int Qv_\alpha \nabla_\alpha f dv &= \int \left[\nabla_\alpha\left(Qv_\alpha f\right) - f\nabla_\alpha\left(Qv_\alpha\right)\right] dv \\
&= \int \nabla_\alpha\left(Qv_\alpha f\right) dv \\
&= \nabla_\alpha\left(n\langle Qv_\alpha\rangle\right) \tag{4.44}
\end{aligned}$$

This holds since for the first step, neither Q nor v_α have positional dependencies, so the gradient of the final term is zero.

57

Finally, the third term is similarly simplified by starting with the realization that it is currently part of an entire product rule derivative: $\partial_{v_\alpha} (QF_\alpha f) = f\partial_{v_\alpha} (QF_\alpha) + QF_\alpha \partial_{v_\alpha} f$, so...

$$
\begin{aligned}
\int QF_\alpha \partial_{v_\alpha} f dv &= \int [\partial_{v_\alpha} (QF_\alpha f) - f\partial_{v_\alpha} (QF_\alpha)] dv \\
&= \int \partial_{v_\alpha} (QF_\alpha f) dv - \int f\partial_{v_\alpha} (QF_\alpha) dv \\
&= [QF_\alpha f]_{-\infty}^{\infty} - \int f\partial_{v_\alpha} (QF_\alpha) dv \\
&= -\int f\partial_{v_\alpha} (QF_\alpha) dv \\
&= -\int fF_\alpha \partial_{v_\alpha} Q dv - \int fQ\partial_{v_\alpha} F_\alpha dv \\
&= -F_\alpha \int f\partial_{v_\alpha} Q dv \\
&= -F_\alpha n \langle \partial_{v_\alpha} Q \rangle
\end{aligned}
\tag{4.45}
$$

Assembling these three pieces, the final moment equation is arrived upon

$$
\partial_t (n\langle Q \rangle) + \nabla_\alpha (n\langle Qv_\alpha \rangle) - F_\alpha n \langle \partial_{v_\alpha} Q \rangle = 0
\tag{4.46}
$$

Using equation 4.46, the conserved moments may be substituted for Q, and the resulting equation of fluid motion may be directly worked out.

4.1.4.2. Mass Conservation

For conserved particle densities ($Q = 1$), a straight integration of the BGK-approximated Boltzmann equation recovers an equation for continuity.

$$
\int \partial_t f dv + \int v_\alpha \partial_{x_\alpha} f dv + \int F_\alpha \partial_{v_\alpha} f dv = \int \frac{1}{\tau}(f^0 - f)dv
\tag{4.47}
$$

$$
\partial_t \int f dv + \partial_{x_\alpha} \int f v_\alpha dv + F_\alpha \int \partial_{v_\alpha} f dv = \frac{1}{\tau}\left[\int f^0 dv - \int f dv\right]
\tag{4.48}
$$

On the left-hand side, the first term is equivalent to n by Equation 4.29, the second equals nu_α (4.30), and the third integral - evaluated from positive to negative infinite limits, evaluates to zero since the forcing term has no velocity dependence.

To explicitly show the conserved moment leads to the collision integral equating to zero on the right-hand side, each term in the brackets also equals n, the subtraction of which yields zero. The result is a continuity equation for mass

$$\partial_t n + \partial_{x_\alpha}(nu_\alpha) + O(\partial^2) = 0, \tag{4.49}$$

or in three dimensions,

$$\partial_t n + \nabla(n\vec{u}) = 0, \tag{4.50}$$

Alternately, the mass continuity equation can be recovered in mass density form by using $Q = m$, $\rho = nm$, and recognizing that the expectation of particle velocity ($\langle v_\alpha \rangle$) is the same as mean velocity (u_α), leading to

$$\partial_t \rho + \nabla_\alpha(\rho u_\alpha) = 0 \tag{4.51}$$

4.1.4.3. Momentum Conservation

Momentum conservation can be shown by using $Q = mv_\alpha$ as the conserved quantity in the moment equation 4.46

$$\partial_t \left(n \langle mv_\alpha \rangle \right) + \nabla_\beta \left(n \langle mv_\alpha v_\beta \rangle \right) - F_\beta n \left\langle \partial_{v_\beta} mv_\alpha \right\rangle = 0$$

$$\partial_t \left(\rho \langle v_\alpha \rangle \right) + \nabla_\beta \left(\rho \langle v_\alpha v_\beta \rangle \right) - F_\beta \rho \left\langle \partial_{v_\alpha} v_\beta \right\rangle = 0$$

$$\partial_t \left(\rho u_\alpha \right) + \nabla_\beta \rho \left\langle v_\alpha v_\beta \right\rangle - \rho F_\beta \delta_{\alpha\beta} = 0$$

$$\partial_t \left(\rho u_\alpha \right) + \nabla_\beta \rho \left\langle v_\alpha v_\beta \right\rangle - \rho F_\alpha = 0 \tag{4.52}$$

So momentum conservation thus far - upon expanding the expectation value remaining in Eq. 4.52 - is

$$\partial_t(\rho u_\alpha) + \nabla_\beta \int f m v_\alpha v_\beta dv - \rho F_\alpha = 0 \tag{4.53}$$

Transformation of the second term on the left hand side is a lengthy exercise, beginning with using the BGK approximation (Eq. 4.13) to eliminate f in favor of the equilibrium distribution f^0. The substitution is made iteratively until the expansion is of the necessary order and higher-order

terms may be neglected. Treating only the integral for the second term

$$\int f m v_\alpha v_\beta dv = m \int \left[f^0 - \tau \left(\partial_t f + v_\gamma \nabla_\gamma f + F_\gamma \partial_{v_\gamma} f \right) \right] v_\alpha v_\beta dv$$

$$= m \int f^0 v_\alpha v_\beta dv - \tau m \partial_t \int f v_\alpha v_\beta dv -$$

$$- \tau m \nabla_\gamma \int f v_\alpha v_\beta v_\gamma dv - \tau m F_\gamma \int \partial_{v_\gamma} f v_\alpha v_\beta dv$$

$$= m \int f^0 v_\alpha v_\beta dv - \tau m \partial_t \int f^0 v_\alpha v_\beta dv -$$

$$- \tau m \nabla_\gamma \int f^0 v_\alpha v_\beta v_\gamma dv - \tau m F_\gamma \int \partial_{v_\gamma} f^0 v_\alpha v_\beta dv + O(\partial^2) \qquad (4.54)$$

The first two integrals can be substituted for by the 2nd order moments shown in 4.31, and the 3rd order moment (4.40) takes care of the third integral. The fourth integral is reduced through partial integration as follows

$$\int \partial_{v_\gamma} f^0 v_\alpha v_\beta dv = [f^0 v_\alpha v_\beta]_{-\infty}^{\infty} - \int f^0 \partial_{v_\gamma} (v_\alpha v_\beta) dv$$

$$= 0 - \int f^0 (\delta_{\alpha\gamma} v_\beta + v_\alpha \delta_{\beta\gamma}) dv$$

$$= -\delta_{\alpha\gamma} \int f^0 v_\beta dv - \delta_{\beta\gamma} \int f^0 v_\alpha dv$$

$$= -n u_\beta \delta_{\alpha\gamma} - n u_\alpha \delta_{\beta\gamma} \qquad (4.55)$$

The momentum conservation thus far is now

$$\partial_t(\rho u_\alpha) + \nabla_\beta[(\rho u_\alpha u_\beta + \rho \theta \delta_{\alpha\beta})$$

$$- \tau \partial_t(\rho u_\alpha u_\beta + \rho \theta \delta_{\alpha\beta})$$

$$- \tau \nabla_\gamma \left(\rho u_\alpha u_\beta u_\gamma + \rho \theta \left(u_\alpha \delta_{\beta\gamma} + u_\beta \delta_{\alpha\gamma} + u_\gamma \delta_{\alpha\beta} \right) \right)$$

$$- \tau F_\gamma \left(-\rho u_\beta \delta_{\alpha\gamma} - \rho u_\alpha \delta_{\beta\gamma} \right) + O(\partial^2)] - \rho F_\alpha = 0 \qquad (4.56)$$

The above may be rearranged to group any collision-oriented term - i.e. those involving τ - on the right hand side

$$\partial_t(\rho u_\alpha) + \nabla_\beta(\rho u_\alpha u_\beta + \rho\theta\delta_{\alpha\beta}) - \rho F_\alpha = \tau\nabla_\beta[\partial_t(\rho u_\alpha u_\beta + \rho\theta\delta_{\alpha\beta})$$
$$+ \nabla_\gamma\left(\rho u_\alpha u_\beta u_\gamma + \rho\theta\left(u_\alpha\delta_{\beta\gamma} + u_\beta\delta_{\alpha\gamma} + u_\gamma\delta_{\alpha\beta}\right)\right)$$
$$+ F_\gamma\left(-\rho u_\beta\delta_{\alpha\gamma} - \rho u_\alpha\delta_{\beta\gamma}\right)$$
$$- O(\partial^2) \tag{4.57}$$

This statement is identically equal to the Euler equation as stated in equation 4.52, with the inclusion of second order and higher derivatives on the right hand side that will become the Navier-Stokes pressure and viscous stress tensors. All that is required to recover Euler in this expression is to set $\tau = 0$ to mimic the inviscid nature of Euler.

To show full equivalence of equation 4.57 with Navier-Stokes, we aim to replace the time derivative terms on the right hand side above with spatial gradients.

$$\partial_t(\rho u_\alpha u_\beta + \rho\theta\delta_{\alpha\beta}) \rightarrow \nabla_\alpha(something) \tag{4.58}$$

Beginning with the first time derivative, we may carry out a product rule expansion. With a properly grouped product rule expansion, the Euler equation may be rearranged and directly substituted for the first term on the right hand side

$$\partial_t(\rho u_\alpha u_\beta) = \partial_t(\rho u_\alpha)u_\beta + \rho u_\alpha\partial_t(u_\beta)$$
$$= [\rho F_\alpha - \nabla_\gamma\left(\rho u_\alpha u_\gamma + \rho\theta\delta_{\alpha\gamma}\right)]u_\beta + \rho u_\alpha\partial_t(u_\beta) \tag{4.59}$$

To transform the second portion of this time derivative, the Euler equation itself may be massaged into a form to substitute directly for $\rho\partial_t u_\beta$. Beginning by expanding Euler by the product

rule and regrouping terms

$$\partial_t(\rho u_\beta) + \nabla_\gamma(\rho u_\beta u_\gamma + \rho\theta\delta_{\beta\gamma}) - \rho F_\beta = 0$$

$$\partial_t(\rho)u_\beta + \rho\partial_t(u_\beta) + \nabla_\gamma(\rho u_\gamma)u_\beta + \rho u_\gamma\nabla_\gamma(u_\beta) + \nabla_\gamma(\rho\theta\delta_{\beta\gamma}) - \rho F_\beta = 0$$

$$u_\beta[\partial_t\rho + \nabla_\gamma(\rho u_\gamma)] + \rho\partial_t u_\beta + \rho u_\gamma\nabla_\gamma u_\beta + \nabla_\gamma(\rho\theta\delta_{\beta\gamma}) - \rho F_\beta = 0 \qquad (4.60)$$

The term in brackets is equal to zero by the continuity equation (equation 4.49). Rearranging what remains

$$\rho\partial_t u_\beta = \rho F_\beta - \rho u_\gamma\nabla_\gamma u_\beta - \nabla_\gamma(\rho\theta\delta_{\beta\gamma}) \qquad (4.61)$$

This may be substituted directly into equation 4.59 to complete the transformation of the first time derivative into a spatial term

$$\partial_t(\rho u_\alpha u_\beta) = [\rho F_\alpha - \nabla_\gamma(\rho u_\alpha u_\gamma + \rho\theta\delta_{\alpha\gamma})]u_\beta$$
$$+ u_\alpha[\rho F_\beta - \rho u_\gamma\nabla_\gamma u_\beta - \nabla_\gamma(\rho\theta\delta_{\beta\gamma})] \qquad (4.62)$$

The transformation of the second time derivative follows a similar path as that of the first. The derivative is expanded via the product rule, taking care to group terms in a manner that allows - this time - the continuity equation to be used in substitution

$$\partial_t(\rho\theta\delta_{\alpha\beta}) = \partial_t(\rho)\theta\delta_{\alpha\beta} + \rho\partial_t(\theta\delta_{\alpha\beta})$$
$$= -\nabla_\gamma(\rho u_\gamma)\theta\delta_{\alpha\beta} + \rho\partial_t(\theta)\delta_{\alpha\beta} \qquad (4.63)$$

To address the second portion of this time derivative, we refer to the derivation of the macroscopic heat flow equation (which is a consequence of energy conservation $Q = \frac{1}{2}mv^2$) from [55] and use the following substitution

$$\partial_t\theta = -u_\gamma\nabla_\gamma\theta - \frac{2}{3}\theta\nabla_\gamma u_\gamma + O(\partial^2) \qquad (4.64)$$

We note that since our simulations will be constrained to be isothermal, we should properly substitute $\partial_t\theta = 0$ instead. Doing so would affect a slight change in the resulting Navier-Stokes stress

term wherein the term with the coefficient 2/3 would not appear in the final result. We shall not derive the governing equation of heat flow here; however, for the sake of completeness, we will simply press on with the knowledge of energy conservation.

Using substitution from Eq. (4.64, we can cast the second time derivative in spatial terms only

$$
\begin{aligned}
\partial_t(\rho\theta\delta_{\alpha\beta}) = & -\nabla_\gamma(\rho u_\gamma)\theta\delta_{\alpha\beta} \\
& + \rho[-u_\gamma\nabla_\gamma\theta - \frac{2}{3}\theta\nabla_\gamma u_\gamma + O(\partial^2)]\delta_{\alpha\beta}
\end{aligned}
\tag{4.65}
$$

Substituting equations 4.62 and 4.65 back into equation 4.57 to eliminate the time derivatives in favor of spatial gradients on the right hand side, we obtain the following as our equation of motion

$$
\begin{aligned}
\partial_t(\rho u_\alpha) + \nabla_\beta(\rho u_\alpha u_\beta + \rho\theta\delta_{\alpha\beta}) - \rho F_\alpha = & \ \tau\nabla_\beta\{[\rho F_\alpha - \nabla_\gamma(\rho u_\alpha u_\gamma + \rho\theta\delta_{\alpha\gamma})]u_\beta \\
& + u_\alpha[\rho F_\beta - \rho u_\gamma\nabla_\gamma u_\beta - \nabla_\gamma(\rho\theta)\delta_{\beta\gamma}] \\
& - \nabla_\gamma(\rho u_\gamma)\theta\delta_{\alpha\beta} + \rho[-u_\gamma\nabla_\gamma\theta - \frac{2}{3}\theta\nabla_\gamma u_\gamma + O(\partial^2)]\delta_{\alpha\beta} \\
& + \nabla_\gamma(\rho u_\alpha u_\beta u_\gamma + \rho\theta(u_\alpha\delta_{\beta\gamma} + u_\beta\delta_{\alpha\gamma} + u_\gamma\delta_{\alpha\beta})) \\
& + F_\gamma(-\rho u_\beta\delta_{\alpha\gamma} - \rho u_\alpha\delta_{\beta\gamma}) \\
& - O(\partial^2)\}
\end{aligned}
\tag{4.66}
$$

The road to Navier-Stokes next requires a great deal of algebraic simplification of the terms in the braces above. Along the way, several cancellations are possible by expanding terms with either a standard product rule or a "reverse" product rule. Algebraic rearrangement is also used copiously.

$$
\begin{aligned}
\{\ldots\} =\ & [\rho F_\alpha - \nabla_\gamma\left(\rho u_\alpha u_\gamma + \rho\theta\delta_{\alpha\gamma}\right)]u_\beta + u_\alpha[\rho F_\beta - \rho u_\gamma\nabla_\gamma u_\beta - \nabla_\gamma(\rho\theta)\delta_{\beta\gamma}] \\
& - \nabla_\gamma(\rho u_\gamma)\theta\delta_{\alpha\beta} + \rho[-u_\gamma\nabla_\gamma\theta - \frac{2}{3}\theta\nabla_\gamma u_\gamma + O(\partial^2)]\delta_{\alpha\beta} \\
& + \nabla_\gamma[\rho u_\alpha u_\beta u_\gamma + \rho\theta\left(u_\alpha\delta_{\beta\gamma} + u_\beta\delta_{\alpha\gamma} + u_\gamma\delta_{\alpha\beta}\right)] \\
& + F_\gamma\left(-\rho u_\beta\delta_{\alpha\gamma} - \rho u_\alpha\delta_{\beta\gamma}\right) \\
& - O(\partial^2) \\[4pt]
=\ & \rho u_\beta F_\alpha - u_\beta\nabla_\gamma(\rho u_\alpha u_\gamma) - u_\beta\nabla_\gamma(\rho\theta\delta_{\alpha\gamma}) + \rho u_\alpha F_\beta - \rho u_\alpha u_\gamma\nabla_\gamma u_\beta - u_\alpha\nabla_\gamma(\rho\theta)\delta_{\beta\gamma} \\
& - \nabla_\gamma(\rho u_\gamma)\theta\delta_{\alpha\beta} - \rho u_\gamma\nabla_\gamma\theta\delta_{\alpha\beta} - \frac{2}{3}\rho\theta\nabla_\gamma u_\gamma\delta_{\alpha\beta} + O(\partial^2)\rho\delta_{\alpha\beta} \\
& + \nabla_\gamma(\rho u_\alpha u_\beta u_\gamma) + \nabla_\gamma(\rho\theta u_\alpha)\delta_{\beta\gamma} + \nabla_\gamma(\rho\theta u_\beta)\delta_{\alpha\gamma} + \nabla_\gamma(\rho\theta u_\gamma)\delta_{\alpha\beta} \\
& - F_\gamma\rho u_\beta\delta_{\alpha\gamma} - F_\gamma\rho u_\alpha\delta_{\beta\gamma} \\
& - O(\partial^2) \\[4pt]
=\ & \cancel{\rho u_\beta F_\alpha} - u_\beta\nabla_\gamma(\rho u_\alpha u_\gamma) - u_\beta\nabla_\gamma(\rho\theta\delta_{\alpha\gamma}) + \cancel{\rho u_\alpha F_\beta} - \rho u_\alpha u_\gamma\nabla_\gamma u_\beta - u_\alpha\nabla_\gamma(\rho\theta)\delta_{\beta\gamma} \\
& - \nabla_\gamma(\rho u_\gamma)\theta\delta_{\alpha\beta} - \rho u_\gamma\nabla_\gamma\theta\delta_{\alpha\beta} - \frac{2}{3}\rho\theta\nabla_\gamma u_\gamma\delta_{\alpha\beta} + \cancel{O(\partial^2)\rho\delta_{\alpha\beta}} \\
& + \nabla_\gamma(\rho u_\alpha u_\beta u_\gamma) + \nabla_\gamma(\rho\theta u_\alpha)\delta_{\beta\gamma} + \nabla_\gamma(\rho\theta u_\beta)\delta_{\alpha\gamma} + \nabla_\gamma(\rho\theta u_\gamma)\delta_{\alpha\beta} \\
& - \cancel{\rho F_\alpha u_\beta} - \cancel{\rho F_\beta u_\alpha} \\
& - \cancel{O(\partial^2)} \\[4pt]
=\ & \cancel{\nabla_\gamma(\rho u_\alpha u_\beta u_\gamma)} - \cancel{u_\beta\nabla_\gamma(\rho u_\alpha u_\gamma)} - \cancel{\rho u_\alpha u_\gamma\nabla_\gamma u_\beta} \\
& + \cancel{\nabla_\gamma(\rho\theta u_\gamma)\delta_{\alpha\beta}} - \cancel{\nabla_\gamma(\rho u_\gamma)\theta\delta_{\alpha\beta}} - \cancel{\rho u_\gamma\nabla_\gamma\theta\delta_{\alpha\beta}} \\
& + \nabla_\beta(\rho\theta u_\alpha) - u_\alpha\nabla_\beta(\rho\theta) \\
& + \nabla_\alpha(\rho\theta u_\beta) - u_\beta\nabla_\alpha(\rho\theta) \\
& - \frac{2}{3}\rho\theta\nabla_\gamma u_\gamma\delta_{\alpha\beta} \\[4pt]
=\ & \cancel{\nabla_\beta(\rho\theta)u_\alpha} + \rho\theta\nabla_\beta u_\alpha - \cancel{u_\alpha\nabla_\beta(\rho\theta)} \\
& + \cancel{\nabla_\alpha(\rho\theta)u_\beta} + \rho\theta\nabla_\alpha u_\beta - \cancel{u_\beta\nabla_\alpha(\rho\theta)} \\
& - \frac{2}{3}\rho\theta\nabla_\gamma u_\gamma\delta_{\alpha\beta} \\[4pt]
\{\ldots\} =\ & \rho\theta\left(\nabla_\beta u_\alpha + \nabla_\alpha u_\beta - \frac{2}{3}\nabla_\gamma u_\gamma\delta_{\alpha\beta}\right)
\end{aligned}
\tag{4.67}
$$

This may be substituted into equation 4.66 to obtain our first version of the Navier-Stokes momentum equations

$$\partial_t(\rho u_\alpha) + \nabla_\beta(\rho u_\alpha u_\beta + \rho\theta\delta_{\alpha\beta}) - \rho F_\alpha = \tau\nabla_\beta\left\{\rho\theta\left(\nabla_\beta u_\alpha + \nabla_\alpha u_\beta - \frac{2}{3}\nabla_\gamma u_\gamma\delta_{\alpha\beta}\right)\right\} \tag{4.68}$$

Rearranging terms a bit, we obtain the final, more conventional, forms of Navier-Stokes

$$\partial_t(\rho u_\alpha) + \nabla_\beta(\rho u_\alpha u_\beta) = -\nabla_\alpha(\rho\theta) + \rho F_\alpha + \nabla_\beta\left[\tau\rho\theta\left(\nabla_\beta u_\alpha + \nabla_\alpha u_\beta - \frac{2}{3}\nabla_\gamma u_\gamma\delta_{\alpha\beta}\right)\right] \tag{4.69}$$

$$\partial_t(\rho u_\alpha) + \nabla_\beta(\rho u_\alpha u_\beta) = -\nabla_\alpha P_{\alpha\beta} + \nabla_\beta\sigma_{\alpha\beta} \tag{4.70}$$

where the external force term (i.e. a "non-ideal" pressure cast in terms of the difference between ideal and total pressure tensors) and the viscous stress tensor are defined as,

$$F_\alpha = \nabla_\beta(\rho\theta\delta_{\alpha\beta} - P_{\alpha\beta}) \tag{4.71}$$

$$\sigma_{\alpha\beta} = \tau\rho\theta\left(\nabla_\beta u_\alpha + \nabla_\alpha u_\beta - \frac{2}{3}\nabla_\gamma u_\gamma\delta_{\alpha\beta}\right) \tag{4.72}$$

Our definition of the viscous stress tensor allows us to identify the definition of dynamic viscosity

$$\eta = \tau\rho\theta \tag{4.73}$$

We use this definition and map Eqs. (4.69) and (4.70) to more traditional expressions of the Navier-Stokes momentum equations. Using vector instead of tensor notation, we have

$$\partial_t(\rho\vec{u}) + \nabla(\rho\vec{u}\vec{u}) = -\nabla(\rho\theta) + \rho\vec{F} + \nabla\left[\eta(\nabla\vec{u} + (\nabla\vec{u})^T) - \nu\nabla\cdot\vec{u}\mathbb{1}\right] \tag{4.74}$$

$$\partial_t(\rho\vec{u}) + \nabla(\rho\vec{u}\vec{u}) = -\nabla P + \nabla\sigma \tag{4.75}$$

4.1.5. The Intuition of Particle Collisions

Before proceeding to develop the lattice Boltzmann equation, we pause for a moment to better connect kinteic theory concepts to intuition. These intuitive connections will be informal in nature, but references such as [50] contain more formal descriptions which lead to these conclusions.

In the kinetic theory development of the Navier-Stokes momentum equations, the collision term Ω_f in Eq. (4.12) directly gives rise to the phenomenon of viscosity. This is seen more clearly in our use of the BGK approximation of Eq. (4.13) and the term τ which appears in our dynamic viscosity definition in Eq. (4.73). As τ decreases in value, Eq. (4.13) implies that the number of collisions increases and Eq. (4.73) implies that viscosity decreases. Connecting these results, viscosity decreases as the number of collisions increase, and the particle "flow" from the non-equilibrium distribution f to the equilibrium distribution f^0 occurs faster.

It is important to realize that an underlying assumption in kinetic theory is that it applies to sufficiently dilute gases. At its core, viscosity in a vapor is synonymous with momentum transfer. More particle collisions shortens the mean free path, which results in slower particles. Slower particles impart less momentum during a collision, hence the lower viscosity. In a liquid, particles are constantly colliding, so there is no meaningful definition of a mean free path. As a consequence, thinking about concepts such as viscosity can lead to counter-intuitive consequences, especially when one understands viscosity intuitively in liquids.

For example, when the temperature of a liquid is increased, the well-known result is that its viscosity decreases (think of oil in an engine). However, Eq. (4.73) when understood in the vapor viscosity context implies that as the temperature of a vapor increases, so does its viscosity. This difference is because liquid viscosity is a consequence of inter-particle interactions, which is a fundamentally different definition than that for vapor viscosity.

One final interesting consequence of a higher number of particle collisions is that entropy production decreases. This is counter-intuitive if one envisions that more collisions equate to more "disorder" in the system. However, when one recalls that more collisions result in a shorter mean free path, we can begin to understand that the particles in a vapor actually explore less volume as they relax to equilibrium. Since entropy is proportional to lnV, a smaller volume directly implies less entropy.

4.2. Lattice Boltzmann Equation

For the discretized version of the BTE, we transition from the continuous to the discrete by dividing our simulation volume into lattice sites of dimension Δx (note that x is of general dimensionality at this point). We also define a set of discrete velocities $\{v_i\}$ such that $x + v_i \Delta t$ is again a lattice location. For each lattice location we then have a density f_i associated to each

velocity v_i. Applying the discretization to Eq. (4.14) and rearranging to isolate the same-timestep terms, we have

$$f_i(x + v_i\Delta t, t + \Delta t) = f_i(x, t) - F_i(x, t) + \frac{1}{\tau}\left[f_i^0(n, \theta) - f_i(x, t)\right] \tag{4.76}$$

This is the lattice Boltzmann equation. This algorithm is usually broken apart into two steps that constantly iterate: streaming and collision.

The streaming step is conceptualized as the transport of particles from one time step to the next $(t \rightarrow t + \Delta t)$. The direction and speed of particle transport is defined by the set of velocity vectors v_i. Streaming is captured by the first two terms in Eq. (4.76).

Within a single time step, particle densities are rearranged according to two main physical causes: non-ideal interparticle interactions (e.g. the attractive part of a potential) and momentum exchange due to particle collision. In principle, the collision operator can be any defined process Ω, but here we implement the BGK approximation identically from the continuous to the discrete. The collision operation accounts for the conserved momentum exchanges as the particles relax towards equilibrium. A generalized force term F_i includes the non-ideal behavior as well as the non-conservative effects of friction (we specify this explicitly in Section 5.2).

We finally note that the force term of the continuous equation - which is specified by $F_\alpha d_{v_\alpha} f$ - is generalized into the single term $F_i(x, t)$ of the discrete equation. This generalization is necessary since the velocities are now part of a discrete set v_i and we can no longer take a velocity derivative ∂_{v_α} of the distribution function. We note that in Section 4.1.2, the continuous form the force F_α and the velocity derivative $\partial_{v_\alpha} f$ are separable, which obviated the need to specify moments of the force term. In this case they are not, so to ensure equivalence, we demand that the velocity moments of this new general term F_i are equal to the moments of the continuous force term as follows

$$\int F_\alpha \partial_{v_\alpha} f dv = \sum_i F_i = 0 \tag{4.77}$$

$$\int F_\beta \partial_{v_\beta} f v_\alpha dv = \sum_i F_i v_{i\alpha} = -nF_\alpha \tag{4.78}$$

$$\int F_\gamma \partial_{v_\gamma} f v_\alpha v_\beta dv = \sum_i F_i v_{i\alpha} v_{i\beta} = -n(F_\alpha u_\beta + F_\beta u_\alpha) \tag{4.79}$$

The continuous force moments are directly calculable and are simplified by use of the distribution function moments from Section 4.1.1. This has been partially done in the derivation of the master moment equation in Section 4.1.4.1.

4.2.1. Discrete Equations of Motion

At this stage, the discrete BTE is not able to be simulated since we do not know the form of the non-equilibrium particle distributions f_i. However, we are able to "rewrite" the equation into a form that depends only on the local equilibrium distribution f^0, which we do know (the Maxwell-Boltzman distribution).

To begin, we cast the left hand side of equation 4.76 to the same time step as the right hand side, a Taylor expansion is used. A derivative operator - the material derivative - is defined such that $D_i \equiv (\partial_t + v_{i\alpha}\nabla_\alpha)$ (or with another appropriate Greek subscript), and the time steps Δt are constrained to be integer steps of 1 [43]

$$f_i(x + v_i\Delta t, t + \Delta t) = \sum_k \frac{(\Delta t)^k}{k!} D_i^k f_i(x, t)$$

$$f_i(x + v_i, t + 1) = f_i(x, t) + D_i f_i(x, t) + \frac{1}{2} D_i^2 f_i(x, t) + O(\partial^3) \tag{4.80}$$

Note that further space, time, and energies are implied. This expansion may be substituted back into equation 4.76, obtaining to second order:

$$\cancel{f_i} + D_i f_i + \frac{1}{2} D_i^2 f_i + O(\partial^3) = \cancel{f_i} - F_i + \frac{1}{\tau}\left[f_i^0 - f_i\right]$$

$$D_i f_i + \frac{1}{2} D_i^2 f_i + F_i = \frac{1}{\tau}\left[f_i^0 - f_i\right] \tag{4.81}$$

Equation 4.81 may be rearranged to $f_i = f_i^0 - \tau\left(D_i f_i + \frac{1}{2} D_i^2 f_i + F_i\right)$, which is iteratively substituted into itself to cast things in terms of the known equilibrium distribution f_i^0. Again, to second order:

$$D_i \left[f_i^0 - \tau \left(D_i f_i + \frac{1}{2} D_i^2 f_i + F_i \right) \right] + \frac{1}{2} D_i^2 \left[f_i^0 - \tau \left(D_i f_i + \frac{1}{2} D_i^2 f_i + F_i \right) \right] + F_i = \frac{1}{\tau} \left[f_i^0 - f_i \right]$$

$$D_i f_i^0 - \tau D_i^2 f_i - \tau \underset{O(\partial^3)}{\cancel{\frac{1}{2} D_i^3 f_i}} - \tau D_i F_i + \frac{1}{2} D_i^2 f_i^0 - \underset{O(\partial^3)}{\cancel{\frac{1}{2} \tau D_i^3 f_i}} - \underset{O(\partial^4)}{\cancel{\tau \frac{1}{4} D_i^4 f_i}} - \underset{O(\partial^3)}{\cancel{\frac{1}{2} D_i^2 \tau F_i}} + F_i = \frac{1}{\tau} \left[f_i^0 - f_i \right]$$

$$D_i f_i^0 - \tau D_i^2 \underset{O(\partial^{3+})}{\cancel{\left[f_i^0 - \tau \left(D_i f_i + \frac{1}{2} D_i^2 f_i + F_i \right) \right]}} - \tau D_i F_i + \frac{1}{2} D_i^2 f_i^0 + F_i = \frac{1}{\tau} \left[f_i^0 - f_i \right]$$

$$D_i f_i^0 - \tau D_i^2 f_i^0 - \tau D_i F_i + \frac{1}{2} D_i^2 f_i^0 + F_i = \frac{1}{\tau} \left[f_i^0 - f_i \right]$$

$$D_i (f_i^0 - \tau F_i) - \left(\tau - \frac{1}{2} \right) D_i^2 f_i^0 + F_i = \frac{1}{\tau} \left[f_i^0 - f_i \right] \tag{4.82}$$

Eq. (4.82) is the discrete Boltzmann Transport Equation that our model will simulate for a given equilibrium distribution f^0. Note that the constant τ has been effectively "renormalized" to $(\tau - \frac{1}{2})$ when compared to the continuous BTE (Eq. 4.14). We can rearrange Eq. (4.82) to cast the unknown distribution function f purely in terms of the known quantity f^0. But although f^0 is known in principle, we still must specify its form.

If we can choose a discrete f^0 that adheres to the same moments as those for the continuous Maxwell-Boltzmann distribution in Section 4.1.3.1, we can be sure that our discretization will also recover the hydrodynamic equations of motion in Section 4.1.4. Our solution is to discretize the Maxwell-Boltzmann distribution itself.

4.2.2. Discrete Maxwell-Boltzmann Distribution

As a reminder, the continuous Maxwell-Boltzmann distribution we use is given by Eq. (4.28)

$$f_i^0 = \frac{n}{(2\pi\theta)^{\frac{3}{2}}} \mathrm{e}^{-\frac{(v_{i\alpha} - u_\alpha)^2}{2\theta}}$$

where, like in the discrete BTE, the i subscript denotes dependence on a discrete velocity vector; the position dependency is implied. We must discretize this distribution in order to use this as our local equilibrium distribution in a discrete model.

Our discretization starts by expanding the peculiar velocity term in the exponential

$$f_i^0 = n \underbrace{(2\pi\theta)^{-\frac{3}{2}} \mathrm{e}^{-\frac{v_{i\alpha}^2}{2\theta}}}_{w_i} \mathrm{e}^{\frac{(2v_{i\alpha}u_\alpha - u^2)}{2\theta}} \tag{4.83}$$

where we have also rearranged the result to emphasize the identification of a velocity-dependent weight factor, w_i. The weights form a set that map one-to-one to the velocities, and they must meet additional constraints that are outlined below.

Proceeding with the expansion, the remaining exponential in terms of the average velocity u_α can be further expanded into a power series. In general, the power series expansion for an exponential is

$$e^x = 1 + x + \frac{x^2}{2!} + \frac{x^3}{3!} + \cdots \tag{4.84}$$

Identifying the exponent as x, we can convert the exponential into the following power series which keeps terms up to the second order

$$
\begin{aligned}
\mathrm{e}^{\frac{(2v_{i\alpha}u_\alpha - u^2)}{2\theta}} &= 1 + \left(\frac{v_{i\alpha}u_\alpha}{\theta} - \frac{u^2}{2\theta}\right) + \frac{1}{2}\left(\frac{v_{i\alpha}u_\alpha}{\theta} - \frac{u^2}{2\theta}\right)^2 + O(\partial^3) \\
&= 1 + \frac{v_{i\alpha}u_\alpha}{\theta} + \frac{(v_{i\alpha}u_\alpha)^2}{2\theta^2} - \frac{u^2}{2\theta} + O(\partial^3)
\end{aligned}
\tag{4.85}
$$

Replacing the exponential with the power series to second order, our discretized local equilibrium distribution is

$$f_i^0 = nw_i\left[1 + \frac{v_{i\alpha}u_\alpha}{\theta} + \frac{(v_{i\alpha}u_\alpha)^2}{2\theta^2} - \frac{u^2}{2\theta}\right] \tag{4.86}$$

We need to ensure that the use of the discrete version of our equilibrium distribution will still lead to recovery of the desired conservation equations [57]. As such, we demand that all

continuous and discrete moments - up to the order of interest - match

$$\sum_i f_i^0 = n \tag{4.87}$$

$$\sum_i f_i^0 v_{i\alpha} = n u_\alpha \tag{4.88}$$

$$\sum_i f_i^0 v_{i\alpha} v_{i\beta} = n u_\alpha u_\beta + n\theta \delta_{\alpha\beta} \tag{4.89}$$

$$\sum_i f_i^0 v_{i\alpha} v_{i\beta} v_{i\gamma} = n u_\alpha u_\beta u_\gamma + n\theta(u_\alpha \delta_{\beta\gamma} + u_\beta \delta_{\alpha\gamma} + u_\gamma \delta_{\alpha\beta}) \tag{4.90}$$

Enforcing these moments is equivalent to discretizing our weight factors w_i appropriately and generating "moments" of the weights. We determine the first three such moments by substituting Eq. (4.86) into Eq. (4.87)

$$\begin{aligned}
n &= \sum_i n w_i \left[1 + \frac{v_{i\alpha} u_\alpha}{\theta} + \frac{(v_{i\alpha} u_\alpha)^2}{2\theta^2} - \frac{u^2}{2\theta} \right] \\
&= n \left[\sum_i w_i + \frac{u_\alpha}{\theta} \sum_i w_i v_{i\alpha} + \frac{u_\alpha^2}{2\theta^2} \sum_i w_i v_{i\alpha}^2 - \frac{u^2}{2\theta} \sum_i w_i \right]
\end{aligned} \tag{4.91}$$

This equality will hold if the term in brackets is equal to 1, and since w_i is a discrete version of a continuous normalization factor, it must sum to 1. These facts drive the definition of the other two sums inside the brackets, which collectively define the first three moments of our weights

$$\sum_i w_i = 1 \tag{4.92}$$

$$\sum_i w_i v_{i\alpha} = 0 \tag{4.93}$$

$$\sum_i w_i v_{i\alpha} v_{i\beta} = \theta \delta_{\alpha\beta} \tag{4.94}$$

71

Repeating this procedure with the next two equilibrium distribution moments in Eqs. (4.88) and (4.89) allows us to identify the next two moments of the weights as

$$\sum_i w_i v_{i\alpha} v_{i\beta} v_{i\gamma} = 0 \tag{4.95}$$

$$\sum_i w_i v_{i\alpha} v_{i\beta} v_{i\gamma} v_{i\delta} = \theta^2 (\delta_{\alpha\beta}\delta_{\gamma\delta} + \delta_{\alpha\gamma}\delta_{\beta\delta} + \delta_{\alpha\delta}\delta_{\beta\gamma}) \tag{4.96}$$

The final weight moment deserves a little extra attention. One may sense the pattern developing that the even moments are equal to sequential powers of θ (appropriately tensor-ized) and the odd moments are equal to zero to preserve the isotropic nature of our simulation. This logic can be used to correctly guess that the next moment is

$$\sum_i w_i v_{i\alpha} v_{i\beta} v_{i\gamma} v_{i\delta} v_{i\epsilon} = 0 \tag{4.97}$$

However, when one substitutes Eq. (4.86) into Eq. (4.90) and uses this definition, we find that the third discrete moment of the equilibrium distribution is not correctly recovered

$$\sum_i f_i^0 v_{i\alpha} v_{i\beta} v_{i\gamma} = n\theta(u_\alpha \delta_{\beta\gamma} + u_\beta \delta_{\alpha\gamma} + u_\gamma \delta_{\alpha\beta}) \neq n u_\alpha u_\beta u_\gamma + n\theta(u_\alpha \delta_{\beta\gamma} + u_\beta \delta_{\alpha\gamma} + u_\gamma \delta_{\alpha\beta}) \tag{4.98}$$

For simulations where the average velocity u_α is sufficiently small, the term $n u_\alpha u_\beta u_\gamma$ can be neglected to rectify this situation. This is fine for the most common LB applications; however, in cases where the magnitude of u_α proves to be large enough, violations of Galilean invariance may result. This is the discrete manifestation of the same problem with the continuous third moment in Eq. (4.39).

The moments of our discrete weights act as constraints to the values the weights can take. We shall apply these constraints in Section 5.1 to derive the weights of the D1Q3 model we use in this thesis. We will also be able to use these relations to constrain the value of our isothermal lattice temperature θ.

4.2.3. Discrete Multicomponent Conservation Equations

Now that we have specified the form of the equilibrium distribution f^0, we can show that our discrete model recovers the standard continuity and Navier-Stokes equations. We also introduce the

multicomponent notation from Section 2.1.2 to the LB theory here. The discrete theory discussed up to this point is strictly for a single component; however, we choose to implement the simplest extension to multiple components by simply replicating the necessary equations for each component c in our mixture.

We note at this point that when we replicate the average velocity of a fluid u_α to create u_α^c, this new component-specific velocity is not itself a proper hydrodynamic variable. Nevertheless, they are still useful as we use them to define the hydrodynamic mean fluid velocity u_α by weighting the "velocities" of each component u_α^c by its respective composition ρ^c/ρ.

We start our multicomponent extension by assigning each component c in our model its own discrete LB representation, which is identical in form to the single-component representation from Eq. (4.76)

$$f_i^c(x + v_i, t + 1) - f_i^c(x, t) + F_i^c(x, t) = \frac{1}{\tau} \left[f_i^{c0}(n, \theta) - f_i^c(x, t) \right] \tag{4.99}$$

The first thing to note is that by keeping the form of the lattice Boltzmann equation for a specific component c identical to that of a regular single-component lattice Boltzmann equation, we are easily able to sum up the LB equations over all components ($\sum_c Eq.4.99$) to recover a single LB equation for the entire mixture. The full-mixture equation also has the single-component form and is identical to Eq. (4.76).

Given our chosen equilibrium distribution and its moments, we automatically know that the full mixture equations of motion are the standard continuity equation

$$\partial_t \rho + \nabla_\alpha (\rho \hat{u}_\alpha) = 0 \tag{4.100}$$

where the mean velocity of the fluid is found to be

$$\hat{u}_\alpha = u_\alpha + \frac{1}{2\rho} F_\alpha \tag{4.101}$$

This redefinition of the mean velocity arises from discretizing the force and can be thought of as an average of the pre-/post-force velocities [49].

73

In terms of the new mean velocity $\hat{u}_\alpha$, the Navier-Stokes equations

$$\partial_t(\rho\hat{u}_\alpha) + \nabla_\beta(\rho\hat{u}_\alpha\hat{u}_\beta) = -\nabla_\alpha(\rho\theta) + \rho F_\alpha + \nabla_\beta\left[\tau\rho\theta\left(\nabla_\beta\hat{u}_\alpha + \nabla_\alpha\hat{u}_\beta - \frac{2}{3}\nabla_\gamma\hat{u}_\gamma\delta_{\alpha\beta}\right)\right] \quad (4.102)$$

Eqs. (4.100) and (4.102) govern the motion of the mixture as a whole. However, we must still derive the equations of motion with respect to a single component. In a manner similar to how Eq. (4.82) was obtained from Eq. (4.81), we perform a Taylor expansion of the first term in Eq. (4.99) and algebraically rearrange Eq. (4.99) to iteratively substitute it into itself to obtain an expression for f_i^c in terms of the equilibrium distribution f_i^{c0}

$$\partial_t f_i^{c0} + v_{i\alpha}\nabla_\alpha f_i^{c0} - \tau\partial_t F_i - v_{i\alpha}\nabla_\alpha F_i + F_i - (\tau - \frac{1}{2})(\partial_t + v_{i\alpha}\nabla_\alpha)_i^2 f_i^{c0} + O(\partial^3) = \frac{1}{\tau}(f_i^{c0} - f_i^c) \quad (4.103)$$

Summing over the indices i and using the previous definition of $\hat{u}_\alpha^c$ gives

$$\partial_t\rho^c + \nabla_\alpha(\rho^c\hat{u}_\alpha^c) = O(\partial^2) \quad (4.104)$$

Since $\hat{u}_\alpha^c$ is a function of the non-hydrodynamic component velocity u_α^c, we wish to eliminate u_α^c in favor of the mixture's mean velocity u_α, which is a hydrodynamic variable. Defining the component velocity as a deviation from the mean fluid velocity

$$u_\alpha^c = \hat{u}_\alpha + \delta u_\alpha^c \quad (4.105)$$

we obtain the component-specific zeroth moment as

$$\partial_t\rho^c + \nabla_\alpha\left(\rho^c u_\alpha^c\right) = -\nabla_\alpha(\rho^c\delta u_\alpha^c) + O(\partial^2) \quad (4.106)$$

This leaves us with the task of identifying δu_α^c in terms of the hydrodynamic quantities. We begin by determining the first velocity moment of Eq. (4.103) and keeping only first-order terms

$$\partial_t(\rho^c u_\alpha^c) + \nabla_\alpha(\rho^c u_\alpha^c u_\beta^c + \rho^c\theta\delta_{\alpha\beta}) + F_\alpha^c = O(\partial^2) \quad (4.107)$$

Substituting in the component velocity defined in Eq. (4.105) and noting that derivatives of the small perturbation δu_α^c are negligible, we have

$$\partial_t(\rho^c \hat{u}_\alpha) + \nabla_\alpha(\rho^c \hat{u}_\alpha \hat{u}_\beta) + \nabla_\beta(\rho^c \theta) + F_\alpha^c = O(\partial^2) \tag{4.108}$$

Multiplying Eq. (4.102) by $\frac{\rho^c}{\rho}$, recognizing that $-\nabla_\alpha P_{\alpha\beta} = -\nabla_\alpha(\rho\theta) + F_\alpha$, and absorbing second-order terms into $O(\partial^2)$ allows a substitution for the first 2 terms

$$-\frac{\rho^c}{\rho}\nabla_\alpha P_{\alpha\beta} + \nabla_\beta(\rho^c \theta) + F_\alpha^c = O(\partial^2) \tag{4.109}$$

Finally, we substitute in the Gibbs-Duhem relation (Eq. 2.29) and the force definitions from Eqs. (5.24) and (5.22) to obtain

$$-\frac{\rho^c}{\rho}\sum_{c'}\rho^{c'}\nabla_\beta\mu^{c'} + \nabla_\beta(\rho^c\theta) + \rho^c\nabla_\alpha(\mu^c - \mu^{c,id}) - \sum_{c'}\lambda^{cc'}\frac{\rho^c\rho^{c'}}{\rho^c + \rho^{c'}}(\hat{u}_\alpha^{c'} - \hat{u}_\alpha^c) = O(\partial^2) \tag{4.110}$$

Using $\theta\rho^c\nabla\log(\rho^c) = \theta\nabla\rho^c$, the second term above is recognized as an ideal chemical potential gradient (for an isothermal system), which cancels with part of the non-ideal chemical potential driving force. Given the definition of the full density ρ, we can simplify the expression as

$$\sum_{c'}\frac{\rho^c\rho^{c'}}{\rho}\nabla_\alpha(\mu^c - \mu^{c'}) - \sum_{c'}\lambda^{cc'}\frac{\rho^c\rho^{c'}}{\rho}(\hat{u}_\alpha^{c'} - \hat{u}_\alpha^c) = O(\partial^2) \tag{4.111}$$

Expanding this equation and and substituting in the Gibbs-Duhem relation allows us to rewrite as

$$-\nabla_\alpha\mu^c = \sum_{c'}\lambda^{cc'}\frac{\rho^{c'}}{\rho}(\hat{u}_\alpha^c - \hat{u}_\alpha^{c'}) - \frac{1}{\rho}\nabla_\beta P_{\alpha\beta} + O(\partial^2) \tag{4.112}$$

This linear system of equations is the definition of Maxwell-Stefan diffusion with the addition of a barodiffusion term $\nabla_\beta P_{\alpha\beta}$ that captures an average pressure gradient force acting on each component. Provided the pressure tensor is non-singular, one may use the hydrodynamic substitution for u_α^c (Eq. 4.105), and in principle, Eq. (4.112) will always yield a general solution for δu_α^c.

In the specific case of symmetric, constant $\lambda^{cc'} = \lambda$ and a divergence-free pressure tensor - such as for a two-component simulation - this reduces to general Fickian diffusion where

$$\delta u^c = -\frac{1}{\lambda}\nabla_\alpha\mu^c + O(\partial^2)$$

(4.113)

and the term $1/\lambda$ is identified as the component mobility.

5. LATTICE BOLTZMANN D1Q3 IMPLEMENTATION

Traditionally, LB models are described at a high level by two characteristics: dimensionality and the number of discrete velocities. The notation DXQY describes a lattice that is represented in X spatial dimensions with Y number of velocities used to describe motion along the lattice.

Now that sufficient theoretical background has been established, we shall describe the actual implementation of the D1Q3 lattice Boltzmann model used for this thesis. One of the strong points of a LB implementation is its simplicity, and as a reflection of that simplicity, this section will be relatively brief. We will begin with an overview of how to arrive at the expressions for the distribution function f that are actually coded. We then refer to prior work that was used to help ensure our model acts in a thermodynamically consistent and stable manner. We then define the physical basis for the non-ideal forcing mechanism and the friction among components. We then conclude with specifics related to the van der Waals fluid and interface constants pertinent to our implementation.

A brief note on the expressions in this chapter. A great many of the expressions that follow can be simplified algebraically, which would sometimes lead to a slight increase in code performance. A design decision was made to generally forego such simplifications in the interest of being able to more easily connect the theory to an explicit code implementation. Where applicable, the expressions that follow were coded verbatim to coincide with the arbitrary point in a derivation where the author's intuition was satisfied.

5.1. D1Q3 Model

Regardless of the dimensionality and discretization that is desired, the concrete implementation of a LB model can begin with a simple rearrangement of Eq. (4.99)

$$\underbrace{f_i^c(x + v_i, t + 1) - f_i^c(x, t)}_{f_i^c(t+1)+=} = \frac{1}{\tau} \left[f_i^{c0}(n, \theta) - f_i^c(x, t) \right] - F_i^c(x, t) \tag{5.1}$$

where we redefine the left-hand side of the equation as a standard "plus-equals" operation which modifies the particle distribution from one time step to the next. This is the streaming part of our LB algorithm. Also note that we have isolated the collision side of our LB algorithm to the

right-hand side of the equation. Our collisions are captured by the BGK approximation and the generalized force term F_i^c referenced in the last section.

The D1Q3 model uses three discrete velocities to generate one "copy" of Eq. (5.1) per velocity vector per component c. The three velocity vectors in our model $v_i \in \{-1, 0, +1\}$ means that we will have a set of three particle distribution functions $\{f_{-1}^c, f_0^c, f_{+1}^c\}$ for each component c, three equilibrium distribution functions $\{f_{-1}^{c0}, f_0^{c0}, f_{+1}^{c0}\}$ for each component c, and three discrete weights $\{w_{-1}, w_0, w_{+1}\}$ (which are component-agnostic).

Each equilibrium distribution f_i^{c0} carries a weight w_i that corresponds to the velocity v_i. From Section 4.2.2, the weights in Eqs. (4.92), (4.94), and (4.96) expand to

$$w_0 + w_{+1} + w_{-1} = 1 \tag{5.2}$$

$$w_{+1} + w_{-1} = \theta \tag{5.3}$$

$$w_{+1} + w_{-1} = 3\theta^2 \tag{5.4}$$

The two equations in θ can be solved to identify the isothermal temperature of our lattice

$$\theta = \frac{1}{3} \tag{5.5}$$

This temperature value can be used to solve the system for each weight

$$w_0 = \frac{2}{3} \qquad w_{+1} = w_{-1} = \frac{1}{6} \tag{5.6}$$

We know that the last two weights are equal by Eq. (4.93).

We further specify the model by explicitly refining the discrete equilibrium distribution from Eq. (4.86). Substituting in the magnitude of each velocity vector along with its corresponding weight and reducing, we find

$$f_0^{c0} = n^c - n^c u^{c2} - n^c \theta \tag{5.7}$$

$$f_{+1}^{c0} = \frac{1}{2}(n^c u^{c2} + n^c u^c + n^c \theta) \tag{5.8}$$

$$f_{-1}^{c0} = \frac{1}{2}(n^c u^{c2} - n^c u^c + n^c \theta) \tag{5.9}$$

This result may be a little more readily obtained by expanding the moments of the discrete equilibrium distribution in Eqs. (4.87), (4.88), and (4.89) and solving the resulting system of equations.

Finally, we need to expand the constraints on the generalized force term F_i^c given by Eqs. (4.77), (4.78), and (4.79) to derive the implementation for each velocity vector. Before we do, we make two modifications. Eq. (4.78) is modified to

$$\sum_i F_i^c v_i = -F^c \tag{5.10}$$

which is an expression of the force per particle that is consistent with our discretization.

As shown in [22] the lattice Boltzmann model to this point will contain thermodynamic inconsistencies. To help ensure consistent thermodynamics, we add a correction term Ψ^c to Eq. (4.79), and we also express this moment per particle

$$\sum_i F_i^c v_i^2 = -2F^c u^c + \Psi^c \tag{5.11}$$

Note that we drop the Greek indices since we are explicitly using a one-dimensional model. References [22] and [58] demonstrate that a fourth-order analysis of forcing methods leads to the following choice for the general correction term $\Psi_{\alpha\beta}^c$ to ensure consistent thermodynamic equilibrium

$$\Psi_{\alpha\beta}^c = -\frac{1}{\tau}\left[(\tau - \frac{1}{4})\frac{F_\alpha^c F_\beta^c}{\rho^c} + \frac{1}{12}\nabla^2 \rho^c\right] \tag{5.12}$$

Expanding the force moments and solving the resulting system gives the force associated with each velocity vector

$$F_0^c = 2F^c u^c - \Psi^c \tag{5.13}$$

$$F_{+1}^c = -F^c u^c - \frac{1}{2}F^c + \frac{1}{2}\Psi^c \tag{5.14}$$

$$F_{-1}^c = -F^c u^c + \frac{1}{2}F^c + \frac{1}{2}\Psi^c \tag{5.15}$$

It is an interesting note that the force associated with the rest velocity is identical to the second velocity moment of the force.

After assembling the pieces into the form suggested by Eq. (5.1), the lattice Boltzmann equations for each component and velocity at a given lattice site were explicitly coded as

$$f_0^c(t+1) \mathrel{+}= \frac{1}{\tau}\left[(n^c - n^c\theta - n^c u^{c2}) - f_0^c(t)\right] - (2F^c u^c - \Psi^c) \tag{5.16}$$

$$f_{+1}^c(t+1) \mathrel{+}= \frac{1}{\tau}\left[\frac{1}{2}(n^c u^{c2} + n^c u^c + n^c\theta) - f_{+1}^c(t)\right] - \left(-F^c u^c - \frac{1}{2}F^c + \frac{1}{2}\Psi^c\right) \tag{5.17}$$

$$f_{-1}^c(t+1) \mathrel{+}= \frac{1}{\tau}\left[\frac{1}{2}(n^c u^{c2} - n^c u^c + n^c\theta) - f_{-1}^c(t)\right] - \left(-F^c u^c + \frac{1}{2}F^c + \frac{1}{2}\Psi^c\right) \tag{5.18}$$

These equations form the core of the LB model.

5.2. External Forcing Term

Our model still requires an explicit force. In the absence of an external potential, a single-component LB model will generally simulate an ideal gas, with an equation of state $P = \rho\theta$. The macroscopic force that is in play for such a model is usually the gradient of the pressure ∇P.

In a multicomponent model, we need to identify such a thermodynamic force that acts on each component of the mixture separately. If one simulates a mixture of ideal fluids, the pressure P can be split into partial pressures P^c, the weighted sum of which comprises the full pressure of the mixture

$$\sum_c \frac{\rho^c}{\rho} P^c = P \tag{5.19}$$

We are not simulating ideal fluids. Every component of our mixtures is a van der Waals fluid, and the inter-particle interaction renders the explicit partial pressure approach null. Instead, we can implicitly implement the same concept by leveraging the Gibbs-Duhem relation from Eq. (2.29) as defined for multiple components

$$\nabla_\beta P_{\alpha\beta} = \sum_c \rho^c \nabla_\alpha \mu^c \tag{5.20}$$

which reminds us that each component c has its own chemical potential.

Leveraging Gibbs-Duhem, we define the force F_α^c to have two contributions which combine such that $F_\alpha^c = F_\alpha^{\mu,c} + F_\alpha^{f,c}$: thermodynamic forcing from chemical potential gradients ($F_\alpha^{\mu,c}$) and momentum exchanges from friction between mixture components ($F_\alpha^{f,c}$).

5.2.1. Thermodynamic Forcing

Our thermodynamic, conservative force is provided not by a pressure gradient but by the gradient of the non-ideal part of the chemical potential

$$F_\alpha^{\mu,c} = \rho^c \nabla_\alpha (\mu^c - \mu^{c,id}) \tag{5.21}$$

where $\mu^{c,id} = \theta ln \rho^c$ is the ideal portion of the chemical potential for component c and the form of the right-hand side is implied by the Gibbs-Duhem relation.

Interestingly, coding Eq. (5.22) is not straightforward as there are two possible implementations:

1. Directly substituting the definition of the ideal chemical potential into Eq. (5.22)

$$F_\alpha^{\mu,c} = \rho^c \nabla_\alpha (\mu^c - \theta ln \rho^c) \tag{5.22}$$

This method is termed the "nid" method.

2. Simplifying the expression by applying the gradient operation to both terms in the previous option

$$F_\alpha^{\mu,c} = \rho^c \nabla_\alpha \mu^c - \theta \nabla_\alpha \rho^c \tag{5.23}$$

This method is termed the "log" method.

Both are expressions implement the non-ideal chemical potential driving force in Eq. (5.21); however, the numeric representations of each yield results that differ in both accuracy and stability. The results of both implementations are reviewed in Figure 6.6a.

5.2.2. Friction between Components

The friction between the components of a mixture is a non-conservative, dissipative force. The form of this force can be found from first-principle mechanics by enforcing momentum and kinetic energy conservation between two colliding particles. The frictional force by an arbitrary second component c' on a primary component c is proportional to the velocity difference between

the two components

$$F_\alpha^{f,c} = -\sum_{c' \neq c} \lambda^{cc'} \frac{\rho^c \rho^{c'}}{\rho^c + \rho^{c'}} (\hat{u}_\alpha^{c'} - \hat{u}_\alpha^c) \tag{5.24}$$

where $\lambda^{cc'}$ is a parameterized friction coefficient between the two components and the $\hat{u}_\alpha^c$ are true fluid velocities, defined through Eq. (4.101). The total frictional force on component c is summed up over all other types of components in the mixture. The minus sign sets the convention that friction acts opposite to any driving forces defined in a positive direction.

5.3. Model Stability

To aid the accuracy and help control the stability of the lattice Boltzmann simulations in the regions where we anticipated phase separation with sizeable density ratios, we implemented two things. First, lattice Boltzmann simulations were initialized with $tanh$ density profiles with bulk values equal to the results of our free energy minimization. And second, we sought to initialize the density profiles with an interface width, w, that was close to the equilibrium interface width.

The initial interface width we imposed drove the choice of two simulation parameters: $\kappa^{cc'}$ and a chemical potential coefficient γ_μ. The numerical parameter γ_μ is an artificial construct used to control the abruptness with which the chemical potential-based forcing $F^{\mu,c}$ is applied. More explicitly stated, in the implementation, $F^{\mu,c}$ is coded as $\gamma_\mu F^{\mu,c}$ ($F^{\mu,c} \equiv \gamma_\mu F^{\mu,c}$). Reference [24] specifies the minimum width in lattice spaces that a phase interface should take

$$w_{min} = \frac{1}{\sqrt{4\rho_v(\theta_c - \theta)}} \tag{5.25}$$

where ρ_v is the expected density of the vapor phase, θ_c is the critical temperature for a component and θ is the isothermal lattice temperature. It also defines the relationship of the parameters $\kappa^{cc'}$ and γ_μ to the interface width as

$$w(\kappa, \theta/\theta_c) = \sqrt{\frac{2\kappa^{cc'}}{\frac{\theta_c}{\theta} - 1}} \tag{5.26}$$

We can equate these two expressions to obtain an expression for $\kappa^{cc'}$

$$\kappa^{cc'} = \frac{1}{8\rho_v \theta} \tag{5.27}$$

where ρ_l is the expected liquid density determined by minimizing the free energy. Once $\kappa^{cc'}$ is obtained, a bound on the lattice speed of sound can be leveraged to determine γ_μ

$$c_s = \sqrt{1 - 4\kappa^{cc'}\rho_l\gamma_\mu} \tag{5.28}$$

where c_s is the lattice speed of sound (equal to $\frac{1}{\sqrt{3}}$).

The interface width and values for $\kappa^{cc'}$ and γ_μ obtained from this method provided an automatic starting point for the constraints on any simulation. However, it is a bit imprecise as the speed of sound constraint in Eq. (5.28) is strictly an inequality, not an equality. When a simulation is encountered that exhibits instability because of this, it is usually simple to manually adjust these parameters a small amount from their automatic starting value to stabilize a simulation. But in practice, this method proved to be very reliable and useful for automating a series of simulations.

5.4. Discrete Derivative Stencils

A good deal of the thermodynamic theory derived in Chapter 2 hinges on our ability to leverage the Gibbs-Duhem relation from Eq. (2.29). However, the transition from continuous to discrete thermodynamics necessarily involves an approximation to the gradient - and by extension the laplacian - operation. The approximated gradient operator ∇^D means the discrete implementation of the Gibbs-Duhem is no longer strictly equal [22]

$$\nabla^D_\beta P_{\alpha\beta} \approx \sum_c \rho^c \nabla^D_\alpha \mu^c \tag{5.29}$$

This problem can be exacerbated by choosing the wrong stencil for the problem at hand from the several choices available [59]. We can alleviate this concern by using the generalized lattice interaction parameter $\phi^{cc'}(\Delta x)$ in the defintion of our discrete free energy from Eq. (2.69) to inform our choice of stencil.

We have seen in Eqs. (2.73) and (2.74) that the VDW constant $a^{cc'}$ and the interfacial energy term $\kappa^{cc'}$ can be thought of as discrete sums involving a generalized lattice interaction parameter $\phi^{cc'}(\Delta x)$. Given our D1Q3 velocity set v_i, we can expand those moments to express the

lattice interaction parameters $\phi^{cc'}(\Delta x)$ in terms of $a^{cc'}$ and $\kappa^{cc'}$

$$a^{cc'} = -\phi^{cc'}(+1) - \phi^{cc'}(0) - \phi^{cc'}(-1) \tag{5.30}$$

$$\kappa^{cc'} = -(+1)^2\phi^{cc'}(+1) - (0)^2\phi^{cc'}(0) - (-1)^2\phi^{cc'}(-1)$$

$$= -\phi^{cc'}(+1) - \phi^{cc'}(-1) \tag{5.31}$$

Assuming isotropy where $\phi^{cc'}(+1) = \phi^{cc'}(-1)$ and solving this system, we find

$$\phi^{cc'}(0) = \kappa^{cc'} - a^{cc'} \tag{5.32}$$

$$\phi^{cc'}(+1) = \phi^{cc'}(-1) = -\frac{1}{2}\kappa \tag{5.33}$$

We can substitute these definitions into an expansion of the lattice interaction term from Eq. (2.69) to deduce an appropriate stencil

$$\sum_{c'}\sum_{\Delta x}\phi^{cc'}(\Delta x)\rho^c(x)\rho^{c'}(x + \Delta x)$$

$$= \sum_{c'}\left[\phi^{cc'}(0)\rho^c(x)\rho^{c'}(x+0) + \phi^{cc'}(+1)\rho^c(x)\rho^{c'}(x+1) + \phi^{cc'}(-1)\rho^c(x)\rho^{c'}(x-1)\right]$$

$$= \sum_{c'}\left[(\kappa^{cc'} - a^{cc'})\rho^c(x)\rho^{c'}(x) - \frac{1}{2}\kappa\rho^c(x)\rho^{c'}(x+1) - \frac{1}{2}\kappa\rho^c(x)\rho^{c'}(x-1)\right]$$

$$= \sum_{c'}\left\{-a^{cc'}\rho^c(x)\rho^{c'}(x) - \frac{1}{2}\kappa\rho^c(x)\left[\underbrace{\rho^{c'}(x+1) - 2\rho^{c'}(x) + \rho^{c'}(x-1)}_{\nabla^2\rho^{c'}(x)}\right]\right\} \tag{5.34}$$

The term in brackets is recognized as a central difference Laplacian operator, which is accurate to $O(\partial^2)$ and implies that the companion gradient operator should also be of the central difference variety (where boundary conditions allow).

Although in the particular case of the D1Q3 discretization these discrete derivatives likely correspond to our intuition, this has both removed all guess work and formally specified the accuracy of our approximation - and implicitly the accuracy of the discrete Gibbs-Duhem relation. In higher-dimension discretizations where several discrete derivative choices exist, the solution may not be as intuitive.

6.   LATTICE BOLTZMANN SIMULATIONS

6.1. Verification for Mixtures of van der Waals Fluids

In this main section we will examine the ability of our lattice Boltzmann method to recover the complex phase behavior of mixtures of van der Waals fluids. The first, quite extensive, section regards two-component mixtures. We examine the key types of phase diagrams obtainable for such mixtures. A smaller second part shows a single example of a three-component van der Waals fluid, showing four phase coexistence.

6.1.1. Single van der Waals Fluid

The first order of business for developing our LB method was to implement a single-component model, implement the 4th-order corrections from [22] to ensure consistent thermodynamics, and replicate the results of [24] to a practical standard of stability. We used a lattice of size 201 for our D1Q3 model and iterated each test point 250,000 iterations to ensure equilibrium was achieved. Figure 6.1 shows that the implementation is both stable and thermodynamically consistent to a rather low ratio of lattice temperature to critical temperature.
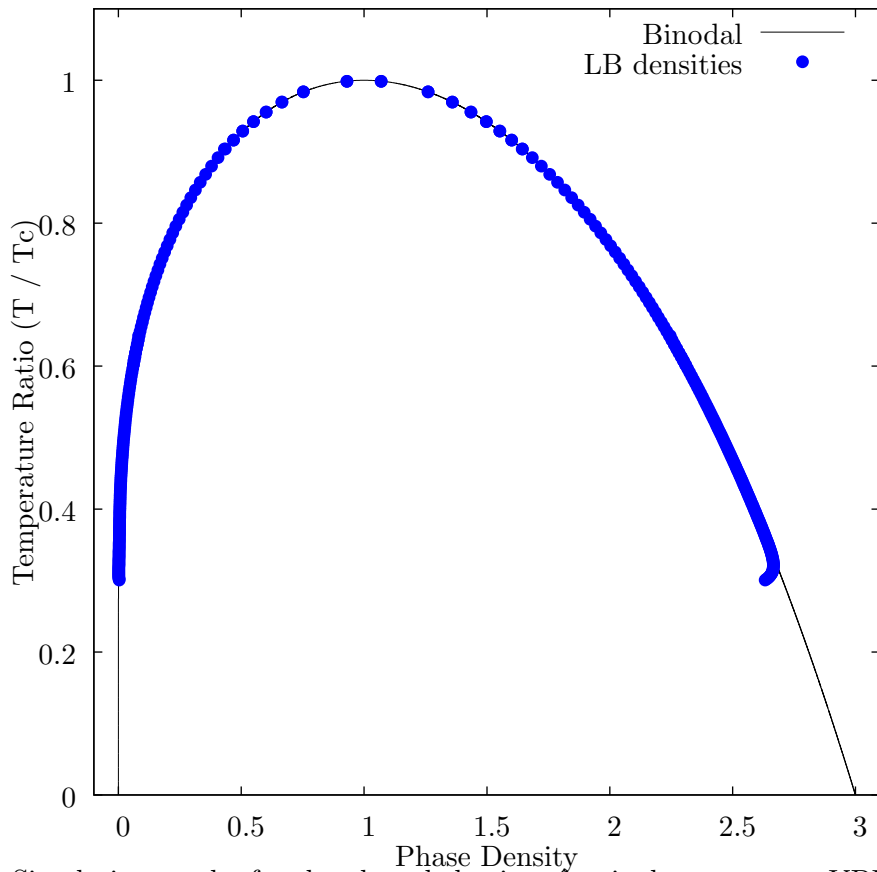
Figure 6.1. Simulation results for the phase behavior of a single-component VDW fluid. The error in the vapor density is $\sim 10^{-4}$ at a temperature ratio of about 0.44; the density ratio at this point is 277. The error in the liquid density is $\sim 10^{-4}$ at a temperature ratio of about 0.36, and the density ratio at this point is 707. The maximum density ratio is near 1400, but we have observed density ratios of over 2500 with proper tuning of the parameters κ and γ_μ. The finite size of the lattice begins to seriously impose an effect on the phase interface around a density ratio of 0.32.

The stabilizing mechanisms from Section 5.3 were explicitly implemented to automatically determine our simulation parameters and generate Figure 6.1. This method was able to generate nearly all of our data points; however, in our first example of the implementations imprecision, a small segment of the phase diagram as not stable. The solution was to simply reduce the size of γ_μ by a factor of 10, and the remainder of the diagram was filled in very well.

6.1.2. Two van der Waals Fluids

With the thermodynamic consistency of a single-component baseline established, we extended the LB model to simulate a binary VDW mixture. To illustrate the thermodynamic consistency of our LB method in a multicomponent case, we use Figure 6.2 as a representative case.

Figure 6.2 shows the density profile along with the associated pressure and chemical potentials that the LB simulation recovers for the A,B pair (0.8, 0.8), which is in the middle of the three-phase region in Figure 6.6. The constant chemical potentials across the lattice and constant pressure in the bulk phases confirm that the simulation has recovered a thermodynamically valid equilibrium profile. The simulated bulk pressure converges to a constant value across the lattice to better than 10^{-11}, and it matches theoretical expectations to approximately 10^{-6}. There are much larger discrepancies at the interfaces which we attribute to the use of a chemical potential-based forcing method rather than a pressure gradient-based method popular with single-component models.
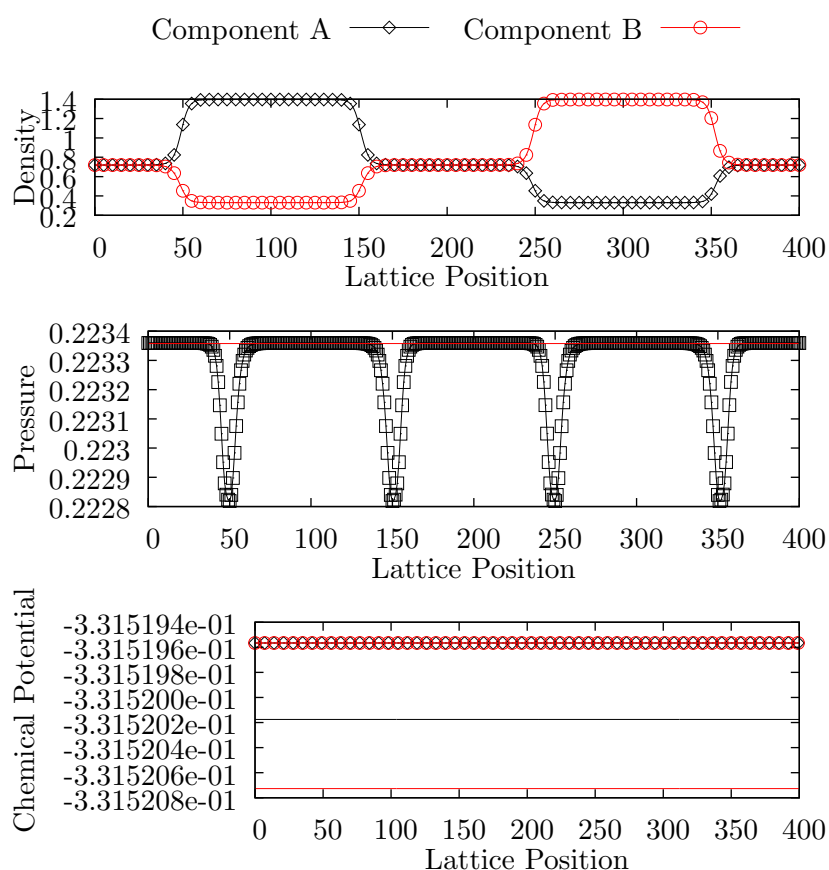
Figure 6.2. Simulation results from our baseline phase diagram (see Figure 6.6) for the initial A,B pair (0.8, 0.8), which exhibits thermodynamically consistent 3-phase equilibrium. The component key applies to the density profile and chemical potential diagrams; solid lines are theoretical expectations for the pressure and chemical potentials. The bulk pressure across phases is constant to 10^{-11}. The chemical potentials for each component were equal to 10^{-9} after only 50,000 iterations and better than 10^{-12} after 1,000,000 iterations. Pressure and chemical potentials matched theoretical expectations to 10^{-6}.

The simulated chemical potentials for both components are constant across the entire lattice - interfaces included - to better than 10^{-12}, and the values also both match theoretical expectations to approximately 10^{-6}. Finally, we note that both the pressure and chemical potentials exhibited significant digital noise ($\sim 10^{-6}$ in amplitude) at the start of all simulations; however, they both converge to near-machine accuracy constant values if the simulations are allowed sufficient time to run.

The LB simulations were initialized with a range of (ρ^A, ρ^B) density pairs in a near-equilibrium profile and allowed to iterate for 50,000 time steps. We selected up to 35 density pairs to test in regions of the theoretical phase diagram that were anticipated to exhibit 2-phase behavior (see Figure 6.3); anticipated 3-phase regions were exhaustively tested. The densities associated with the resulting phases were logged when each simulation concluded. Simulations covered a range of critical temperature, critical density, and interaction parameters to test a variety of phase diagram structures.
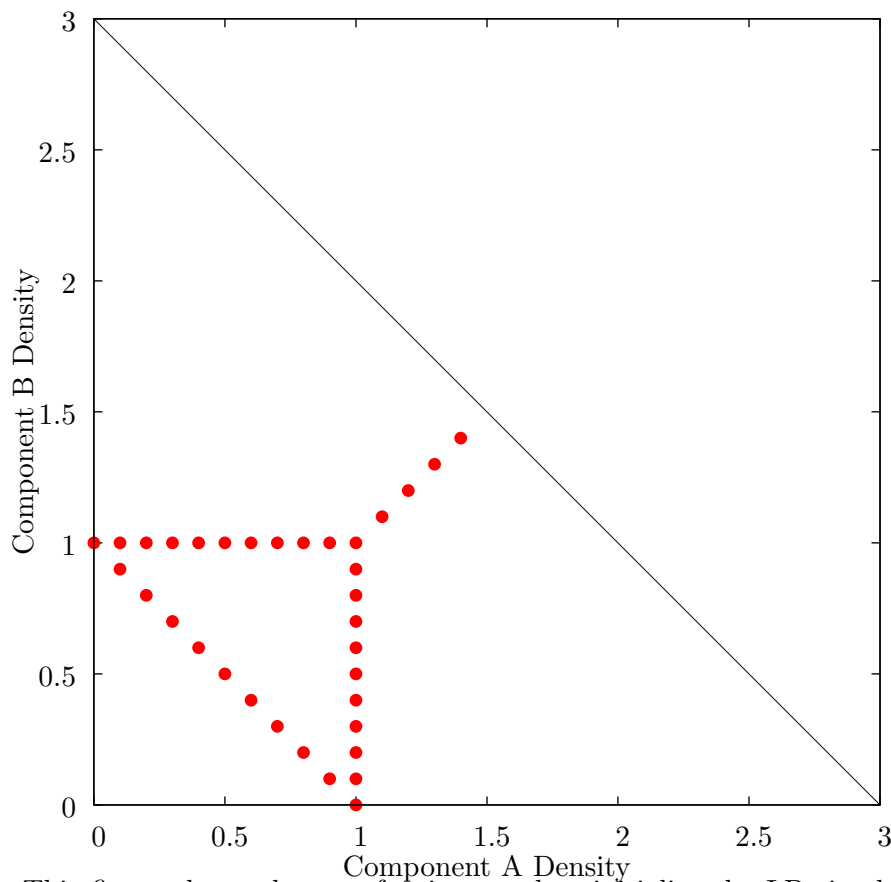
Figure 6.3. This figure shows the set of points used to initialize the LB simulations to test the two-phase regions of our phase diagrams. The algorithm moves vertically from the A-component axis, horizontally from the B-component axis, diagonally from axis to axis, and diagonally from (1.0,1.0) to (1.4,1.4). The point (1.5,1.5) is also tested if a mixture components are asymmetric enough to admit it.

The lattice Boltzmann simulations that tested each phase diagram were automated to consistently and comprehensively test all two- and three-phase regions. To cover the two-phase regions, we selected "paths" through the phase diagrams that were general enough to ensure at least one lattice Boltzmann simulation would occur in all of the anticipated regions: vertical from the A-component axis (1,0) to (1,1), horizontal from the B-component axis (0,1) to (1,1), diagonal from axis-to-axis (1,0) to (0,1), and diagonal from (1,1) to near the van der Waals singularity line at (1.4, 1.4). These path are shown in Figure 6.3. Note that occasionally the asymmetry of the components in a mixture will also include the point (1.5, 1.5).

In general, we chose $\kappa^{cc'} = 0.1$ for our LB simulations. The major exception to this is in simulating the 2-phase behavior in the binary liquid regions of a phase diagram, where we allowed

$\kappa^{cc'}$ to linearly increase from 0.15 at (1.0,1.0) to 0.5 at (1.4,1.4). Deviations from these values are noted in the captions of the associated phase diagrams.

To increase the stability of our LB simulations, all simulations began by estimating the width of the equilibrium interface for a specified value for $\kappa^{cc'}$. This estimate is given for the single-component theory outlined in [24] as

$$w_{min} = \frac{1}{\sqrt{4\rho_v|\theta_c - \theta|}} \tag{6.1}$$

We slightly modified Eq. (6.1) to allow phase diagrams with components to be warmer than their respective critical temperatures. This initial width proved to overestimate the equilibrium interface width in most cases. To improve the initial interface width, this initial estimate was iterated to a near-equilibrium state (usually 50,000 time steps) where the interface width was numerically measured. The measured interface width was used to re-initialize the simulation, and a coefficient was calculated to preserve the relationship $w \propto \sqrt{\kappa^{cc'}}$. The value of γ_μ was initialized according to the relation in Eq. (5.28). When a simulation was unstable ($\sim 5\%$ of the total simulations), γ_μ was numerically optimized to find the maximum value that would provide a stable simulation. If this automation failed to find a stable simulation, parameters were manually tuned by either decreasing the initial value of γ_μ by a factor of anywhere from 2-10 or setting the initial interface width to 2 lattice spaces. This occurred 13 times in $\sim$160 simulations in the two-phase regions, and not at all in $\sim$5600 simulations in the three-phase regions.

The subsections that follow outline our LB simulation results for the phase diagrams indicated in Figure 3.6. Results are grouped in three ways: symmetric components (solid symbols in Figure 3.6), asymmetric components (open symbols in Figure 3.6), and the so-called "shield" region (enclosed region around $\zeta = 0, \Lambda = 0.4364$ in Figure 3.6). Several LB simulations touched areas of numerical instability, but the automated parameter tuning performed exceptionally and lattice Boltzmann simulations were still able to reproduce all binodals very well.

6.1.2.1. Symmetric Components

The first test case was for that of a mixture of two identical components, i.e. a de-facto single-component simulation, with $\theta_c^A = \theta_c^B = 0.4$, $\rho_c^B = 1.0$, and a neutral interaction parameter $\nu = 1.0$. Figure 6.4 shows the phase diagram recovered by minimizing the free energy of such a

system along with the associated lattice Boltzmann simulations. As we expected for a de-facto single-component simulation, we obtained a perfectly symmetrical diagram with straight binodal lines connecting equal densities on the A- and B-component axes. The values of the phase-separated densities on each axis corresponded to the results of a single-component simulation given the same initial conditions.
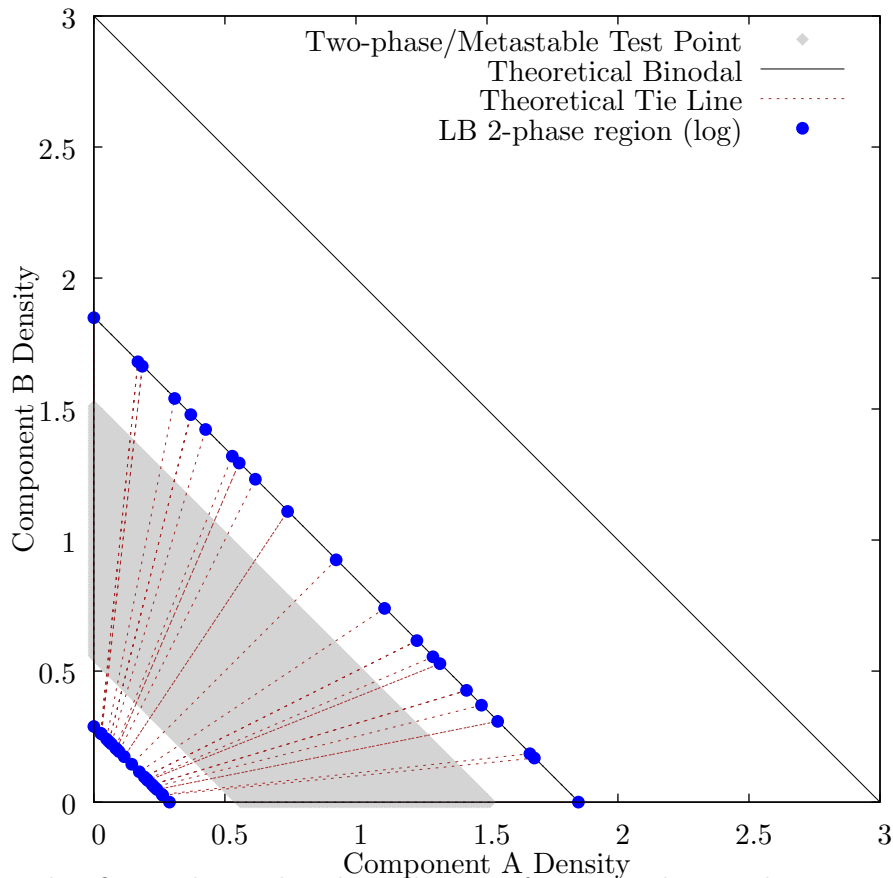
Figure 6.4. This figure shows the phase diagram for a van der Waals mixture of two identical components, which borders Types I and II in the center of Figure 3.6. It was generated using parameters of $\theta_c^A = \theta_c^B = 0.4$, $\rho_c^B = 1.0$, and a neutral interaction parameter $\nu = 1.0$ ($\xi = 0.0, \zeta = 0.0, \Lambda = 0.0$). Overlaid on top of the theoretical diagram generated by free energy minimization are the results of the LB simulations. Also depicted is a diagonal connecting the van der Waals equation discontinuities for both components.

Proceeding from the neutral interaction case in Figure 6.4, we induced repulsive behavior between the two components by reducing the interaction parameter ν. First we notice that the liquid-gas phase separation now depends on the relative concentration of the A and B components.

More mixed fluids show a gas density that is increased whereas the liquid density at coexistence is decreased. For high density liquids we see a further miscibilty gap appear for a liquid-liquid phase separation where the two VDW fluids behave as a binary liquid. Figure 6.5 shows this behavior with $\nu = 0.7$. We see that this predicted behavior is well recovered by the lattice Boltzmann simulations.
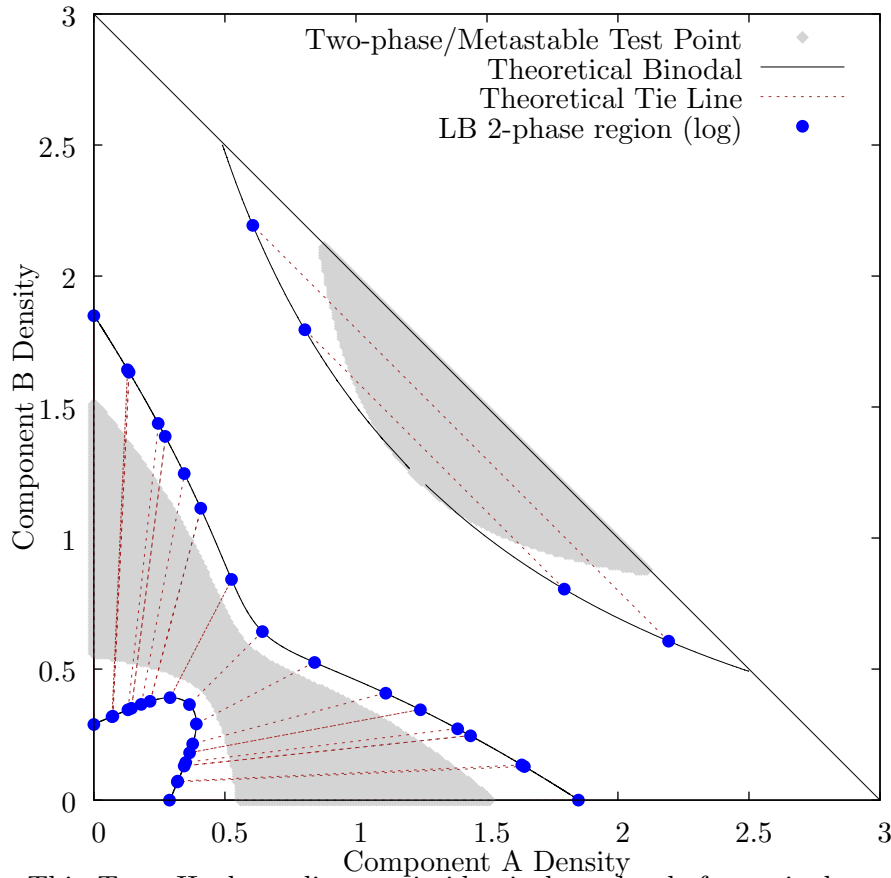
Figure 6.5. This Type II phase diagram is identical to the de-facto single component mixture except phase separation was induced by setting $\nu = 0.7$ ($\xi = 0.0, \zeta = 0.0, \Lambda = 0.3$). The interaction parameter is not quite repulsive enough to connect all regions of phase separation or provoke 3-phase behavior.

Increasing the repulsion between the components further by setting $\nu = 0.5$ the liquid-liquid phase separation becomes more severe, and the binodals from the "bubble" of binary liquid behavior intersect the liquid-gas coesistence curves as shown in Figure 6.6. The binodal lines that define the vapor densities for the two liquid-vapor regions also intersect. These three binodal intersections
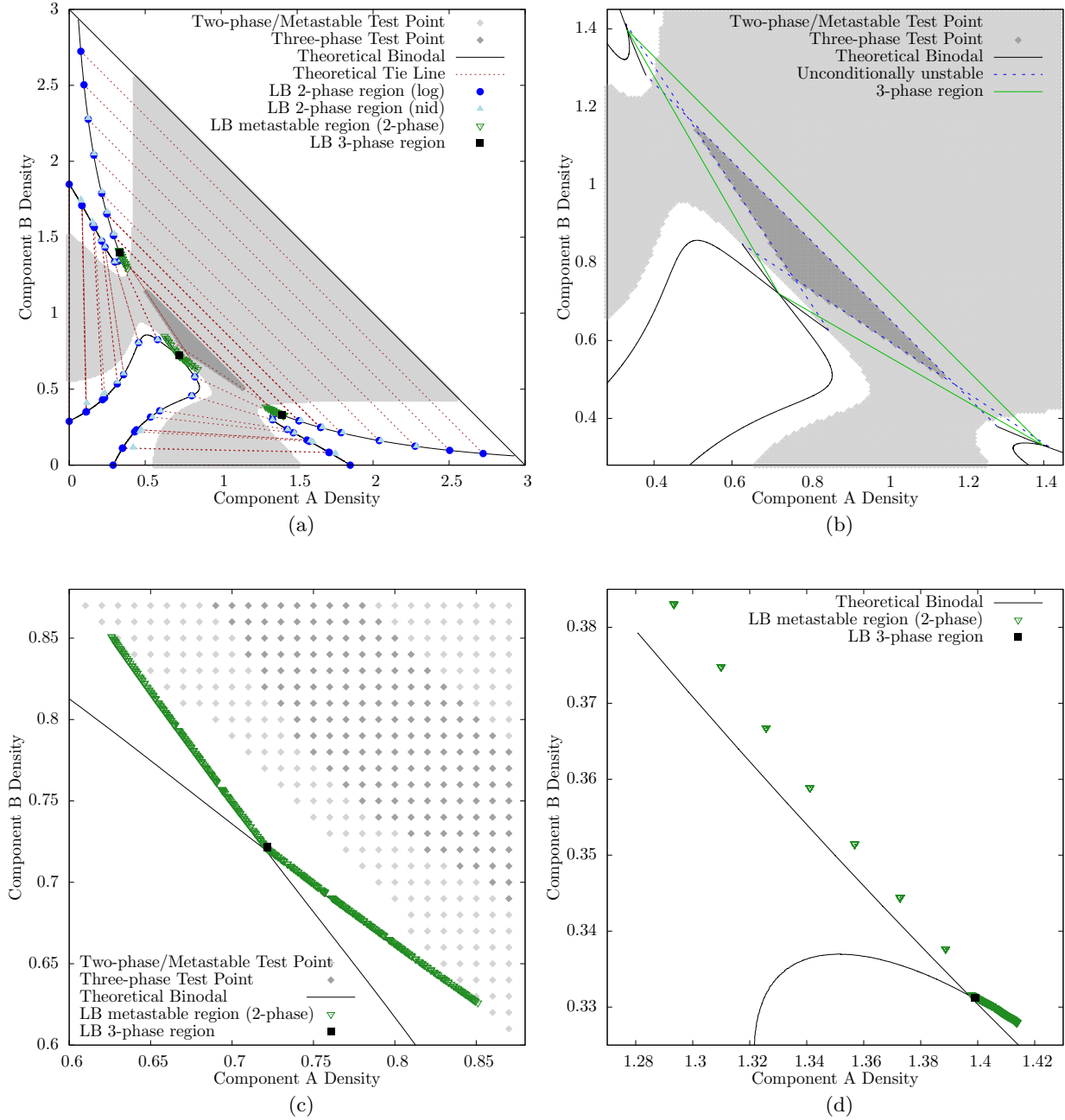
Figure 6.6. A baseline case of 3-phase behavior in a Type III phase diagram. Part (a) shows a phase diagram for a mixture identical to the component in Figure 6.4 except $\nu = 0.5$ ($\xi = 0.0, \zeta = 0.0, \Lambda = 0.5$). Part (b) zooms in to show the three binodal intersections that define the full three-phase region, and the connections between binodals that are used to inscribe the unconditionally unstable 3-phase region can also be seen. In (c) we see the crossing binodals in the vapor region of the 3-phase behavior. Finally, part (d) shows the crossing binodals in the A-rich liquid region of the 3-phase behavior; those in the B-rich liquid region are similar. The LB simulations of metastable points follow the binodals well, but they show the same small deviation from the binodal intersection point as noted in (c).

now define a new region in the phase diagram that exhibits either metastable behavior or 3-phase behavior.

The minimization algorithm predicts 3-phase behavior for every point in this region, and the behavior was reflected in all LB simulations in this region. The LB simulations of metastable points follow the binodals well after the crossing point. The LB simulations for three-phase points show a very small deviation from the point of intersection of the binodals due to interface effects present in the LB simulations that were not incorporated into the bulk free energy minimization.

We exhaustively tested every density pair in the full three-phase region with LB simulations, and as seen in Figure 6.6a the LB simulations recover both the metastable behavior and 3-phase behavior within the three-phase region quite well. In particular, every simulation within the unconditionally unstable three-phase region (see Figure 6.6b) exhibited 3-phase behavior. Metastable points that were initialized with three phases held the 3-phase behavior as well as points in the unconditionally unstable three-phase region. Metastable points that were initialized with two phases also held the 2-phase behavior very well and followed the theoretical binodals after the points of intersection. However, we note that all 2-phase metastable LB simulations show inaccuracies that are attributed to interfacial effects, which are out of scope of this paper.

We used the baseline mixture in Figure 6.6 to perform a comparison between two forcing methods based on chemical potential gradients. This comparison was performed only in the two-phase regions of the phase diagram. We found that the non-ideal chemical potential forcing method (Eq. 5.22) was greatly outperformed - both in terms of accuracy and stability - by the "log" method of Eq. (5.23). Given this, we based all subsequent simulations on only the method of Eq. (5.23).

Figure 6.7 is an example of a symmetric mixture where the lattice temperature is below the common critical temperature of the two components. However, this is the first example we show of a mixture where both components severely repel each other. The repulsion in this case is enough to not only create a standard binary liquid region but to also induce 3-phase behavior. Moreover, there are two very small regions of liquid-vapor phase separation that are an outgrowth of the three-phase region. These small regions are the "accessory plaits" in the terminology of Korteweg [3].
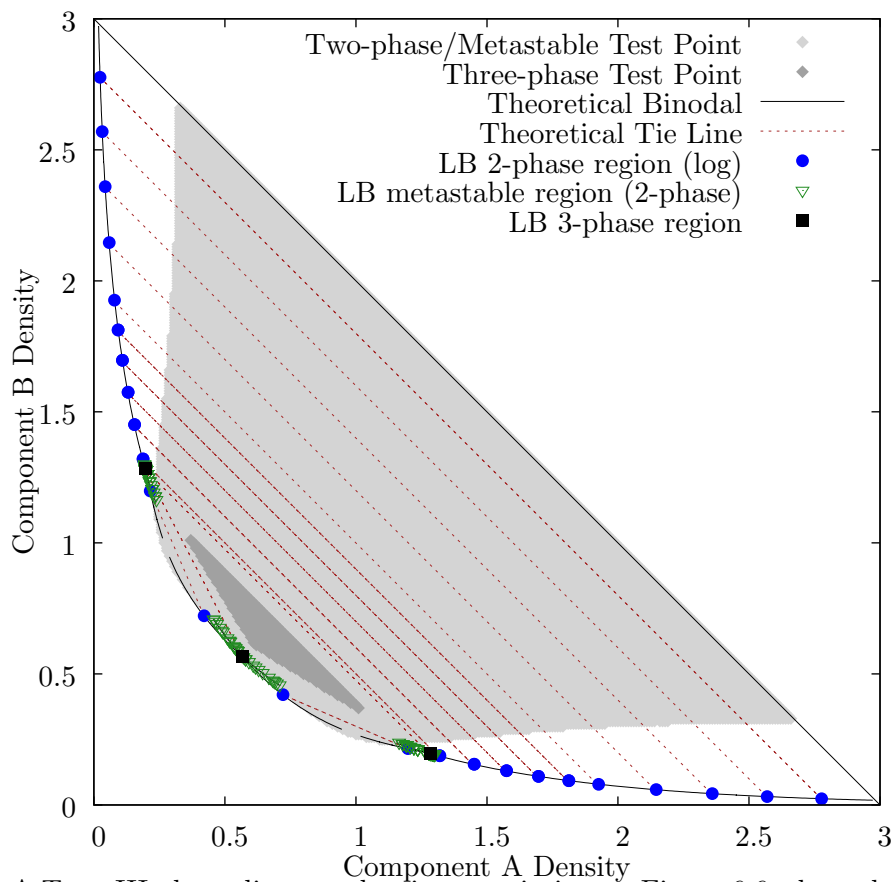
Figure 6.7. A Type III phase diagram showing a variation on Figure 6.6 where the lattice temperature is above the critical temperatures of each component, but the interaction parameter is repulsive enough to still elicit three-phase behavior. It was generated using parameters of $\theta_c^A = \theta_c^B = 0.32$, $\rho_c^B = 1.0$, and $\nu = 0.2$ ($\xi = 0.0, \zeta = 0.0, \Lambda = 0.8$). The maximum density ratio is almost 105.

6.1.2.2. Asymmetric Components

Figure 6.8 is our first example of a phase diagram for a mixture of two components with asymmetric critical traits. The A- and B-components are asymmetrical in both their critical temperatures and critical densities, but there is no interaction between them. The overall appearance of this phase diagram is unremarkably similar to that of a single-component VDW fluid with the exception that the spinodal region is markedly skewed towards the B-component axis. The LB simulations recovered the theoretical expectations well overall; however, the accuracy of the vapor density results fell off by an order of magnitude ($\sim 10^{-3}$ error) at the higher density ratios.

Figure 6.8. A Type II phase diagram showing a lattice temperature that is in between the critical temperatures of the two components $(\theta_c^B < \theta < \theta_c^A)$ and asymmetric critical densities $(\rho_c^A < \rho_c^B)$; the interaction parameter is neutral. It was generated using parameters of $\theta_c^A = 0.5$, $\theta_c^B = 0.3$, $\rho_c^B = 1.2$, and $\nu = 1.0$ ($\xi = 0.090909, \zeta = 0.162791, \Lambda = 0.013339$). Six test points defaulted to values for $\kappa^{cc'}$ derived from single-component theory; the values were all between 3.6 and (slightly above) 3.7.

Figure 6.9 is another mixture of components that are asymmetric in both critical temperatures and densities, In this case, the lattice temperature is slightly below the critical temperatures of each component, and the cross-component interaction is moderately repulsive. The net result is three separate domains with large miscibility gaps separating them: a liquid-vapor region rich in A-component, a liquid-vapor region rich in B-component, and a binary liquid region. This particular example is a good approximation to if the mixture in Figure 6.5 was warmed up (save the slight asymmetry).
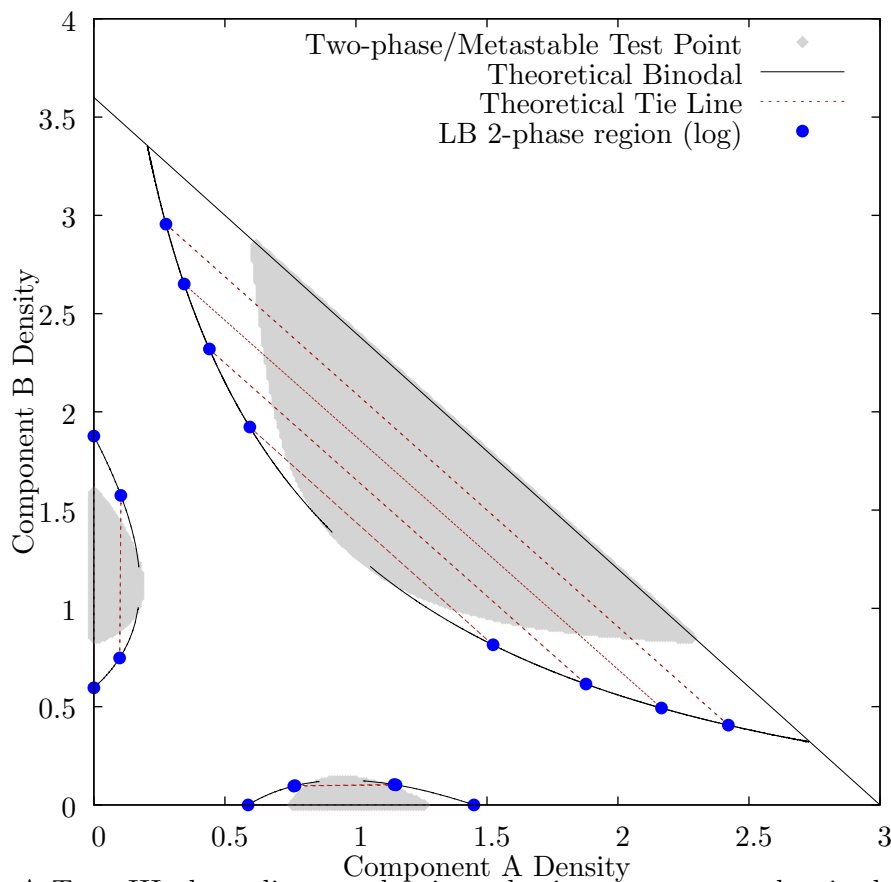
Figure 6.9. A Type III phase diagram showing a lattice temperature that is close enough to the critical temperatures of each component that there are three distinct regions of phase separation; the interaction parameter is repulsive. It was generated using parameters of $\theta_c^A = 0.35$, $\theta_c^B = 0.36$, $\rho_c^B = 1.2$, and $\nu = 0.6$ ($\xi = -0.090909$, $\zeta = 0.104859$, $\Lambda = 0.403308$).

Figure 6.10 illustrates the behavior when asymmetric components that have a moderate affinity for each other are mixed. The lattice temperature is again below the critical temperatures of both components, which has the effect of detaching the spinodal region from the pure component axes and creating a "bubble" of 2-phase behavior.
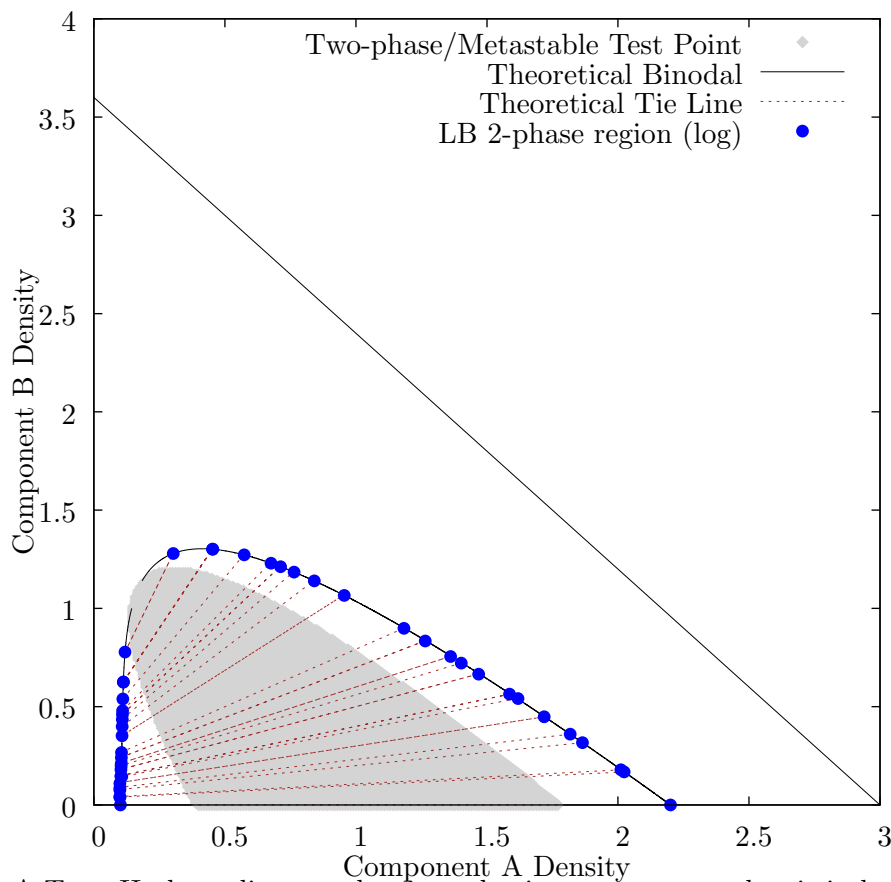
Figure 6.10. A Type I phase diagram showing a lattice temperature that is above the asymmetric critical temperatures of the two components ($\theta_c^A < \theta_c^B < \theta$) and asymmetric critical densities ($\rho_c^A < \rho_c^B$); however, the interaction parameter is attractive enough to still produce two-phase behavior. It was generated using parameters of $\theta_c^A = 0.3$, $\theta_c^B = 0.31$, $\rho_c^B = 1.3$, and $\nu = 1.5$ ($\xi = -0.130435, \zeta = 0.146515, \Lambda = -0.483813$).

In Figure 6.11, we see perhaps our most interesting phase diagram with effects arising due to the asymmetry of the components. Relative to our very symmetric, well-behaved baseline case in Figure 6.6, only two parameter adjustments were made: the critical temperature of the B-component was raised to 0.45 (from 0.40) and the critical density of the B-component was raised to 1.1 (from 1.0). All other parameters are unchanged. At first look, it appears that the binodal from the B-vapor simply rides up and over an independent A-liquid-vapor region to join the A-binary liquid binodal. However, when zooming in to the peak of the A-liquid-vapor region, we see the situation is far more complicated. The binodals cross again to define two points of the three-phase region, and a miscibility gap has appeared in the middle of the three-phase region. This gap has the effect of dividing part of the metastable points into two new accessory plaits: one region at
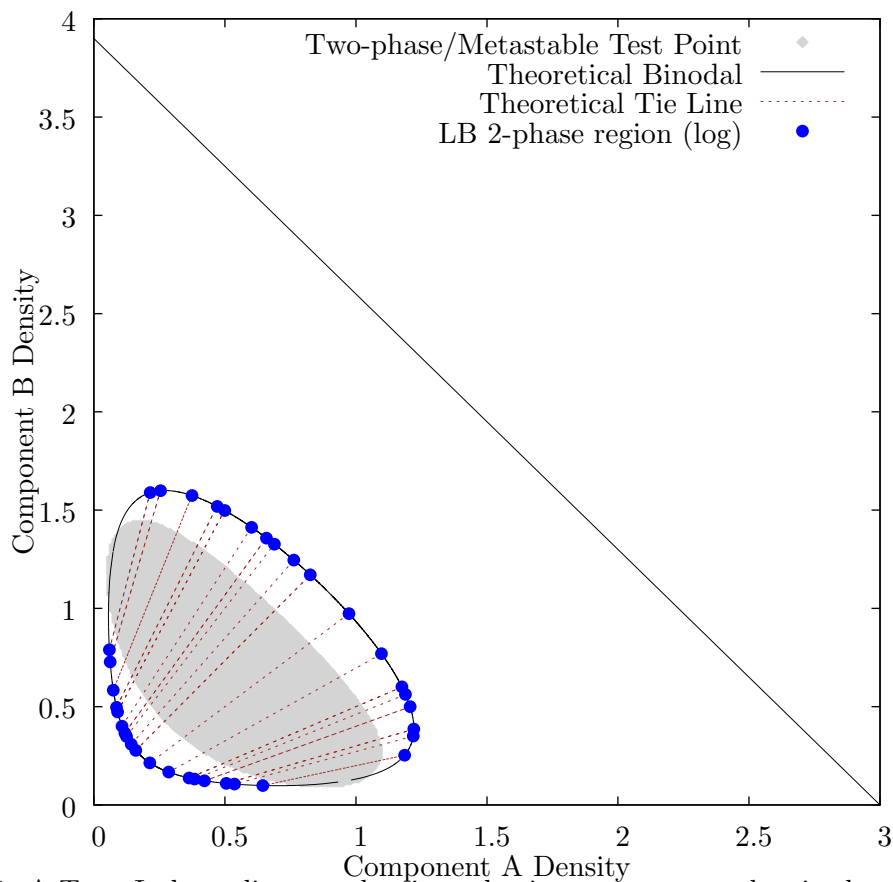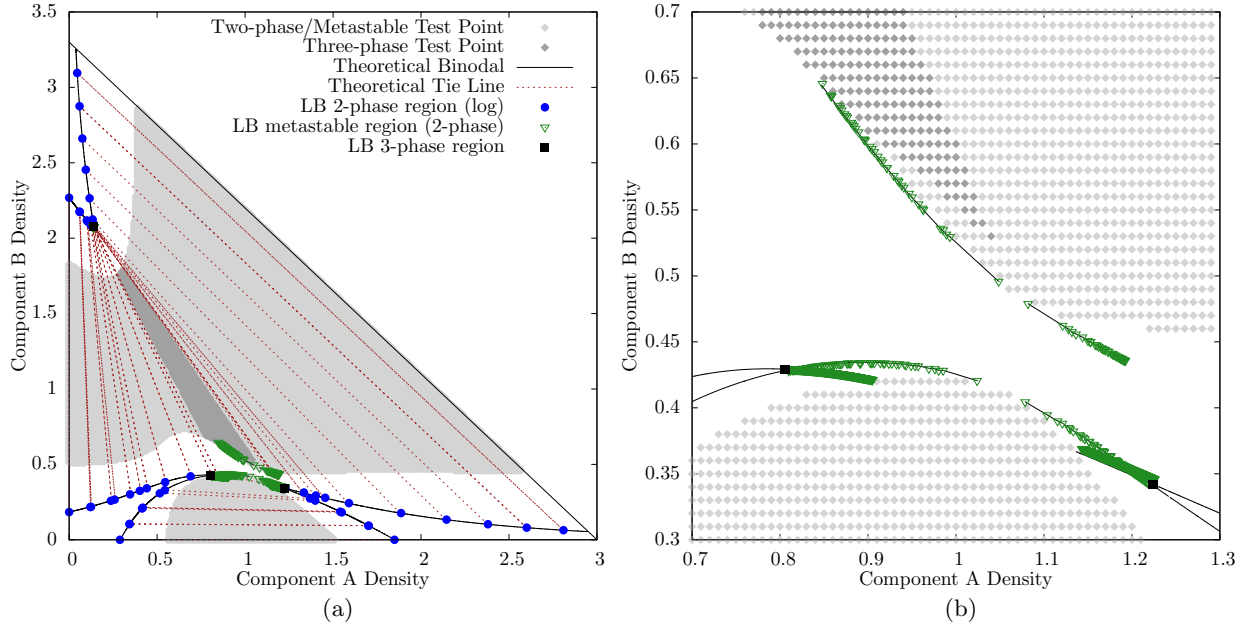
Figure 6.11. A Type II phase diagram showing a lattice temperature that is below the asymmetric critical temperatures of the two components ($\theta < \theta_c^A < \theta_c^B$) and asymmetric critical densities ($\rho_c^A < \rho_c^B$); the interaction parameter is repulsive. The full phase diagram is shown in (a) for a mixture where the component asymmetries have produced an auxiliary binodal for the metastable region of the phase diagram. A zoomed in view of the auxiliary binodals in (b) also clearly shows the miscibility gap within the 3-phase region. This phase diagram was generated using parameters of $\theta_c^A = 0.4$, $\theta_c^B = 0.45$, $\rho_c^B = 1.1$, and $\nu = 0.5$ ($\xi = -0.047619, \zeta = 0.106145, \Lambda = 0.502825$). Unlike the rest of the phase diagrams shown, the metastable and 3-phase LB simulations were done with $\kappa^{cc'} = 0.2$. One point $(0.0,1.0)$ used the single-component value of $\kappa^{cc'} = 2$.

the apex of the A-liquid-vapor area and another at the bottom of the three phase region that is defined by two new, short binodal line segments. The miscibility gap within the 3-phase region is expected in the context of Korteweg's work (this phenomenon was demonstrated for a symmetrical case); however, the formation of accessory plaits that are encapsulated within the 3-phase region was entirely unexpected [3, 27]. Although this situation is firmly entrenched in the global phase diagram for binary VDW mixtures, we have not been able to find another example of this specific behavior.

6.1.2.3. Shield Region

The shield region depicted in the upper, center of Figure 3.6 encloses a zone where 4-phase behavior between two VDW fluids is theoretically possible. The transition through this regions was first described by Korteweg using the tools of differential geometry, and his phase diagrams were

replicated by computational means following the work of Scott and van Konynenburg [3]. One of our goals was to replicate this process using lattice Boltzmann and to obtain a stable LB simulation of 2-component, 4-phase behavior. The general strategy was to use the center of the shield region as identified by [4] ($\zeta = 0, \Lambda = 0.4364$) and gradually increase the critical temperatures of the components (i.e. a deeper quench). Although we fell short of observing 4-phase behavior, we found that the simple D1Q3 model was still able to replicate the transition through the shield region extraordinarily well. Note that the description and phase diagrams in this subsection are all for symmetric components.

Our exploration of the shield region started by creating a phase diagram with $\theta_c = 0.4$ for both the A- and B-components, which yielded a phase diagram remarkably similar to the case shown in Figure 6.9. We then increased the critical temperatures in small, uniform increments (i.e. equal changes to θ_c^A, θ_c^B) to "quench" the mixture temperature even farther below the critical temperatures. As the quench became deeper, each region of the phase diagram developed independent 3-phase behavior with associated metastable accessory plaits. The critical points of each accessory plait eventually coincide, and the phase diagram regions merge, which isolates a "bubble" of single-phase behavior in the middle of the phase diagram. This is shown in Figure 6.12. In a perfectly symmetrical case such as what we were attempting to model, Korteweg predicted the merging of all critical points would be simultaneous. We note a slight discrepancy in that the binary liquid region of our phase diagrams showed 3-phase behavior slightly before the other 2 regions, and as a consequence the critical point merger was - although very close - not simultaneous as expected.

Figure 6.12 shows three independent 3-phase regions, and when initialized in near-equilibrium profiles, the LB simulations hold the predicted three-phase densities for all three regions well. The three-phase regions are separated by regions of 2-phase behavior that form shortly after the critical point merger. The majority of these 2-phase points are not bound by a three-phase region and are thus not expected to exhibit metastable behavior, and the LB simulations show that the tie lines are followed as predicted.

Further increase of the critical temperatures brings us closer to the theoretical 4-phase behavior, and the first sign of this is when the densities associated with 3-phase behavior coalesce into a single set (Figure 6.13). The independence of the separate three-phase regions is lost, yet they are still separated by ribbons of 2-phase metastable behavior. The single-phase bubble shrinks in
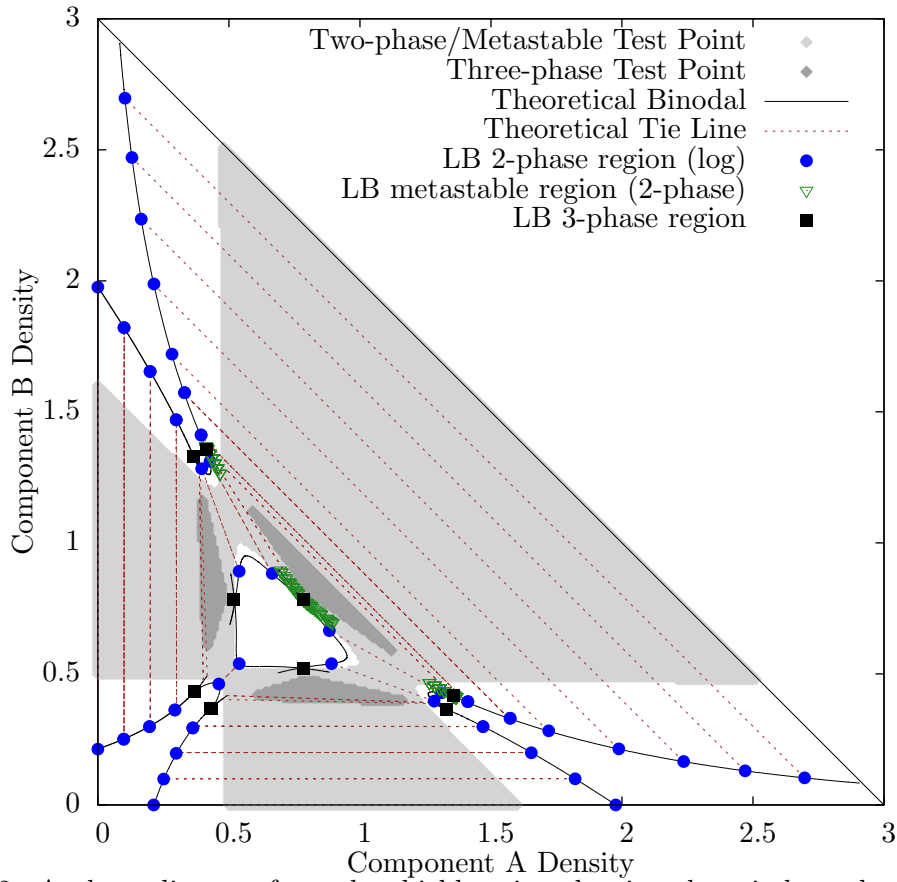
Figure 6.12. A phase diagram from the shield region showing three independent 3-phase regions shortly after the accessory plaits from each region connect. The single-phase region in the middle is fully enclosed and contains binodal segments that are very nearly continuous mediate the 2-phase regions separating each 3-phase region. The intermediary 2-phase regions contain points where metastable behavior would not be anticipated. This phase diagram was generated using parameters of $\theta_c^A = \theta_c^B = 0.427$, $\rho_c^B = 1.0$, and $\nu = 0.5636$ ($\xi = 0.0, \zeta = 0.0, \Lambda = 0.4364$). The metastable and 3-phase LB simulations were done with $\kappa^{cc'} = 0.2$, and we only show the metastable results associated with one 3-phase region to more clearly depict the binodal segments elsewhere.

size, which slowly zeroes in on the expected density of the fourth phase. Curiously, the tie lines that define the metastable 2-phase ribbons have endpoints that retreat closer to the 3-phase densities. This is shown in better detail in Figure 6.13c.

In Figure 6.13c, we see that the metastable 2-phase tie line stops short of the 3-phase density (defined by the intersecting binodals) to define a new, tiny binodal segment. This tiny binodal has a very noticeable affect on the LB simulations of the metastable 2-phase points along the main binodal lines, which we outline in Figure 6.13d. Starting from the simulations near the binodal intersection, the LB simulations recover the expected metastable 2-phase behavior. As the
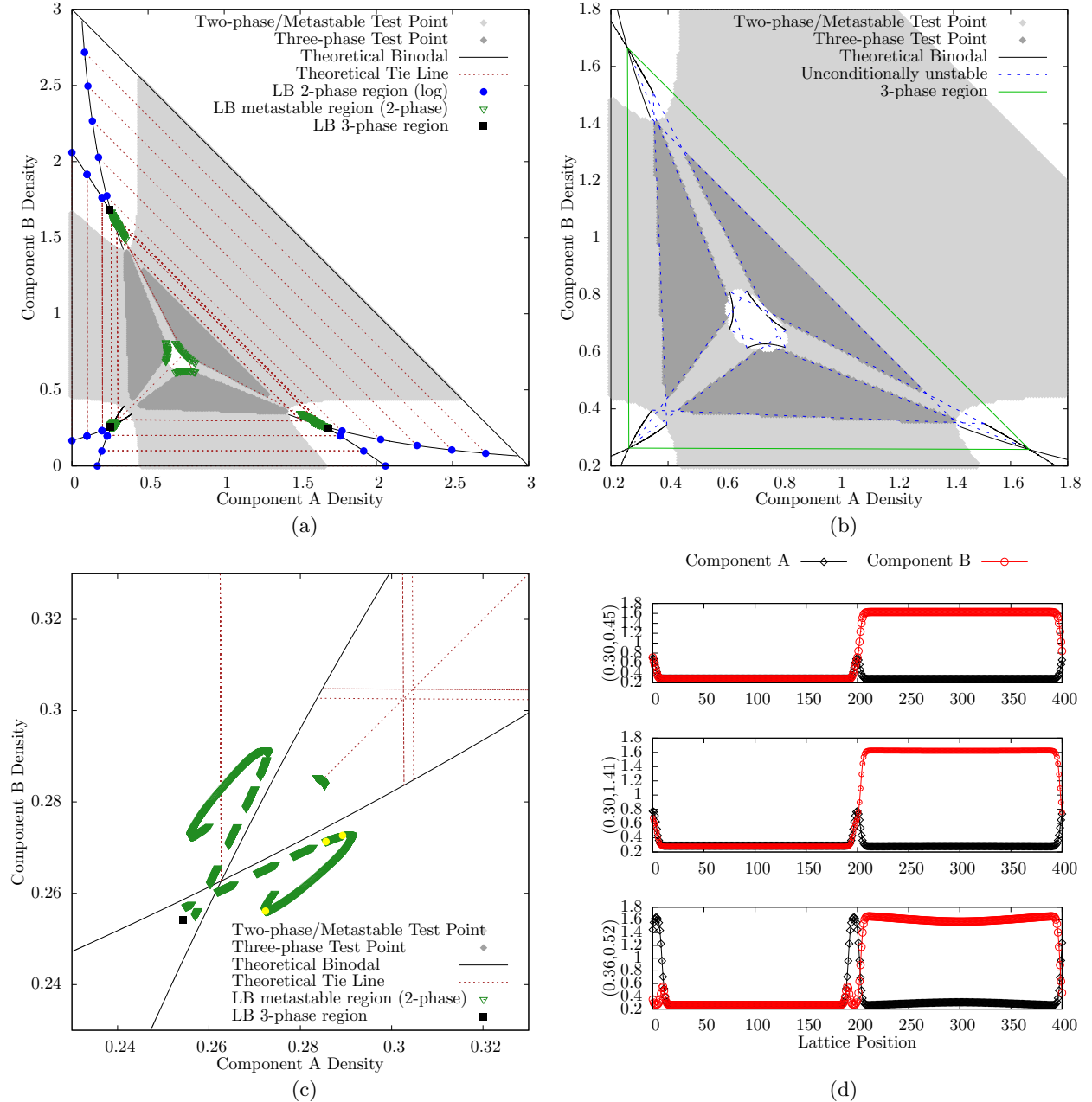
Figure 6.13. A phase diagram from the shield region progressing to theoretical 4-phase behavior. Part (a) shows regions of unconditionally unstable 3-phase behavior, but the once-independent sets of densities have coalesced into a single shared set. The intermediary 2-phase regions are now completely defined by metastability. Part (b) shows that the binodals in the middle single-phase region have broken apart into three independent segments. This phase diagram was generated using parameters of $\theta_c^A = \theta_c^B = 0.45$, $\rho_c^B = 1.0$, and $\nu = 0.5636$ ($\xi = 0.0, \zeta = 0.0, \Lambda = 0.4364$). The metastable and 3-phase LB simulations were done with $\kappa^{cc'} = 0.2$. Part (c) highlights the lower, left 3-phase density of (a). The 3-phase LB simulations exhibit the same consistency as seen in previous simulations; however, the metastable simulations lose track of their respective binodals. Part (d) shows a series of LB simulations that follow the curve of metastable results. Moving clockwise around the curve, the three yellow circle symbols in (c) correspond to lattice site 100 in the simulations shown in (d) from top to bottom, respectively.

simulations reach abeam the tiny binodal segment, the third of the three 3-phase densities begins to emerge. although the new domain doesn't fully form, it nonetheless has the effect of deflecting the LB results away from the binodal lines and back towards the binodal intersection. This is our only example where the LB simulations did not acceptably recover theoretical expectations.

6.1.3. Three van der Waals Fluids

To demonstrate the extensibility of our method, we implemented a LB simulation of a 3-component mixture of non-ideal fluids. Since our LB implementation was designed to simulate each component in its own right rather than order parameter-style relationships, the extension was little more than a simple copy/paste operation in code. Nothing else had to be derived for implementation, and we made zero changes to the corrections for thermodynamic consistency that we used in the two-component case. Figure 6.14 shows a representative case of this model extension.
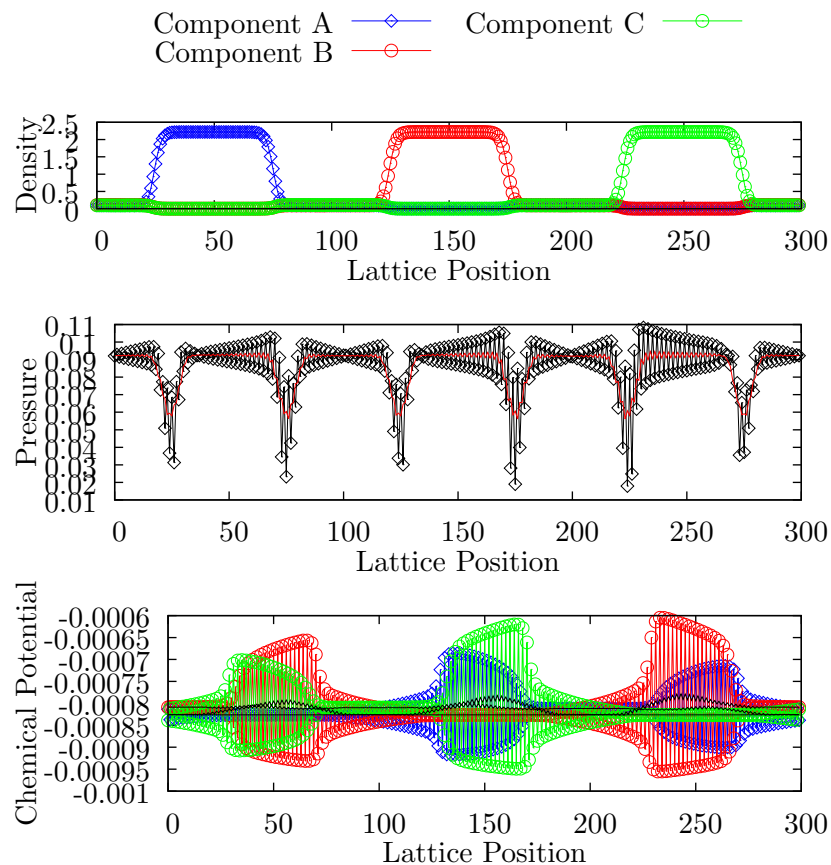

Figure 6.14. Simulation results from a 3-component simulation for the initial A,B,C components set (1.0, 1.0, 1.0), which exhibits thermodynamically consistent 4-phase equilibrium. We use parameters $\theta_c^A = \theta_c^B = \theta_c^C = 0.5$, $\rho_c^B = \rho_c^C = 1.0$, $\nu = 0.05$, and $\kappa^{cc'c''} = 2.0$.

The LB simulation shown in Figure 6.14 was initialized with a near-equilibrium density profile and parameters manually tuned to assure stability for at least 1,000,000 iterations. The top view of the density profile shows a stable density ratio of ~ 1700. The 2nd and 3rd panels are the pressure and chemical potentials, respectively. Filtered values are plotted on top of the noisy raw profiles to show the bulk pressure is constant to 10^{-4} and constant chemical potentials to 10^{-5}. Other simulations with lower equilibrium density ratios showed pressure and chemical potentials that were constant to 10^{-6}.

6.2. Summary and Outlook

We have demonstrated a LB method that is based on the minimization of a free energy function for a mixture of an arbitrary number of VDW fluids. The corrections to single-component simulations proposed earlier by Wagner [22] were applied to this method. With these corrections applied, our method was shown to recover consistent and accurate thermodynamics across a wide range of symmetric and asymmetric two-component fluid mixtures. We also demonstrated that it is very easily extended to simulate mixtures of three or more non-ideal fluid mixtures with equally consistent and accurate thermodynamic consistency.

Our discrete free energy was formulated in a manner reminiscent of the pseudopotential methods of Shan and Doolen [10]. This allowed us to identify the interaction strength ψ in terms of other commonly used non-ideal interaction variables. We also showed that this formulation can help reveal an appropriate choice of gradient stencil.

The numerical stability of our simulations was greatly improved with only a basic application of the findings of Pooley and Wagner [24]. Using the common methods of implementing numerical parameters to tune interface and forcing strength led to phase separation with standard density ratios on the order of ~ 20. But by ensuring the widths of phase interfaces in our initialized density profiles were at or above a minimum threshold, we were able to easily obtain density ratios over 150. Further manual optimization of our parameters combined with ensuring a minimum initial interface with resulted in a density ratio of over 1700.

In all cases, our LB simulation results recover all features of our phase diagrams very well. Since our free energy minimization doesn't account for interface effects, the majority of our LB simulations do not lie exactly at the ends of the theoretical tie lines. But most simulations show a 10^{-4} or less deviation from a binodal line after only 50,000 iterations. Occasionally the error

increases to 10^{-3}, but allowing simulations to run past our iteration cap to reach full equilibrium shows that the error gradually shrinks as material diffuses among phases.

The incredible phase diagram complexity that a simple binary van der Waals mixture can exhibit was known over a century ago to van der Waals, Korteweg, and their Dutch contemporaries. The history of their discovery [3, 27] and the relatively recent treatment by Meijer [32, 33] proved to be very enlightening. We were extremely pleased to learn that for such a simple LB model that included only three discrete lattice velocities, the simulations were able to replicate such a rich set of phase diagram features with outstanding accuracy.

Future extensions of this LB model would obviously expand to two- and three-dimension lattices. They may also implement a multiple relation scheme and other free energy functionals that would more accurately model a realistic multicomponent mixture. Expanding the analysis from the bulk to account for interfacial effects would further increase accuracies. Investigations that add fluctuations to this method may also be able to collapse our metastable 2-phase LB results to more well-defined 3-phase behavior.

REFERENCES

[1] David Johnston. *Advances in Thermodynamics of the van der Waals Fluid.* Morgan & Claypool Publishers, 2014.

[2] S. M. Blinder. Van der waals isotherms, Feb 2008.

[3] J.M.H.L. Sengers. *How Fluids Unmix: Discoveries by the School of Van Der Waals and Kamerlingh Onnes.* History of science and scholarship in the Netherlands. Edita, 2002.

[4] Robert L. Scott. Models for phase equilibria in fluid mixtures. *Accounts of Chemical Research*, 20(3):97–107, 1987.

[5] C. M. Pooley, Anna C. Balazs, and J. M. Yeomans. Pattern formation arising from condensation of a homogeneous gas into a binary, phase-separating liquid. *Phys. Rev. E*, 72:021505, Aug 2005.

[6] Joseph B Miller, Austin CP Usselman, Rebecca J Anthony, Uwe R Kortshagen, Alexander J Wagner, Alan R Denton, and Erik K Hobbie. Phase separation and the 'coffee-ring'effect in polymer–nanocrystal mixtures. *Soft Matter*, 10(11):1665–1675, 2014.

[7] Guy R McNamara and Gianluigi Zanetti. Use of the boltzmann equation to simulate lattice-gas automata. *Physical review letters*, 61(20):2332, 1988.

[8] Andrew K Gunstensen, Daniel H Rothman, Stéphane Zaleski, and Gianluigi Zanetti. Lattice boltzmann model of immiscible fluids. *Physical Review A*, 43(8):4320, 1991.

[9] Xiaowen Shan and Hudong Chen. Lattice boltzmann model for simulating flows with multiple phases and components. *Physical Review E*, 47(3):1815, 1993.

[10] Xiaowen Shan and Gary Doolen. Multicomponent lattice-boltzmann model with interparticle interaction. *Journal of Statistical Physics*, 81(1-2):379–393, oct 1995.

[11] S. Arcidiacono, J. Mantzaras, S. Ansumali, I. V. Karlin, C. Frouzakis, and K. B. Boulouchos. Simulation of binary mixtures with the lattice boltzman method. *Phys. Rev. E*, 74:056707, Nov 2006.

[12] S. Arcidiacono, I. V. Karlin, J. Mantzaras, and C. E. Frouzakis. Lattice boltzmann model for the simulation of multicomponent mixtures. *Phys. Rev. E*, 76:046703, Oct 2007.

[13] A. Mazloomi M, S. S. Chikatamarla, and I. V. Karlin. Entropic lattice boltzmann method for multiphase flows. *Phys. Rev. Lett.*, 114:174502, May 2015.

[14] Xiaowen Shan et al. Multicomponent lattice boltzmann model from continuum kinetic theory. *Physical Review E*, 81(4):045701, 2010.

[15] Pietro Asinari. Multiple-relaxation-time lattice boltzmann scheme for homogeneous mixture flows with external force. *Phys. Rev. E*, 77:056706, May 2008.

[16] Pietro Asinari. Lattice boltzmann scheme for mixture modeling: Analysis of the continuum diffusion regimes recovering maxwell-stefan model and incompressible navier-stokes equations. *Phys. Rev. E*, 80:056701, Nov 2009.

[17] Li-Shi Luo and Sharath S. Girimaji. Theory of the lattice boltzmann method: Two-fluid model for binary mixtures. *Phys. Rev. E*, 67:036302, Mar 2003.

[18] Michael R. Swift, W. R. Osborn, and J. M. Yeomans. Lattice boltzmann simulation of nonideal fluids. *Phys. Rev. Lett.*, 75:830–833, Jul 1995.

[19] Michael R. Swift, E. Orlandini, W. R. Osborn, and J. M. Yeomans. Lattice boltzmann simulations of liquid-gas and binary fluid systems. *Phys. Rev. E*, 54:5041–5052, Nov 1996.

[20] A. Lamura, G. Gonnella, and J. M. Yeomans. A lattice boltzmann model of ternary fluid mixtures. *EPL (Europhysics Letters)*, 45(3):314, 1999.

[21] Ciro Semprebon, Timm Krüger, and Halim Kusumaatmaja. Ternary free-energy lattice boltzmann model with tunable surface tensions and contact angles. *Phys. Rev. E*, 93:033305, Mar 2016.

[22] A. J. Wagner. Thermodynamic consistency of liquid-gas lattice boltzmann simulations. *Phys. Rev. E*, 74:056703, Nov 2006.

[23] Qun Li and A. J. Wagner. Symmetric free-energy-based multicomponent lattice boltzmann method. *Phys. Rev. E*, 76:036701, Sep 2007.

[24] AJ Wagner and CM Pooley. Interface width and bulk stability: Requirements for the simulation of deeply quenched liquid-gas systems. *Physical Review E*, 76(4):045702, 2007.

[25] Peter Henry van Konynenburg. *Critical lines and phase equilibria in binary mixtures.* PhD thesis, 1968.

[26] P. H. van Konynenburg and R. L. Scott. Critical lines and phase equilibria in binary van der waals mixtures. *Philosophical Transactions of the Royal Society of London A: Mathematical, Physical and Engineering Sciences*, 298(1442):495–540, 1980.

[27] Johanna Levelt Sengers and Antonius H. M. Levelt. Diederik korteweg, pioneer of criticality. *Physics Today*, 55(12):47–53, Dec 2002.

[28] Paul H. E. Meijer. The van der waals equation of state around the van laar point. *The Journal of Chemical Physics*, 90(1):448–456, 1989.

[29] Paul H.E. Meijer, Ian L. Pegg, Jonathan Aronson, and Mustafa Keskin. The critical lines of the van der waals equation for binary mixtures around the van laar point. *Fluid Phase Equilibria*, 58(1):65 – 80, 1990.

[30] Paul H. E. Meijer. Generalized korteweg equations for phase separation near the critical point in binary gas–liquid mixtures. *The Journal of Chemical Physics*, 101(6):5140–5147, 1994.

[31] Paul H.E. Meijer. Theory of coexisting states: calculation of binodals. *Physica A: Statistical Mechanics and its Applications*, 237(1):31 – 44, 1997.

[32] Paul H. E. Meijer. Metamorphosis from lcep to ucep in the metastable three-phase region. *The Journal of Physical Chemistry B*, 103(24):5084–5091, 1999.

[33] Paul H.E Meijer. The metamorphosis from LCEP to UCEP in the metastable three-phase region in type v phase-diagrams. *Fluid Phase Equilibria*, 158-160:575–582, jun 1999.

[34] George Jackson. Liquid State Theory: Statistical Mechanics of Liquids and Complex Fluids. (Online; multiple accesses).

[35] F. Reif. *Fundamentals of statistical and thermal physics.* McGraw-Hill series in fundamentals of physics. McGraw-Hill, 1965.

[36] D. Chandler. *Introduction to Modern Statistical Mechanics*. Oxford University Press, 1987.

[37] D. Henderson. *Fundamentals of Inhomogeneous Fluids*. Taylor & Francis, 1992.

[38] Alexander Wagner. *Theory and applications of the lattice Boltzmann method*. PhD thesis, University of Oxford, 1997.

[39] Arthur JM Yang, Paul D Fleming III, and Julian H Gibbs. Molecular theory of surface tension. *The Journal of Chemical Physics*, 64(9):3732–3747, 1976.

[40] H.B. Callen. *Thermodynamics and an Introduction to Thermostatistics*. Wiley, 1985.

[41] JJ van Laar. An exact expression for the course of the spinodal curves and their of plaitpoints for all temperatures, in the case of mixture of normal substances. *Koninklijke Nederlandse Akademie van Wetenschappen Proceedings Series B Physical Sciences*, 7:646–657, 1904.

[42] E. H. Benmekki, T. Y. Kwak, and G. A. Mansoori. *Van der Waals Mixing Rules for Cubic Equations of State*, chapter 9, pages 101–114. American Chemical Society, 1987.

[43] Eric Merlin Foard. *A numerical and analytical analysis of the physics of phase-separation fronts*. PhD thesis, North Dakota State University, 2012.

[44] E.H. Chimowitz. *Introduction to Critical Phenomena in Fluids*. Topics in Chemical Engineering. Oxford University Press, 2005.

[45] William H. Press, Brian P. Flannery, Saul A. Teukolsky, and William T. Vetterling. *Numerical Recipes in C: The Art of Scientific Computing, Second Edition*. Cambridge University Press, 1992.

[46] K. S. Ridl and A. J. Wagner. D1Q3 Thesis/Publication Code & Research Data, 2018. DOI: https://doi.org/10.5281/zenodo.1206330.

[47] J.D. Van Der Waals and J.S. Rowlinson. *On the Continuity of the Gaseous and Liquid States*. Dover Books on Physics Series. Dover Publications, 2004.

[48] JJ van Laar. On the shape of the plaitpoint curves for mixtures of normal substances. *Koninklijke Nederlandse Akademie van Wetenschappen Proceedings Series B Physical Sciences*, 8:33–48, 1905.

[49] T. Krüger, H. Kusumaatmaja, A. Kuzmin, O. Shardt, G. Silva, and E.M. Viggen. *The Lattice Boltzmann Method: Principles and Practice.* Graduate Texts in Physics. Springer International Publishing, 2016.

[50] K. Huang. *Statistical Mechanics.* Wiley, 1987.

[51] Frank C. van den Bosch. Physical Processes in Astronomy. (Online; multiple accesses).

[52] Steven R. Cranmer. Astr-5120, fall 2016, radiative and dynamical processes. (Online; multiple accesses).

[53] K. Huang. *Introduction to Statistical Physics.* Taylor & Francis, 2001.

[54] David Tong. David tong: Lectures on kinetic theory, 2012. (Online; multiple accesses).

[55] Alexander J Wagner. A practical introduction to the lattice boltzmann method. 2008.

[56] J.A. Bittencourt. *Fundamentals of Plasma Physics.* Springer New York, 2004.

[57] Erlend Magnus Viggen. *The lattice Boltzmann method: Fundamentals and acoustics.* PhD thesis, 2014.

[58] K. Strand. Moment Independent Expansion for Fourth-Order Corrections in Lattice Boltzmann Methods. *ArXiv e-prints*, October 2017.

[59] Sumesh P. Thampi, Santosh Ansumali, R. Adhikari, and Sauro Succi. Isotropic discrete laplacian operators from lattice hydrodynamics. *Journal of Computational Physics*, 234:1 – 7, 2013.

[60] Alexander J. Wagner, Stephan Loew, and Sylvio May. Influence of monolayer-monolayer coupling on the phase behavior of a fluid lipid bilayer. *Biophysical Journal*, 93(12):4268 – 4277, 2007.

[61] Goetz August Kaehler. *Fluctuations in the lattice Boltzmann method.* PhD thesis, North Dakota State University, 2012.

[62] E. Orlandini, M. R. Swift, and J. M. Yeomans. A lattice boltzmann model of binary-fluid mixtures. *EPL (Europhysics Letters)*, 32(6):463, 1995.

[63] A. Lamura, G. Gonnella, and J. M. Yeomans. A lattice boltzmann model of ternary fluid mixtures. *EPL (Europhysics Letters)*, 45(3):314, 1999.

[64] Xiaowen Shan and Hudong Chen. Simulation of nonideal gases and liquid-gas phase transitions by the lattice boltzmann equation. *Physical Review E*, 49(4):2941, 1994.

[65] Junfeng Zhang, Baoming Li, and Daniel Y. Kwok. Mean-field free-energy approach to the lattice boltzmann method for liquid-vapor and solid-fluid interfaces. *Physical Review E*, 69(3), mar 2004.

[66] David Keffer. The Statistical Mechanical Derivation of the van der Waals Equation of State for a multicomponent fluid and its associated thermodynamic properties. (Online; multiple accesses).

APPENDIX A.   PARTITION FUNCTION EXPANSION FOR A

MIXTURE OF TWO VAN DER WAALS FLUIDS

The components are A and B with N_A and N_B particles of each component respectively. And in an odd contradition to the expansion that follows, we omit the interfacial terms ($\kappa = 0$) for "brevity."

$$Z_{VDW2} = \frac{(V - N_A b_A - N_B b_B)^{N_A}}{\Lambda^{3N_A} N_A!} e^{\frac{N_A(N_A a_A + N_B a_{AB})}{V k_B T}} \frac{(V - N_A b_A - N_B b_B)^{N_B}}{\Lambda^{3N_B} N_B!} e^{\frac{N_B(N_B a_B + N_A a_{AB})}{V k_B T}}$$

(A.1)

$$
\begin{aligned}
lnZ_{VDW2} =& N_A ln(V - N_A b_A - N_B b_B) - ln(\Lambda^{3N_A} N_A!) + \frac{N_A(N_A a_A + N_B a_{AB})}{V k_B T} \\
& + N_B ln(V - N_A b_A - N_B b_B) - ln(\Lambda^{3N_B} N_B!) + \frac{N_B(N_B a_B + N_A a_{AB})}{V k_B T} \\
=& (N_A + N_B) ln(V - N_A b_A - N_B b_B) + \frac{N_A^2 a_A + 2 N_A N_B a_{AB} + N_B^2 a_B}{V k_B T} \\
& - 3 N_A ln\Lambda - 3 N_B ln\Lambda - lnN_A! - lnN_B! \\
=& (N_A + N_B) ln\left(\frac{V - N_A b_A - N_B b_B}{\Lambda^3}\right) + \frac{N_A^2 a_A + 2 N_A N_B a_{AB} + N_B^2 a_B}{V k_B T} \\
& - N_A lnN_A + N_A - N_B lnN_B + N_B \\
lnZ_{VDW2} =& N_A ln\left(\frac{V - N_A b_A - N_B b_B}{N_A \Lambda^3}\right) + N_B ln\left(\frac{V - N_A b_A - N_B b_B}{N_B \Lambda^3}\right) \\
& + \frac{N_A^2 a_A}{V k_B T} + \frac{2 N_A N_B a_{AB}}{V k_B T} + \frac{N_B^2 a_B}{V k_B T} + N_A + N_B
\end{aligned}
$$

$$F = -k_B T ln Z_{VDW2}$$

$$= -k_B T N_A ln\left(\frac{V - N_A b_A - N_B b_B}{N_A \Lambda^3}\right) - \frac{N_A^2 a_A}{V} - k_B T N_A$$

$$- k_B T N_B ln\left(\frac{V - N_A b_A - N_B b_B}{N_B \Lambda^3}\right) - \frac{N_B^2 a_B}{V} - k_B T N_B$$

$$- \frac{2 N_A N_B a_{AB}}{V}$$

$$\mu_A = -k_B T \frac{\partial ln Z_{VDW2}}{\partial N_A}$$

$$= -k_B T ln\left(\frac{V - N_A b_A - N_B b_B}{N_A \Lambda^3}\right)$$

$$- k_B T N_A \frac{N_A \Lambda^3}{V - N_A b_A - N_B b_B} \frac{(-b_A)(N_A \Lambda^3) - (V - N_A b_A - N_B b_B)(\Lambda^3)}{N_A^2 \Lambda^6}$$

$$- k_B T N_B \frac{N_B \Lambda^3}{V - N_A b_A - N_B b_B} \frac{(-b_A)(N_B \Lambda^3) - \cancel{(V - N_A b_A - N_B b_B)(0)}}{N_B^2 \Lambda^6}$$

$$- k_B T (1 + \cancel{0}) - \frac{2 N_A a_A}{V} - \frac{2 N_B a_{AB}}{V} - \cancel{0}$$

$$= -k_B T ln\left(\frac{V - N_A b_A - N_B b_B}{N_A \Lambda^3}\right) - \frac{k_B T N_A^{\cancel{3}}(-b_A)\cancel{\Lambda^6}}{\cancel{N_A^2 \Lambda^6}(V - N_A b_A - N_B b_B)}$$

$$+ \frac{k_B T \cancel{N_A^2 (V - N_A b_A - N_B b_B)\Lambda^6}}{\cancel{N_A^2 \Lambda^6 (V - N_A b_A - N_B b_B)}} - \frac{k_B T N_B^{\cancel{3}}(-b_A)\cancel{\Lambda^6}}{\cancel{N_B^2 \Lambda^6}(V - N_A b_A - N_B b_B)}$$

$$- k_B T - \frac{2 N_A a_A}{V} - \frac{2 N_B a_{AB}}{V}$$

$$= -k_B T ln\left(\frac{V - N_A b_A - N_B b_B}{N_A \Lambda^3}\right) + \frac{k_B T N_A b_A}{(V - N_A b_A - N_B b_B)} + \cancel{k_B T}$$

$$+ \frac{k_B T N_B b_A}{(V - N_A b_A - N_B b_B)} \cancel{- k_B T} - \frac{2 N_A a_A}{V} - \frac{2 N_B a_{AB}}{V}$$

$$\mu_A = k_B T ln\left(\frac{N_A \Lambda^3}{V - N_A b_A - N_B b_B}\right) + \frac{k_B T b_A (N_A + N_B)}{(V - N_A b_A - N_B b_B)} - \frac{2 N_A a_A}{V} - \frac{2 N_B a_{AB}}{V}$$

$$\therefore \mu_B = -k_B T \frac{\partial ln Z_{VDW2}}{\partial N_B}$$

$$= k_B T ln\left(\frac{N_B \Lambda^3}{V - N_A b_A - N_B b_B}\right) + \frac{k_B T b_B (N_A + N_B)}{(V - N_A b_A - N_B b_B)} - \frac{2 N_B a_B}{V} - \frac{2 N_A a_{AB}}{V}$$

$$P = k_B T \frac{\partial ln Z_{VDW2}}{\partial V}$$

$$= N_A k_B T \frac{\cancel{N_A A^3}}{V - N_A b_A - N_B b_B} \frac{1}{\cancel{N_A A^3}} + N_B k_B T \frac{\cancel{N_B A^3}}{V - N_A b_A - N_B b_B} \frac{1}{\cancel{N_B A^3}}$$

$$- \frac{2 N_A a_A}{V^2} - \frac{2 N_A N_B a_{AB}}{V^2} - \frac{2 N_B a_B}{V^2}$$

$$P = \frac{N_A k_B T}{V - N_A b_A - N_B b_B} - \frac{2 N_A a_A}{V^2} + \frac{N_B k_B T}{V - N_A b_A - N_B b_B} - \frac{2 N_B a_B}{V^2} - \frac{2 N_A N_B a_{AB}}{V^2}$$

APPENDIX B. MULTICOMPONENT PRESSURE TENSOR
CONSTRUCTION

In a multicomponent system with non-ideal interactions, the pressure gradient no longer provides the phase separation forcing in a thermodynamically consistent manner. This necessitates a change to the use of a chemical potential gradient. The Gibbs-Duhem relation is used to enforce thermodynamic consistency.

The pressure tensor for the multicomponent system is constructed by dividing the bulk thermodynamics from that at the interfaces. Similar to the iterative method used in Section 2.1.1.3.2 to develop the pressure interface terms for a single component, we apply an iterative method to develop the multicomponent pressure tensor. Unlike earlier, though, we show that the iterative method can also recover the bulk part of the pressure tensor.

B.1. Bulk Pressure

We start by applying the gradient operation explicitly in the Gibbs-Duhem relation. The pressure and chemical potentials are all functions of the densities of the components in the mixture ρ_c, so we use the chain rule to explicitly pull this dependence out

$$\nabla P = \sum_c \rho_c \nabla \mu_c \tag{B.1}$$

$$\sum_c \frac{\partial P}{\partial \rho_c} \nabla \rho_c = \sum_{c'} \rho_{c'} \sum_c \frac{\partial \mu_{c'}}{\partial \rho_c} \nabla \rho_c \tag{B.2}$$

Comparing coefficients of the $\sum_c \nabla \rho_c$ term, we can determine how to use the free energy (the functional derivative of which is the chemical potential μ) to help construct the expression for the bulk pressure

$$\frac{\partial P}{\partial \rho_c} = \sum_{c'} \rho_{c'} \frac{\partial \mu_{c'}}{\partial \rho_c} = \sum_{c'} \rho_{c'} \frac{\partial^2 \psi}{\partial \rho_{c'} \partial \rho_c} \tag{B.3}$$

Whatever the bulk pressure is, we now know it must satisfy this differential equation with the free energy. We can also integrate this expression over ρ_c and use it as the initial guess to build the

expression for the pressure

$$P \stackrel{?}{=} \sum_{c'} \rho_{c'} \frac{\partial \psi}{\partial \rho_{c'}} \tag{B.4}$$

$$\frac{\partial P}{\partial \rho_c} \stackrel{?}{=} \frac{\partial}{\partial \rho_c} \left(\sum_{c'} \rho_{c'} \frac{\partial \psi}{\partial \rho_{c'}} \right) \tag{B.5}$$

$$= \sum_{c'} \delta_{cc'} \frac{\partial F}{\partial \rho_{c'}} + \sum_{c'} \rho_{c'} \frac{\partial^2 \psi}{\partial \rho_{c'} \rho_c} \tag{B.6}$$

$$= \frac{\partial \psi}{\partial \rho_c} + \sum_{c'} \rho_{c'} \frac{\partial^2 \psi}{\partial \rho_{c'} \rho_c} \tag{B.7}$$

An extra term exists. The free energy derivative can be eliminated if we modify our bulk pressure to subtract the free energy

$$P \stackrel{?}{=} \sum_{c'} \rho_{c'} \frac{\partial \psi}{\partial \rho_{c'}} - \psi \tag{B.8}$$

$$\frac{\partial P}{\partial \rho_c} \stackrel{?}{=} \frac{\partial}{\partial \rho_c} \left(\sum_{c'} \rho_{c'} \frac{\partial \psi}{\partial \rho_{c'}} - \psi \right) \tag{B.9}$$

$$= \cancel{\frac{\partial \psi}{\partial \rho_c}} + \sum_{c'} \rho_{c'} \frac{\partial^2 \psi}{\partial \rho_{c'} \rho_c} - \cancel{\frac{\partial \psi}{\partial \rho_c}} \tag{B.10}$$

$$\frac{\partial P}{\partial \rho_c} = \sum_{c'} \rho_{c'} \frac{\partial^2 \psi}{\partial \rho_{c'} \rho_c} \tag{B.11}$$

The desired differential equation is recovered. Substituting the definition of the chemical potential (and re-labelling indices of summation), the bulk pressure for the multicomponent mixture is:

$$P = \sum_c \rho_c \mu_c - \psi \tag{B.12}$$

B.2. Interface Pressure

The multicomponent free energy density is written to include gradient terms at the interfaces between components ($\psi \rightarrow \frac{1}{2} \sum_{cc'} \kappa_{cc'} \nabla \rho_c \nabla \rho_{c'}$). These gradient terms also appear in the chemical

potentials of each component

$$\mu_c = -\frac{1}{2}\sum_{c'c''}\kappa_{c'c''}\delta_{cc'}\nabla^2\rho_{c''} - \frac{1}{2}\sum_{c'c''}\kappa_{c'c''}\delta_{cc''}\nabla^2\rho_{c'} \qquad \text{(partial integration)} \qquad \text{(B.13)}$$

$$= -\frac{1}{2}\sum_{c''}\kappa_{cc''}\nabla^2\rho_{c''} - \frac{1}{2}\sum_{c'}\kappa_{c'c}\nabla^2\rho_{c'} \qquad \qquad \text{(B.14)}$$

$$= -\frac{1}{2}\sum_{c'}(\kappa_{cc'} + \kappa_{c'c})\nabla^2\rho_{c'} \qquad \text{(relabel c'' = c')} \qquad \text{(B.15)}$$

$$\mu_c = -\sum_{c'}\kappa_{cc'}\nabla^2\rho_{c'} \qquad \qquad \text{(B.16)}$$

These are the gradient terms we use to construct the rest of the pressure tensor while demanding that Gibbs-Duhem holds ($\nabla_\beta P_{\alpha\beta} \overset{!}{=} \sum_c \rho_c \nabla_\alpha \mu_c$). Substituting in the above for the chemical potential in Gibbs-Duhem, we find

$$\sum_c \rho_c \nabla_\alpha \mu_c = -\sum_{cc'}\kappa_{cc'}\rho_c\nabla_\alpha\nabla^2\rho_{c'} \qquad \qquad \text{(B.17)}$$

which gives us a clue about the first term in the pressure tensor

$$P_{\alpha\beta} = -\sum_{cc'}\kappa_{cc'}\delta_{\alpha\beta}\rho_c\nabla^2\rho_{c'} \qquad \qquad \text{(B.18)}$$

Applying the gradient operation to this term reveals an extraneous term to be cancelled

$$\nabla_\beta P_{\alpha\beta} = -\nabla_\beta \sum_{cc'}\kappa_{cc'}\delta_{\alpha\beta}\rho_c\nabla^2\rho_{c'} \qquad \qquad \text{(B.19)}$$

$$= -\sum_{cc'}\kappa_{cc'}\nabla_\alpha\rho_c\nabla^2\rho_{c'} - \sum_{cc'}\kappa_{cc'}\rho_c\nabla_\alpha\nabla^2\rho_{c'} \qquad \qquad \text{(B.20)}$$

To produce a term that will cancel the first above but keep the second (which is the chemical potential portion of the Gibbs-Duhem relation we need to preserve), we modify the pressure tensor gradient terms to

$$P_{\alpha\beta} = -\sum_{cc'}\kappa_{cc'}\delta_{\alpha\beta}\rho_c\nabla^2\rho_{c'} + \sum_{cc'}\kappa_{cc'}\nabla_\alpha\rho_c\nabla_\beta\rho_{c'} \qquad \qquad \text{(B.21)}$$

The derivative of this new term modifies the pressure tensor gradient by

$$\nabla_\beta P_{\alpha\beta} = \nabla_\beta \left(-\sum_{cc'} \kappa_{cc'} \delta_{\alpha\beta} \rho_c \nabla^2 \rho_{c'} + \sum_{cc'} \kappa_{cc'} \nabla_\alpha \rho_c \nabla_\beta \rho_{c'} \right) \tag{B.22}$$

$$= -\cancel{\sum_{cc'} \kappa_{cc'} \nabla_\alpha \rho_c \nabla^2 \rho_{c'}} - \sum_{cc'} \kappa_{cc'} \rho_c \nabla_\alpha \nabla^2 \rho_{c'} \tag{B.23}$$

$$+ \sum_{cc'} \kappa_{cc'} \nabla_\alpha \nabla_\beta \rho_c \nabla_\beta \rho_{c'} + \cancel{\sum_{cc'} \kappa_{cc'} \nabla_\alpha \rho_c \nabla_\beta \nabla_\beta \rho_{c'}} \tag{B.24}$$

$$= -\sum_{cc'} \kappa_{cc'} \rho_c \nabla_\alpha \nabla^2 \rho_{c'} + \sum_{cc'} \kappa_{cc'} \nabla_\alpha \nabla_\beta \rho_c \nabla_\beta \rho_{c'} \tag{B.25}$$

The previous extraneous term has been eliminated (since $\nabla^2 \equiv \nabla_\beta \nabla_\beta$), but a new one remains. Another modification to the pressure and application of the gradient operation yields

$$P_{\alpha\beta} = -\sum_{cc'} \kappa_{cc'} \delta_{\alpha\beta} \rho_c \nabla^2 \rho_{c'} + \sum_{cc'} \kappa_{cc'} \nabla_\alpha \rho_c \nabla_\beta \rho_{c'} - \frac{1}{2} \sum_{cc'} \kappa_{cc'} \nabla_\gamma \rho_c \nabla_\gamma \rho_{c'} \delta_{\alpha\beta} \tag{B.26}$$

$$\nabla_\beta P_{\alpha\beta} = \nabla_\beta \left(-\sum_{cc'} \kappa_{cc'} \delta_{\alpha\beta} \rho_c \nabla^2 \rho_{c'} + \sum_{cc'} \kappa_{cc'} \nabla_\alpha \rho_c \nabla_\beta \rho_{c'} - \frac{1}{2} \sum_{cc'} \kappa_{cc'} \nabla_\gamma \rho_c \nabla_\gamma \rho_{c'} \delta_{\alpha\beta} \right) \tag{B.27}$$

$$= -\cancel{\sum_{cc'} \kappa_{cc'} \nabla_\alpha \rho_c \nabla^2 \rho_{c'}} - \sum_{cc'} \kappa_{cc'} \rho_c \nabla_\alpha \nabla^2 \rho_{c'} + \sum_{cc'} \kappa_{cc'} \nabla_\alpha \nabla_\beta \rho_c \nabla_\beta \rho_{c'} \tag{B.28}$$

$$+ \cancel{\sum_{cc'} \kappa_{cc'} \nabla_\alpha \rho_c \nabla_\beta \nabla_\beta \rho_{c'}} - \frac{1}{2} \sum_{cc'} \kappa_{cc'} \left(\nabla_\alpha \nabla_\gamma \rho_c \nabla_\gamma \rho_{c'} + \nabla_\gamma \rho_c \nabla_\alpha \nabla_\gamma \rho_{c'} \right) \tag{B.29}$$

$$= -\sum_{cc'} \kappa_{cc'} \rho_c \nabla_\alpha \nabla^2 \rho_{c'} + \cancel{\sum_{cc'} \kappa_{cc'} \nabla_\alpha \nabla_\beta \rho_c \nabla_\beta \rho_{c'}} - \frac{1}{2} \cancel{\sum_{cc'} 2\kappa_{cc'} \nabla_\alpha \nabla_\beta \rho_c \nabla_\beta \rho_{c'}} \quad (\text{relabel} \gamma \equiv \beta) \tag{B.30}$$

$$\nabla_\beta P_{\alpha\beta} = -\sum_{cc'} \kappa_{cc'} \rho_c \nabla_\alpha \nabla^2 \rho_{c'} \tag{B.31}$$

These gradient terms will satisfy the Gibbs-Duhem relation. Combining the bulk and interface pressures, we have the final multicomponent pressure tensor

$$P_{\alpha\beta} = \sum_c \rho_c \mu_c - \psi - \sum_{cc'} \kappa_{cc'} \left[\left(\rho_c \nabla^2 \rho_{c'} + \frac{1}{2} \nabla_\gamma \rho_c \nabla_\gamma \rho_{c'} \right) \delta_{\alpha\beta} - \nabla_\alpha \rho_c \nabla_\beta \rho_{c'} \right] \tag{B.32}$$

APPENDIX C. TWO-COMPONENT, FOUR-PHASE

BEHAVIOR ATTEMPT

By Gibbs' phase rule, our two-component mixture should be able to exist at a point where there are no remaining thermodynamic degrees of freedom. Such a point would necessarily exist in 4 phases.

In Figure C.1, the lines without symbols are the prepared density profile. Two liquid domains - one A-rich and the other B-rich - were prepared with a vapor phase separating them on one side and an intermediate density phase separating them on the other (the middle of the lattice). The numerical values of the densities for each phase were intialized as follows

$$rhoA1 = 1.896553132497407 \quad rhoB1 = 0.169151149061583$$

$$rhoA2 = 0.169150765439082 \quad rhoB2 = 1.896556831396832$$

$$rhoA3 = 0.172977697951899 \quad rhoB3 = 0.172978477952882$$

$$rhoA4 = 0.71 \quad rhoB4 = 0.71$$

When the simulation started, the initialized 4th phase immediately collapsed and tried to evolve into additional binary liquid domains. The new binary liquids all collapsed as the initial A- and B-rich phases migrated to the edges of the lattice and the initial vapor phase re-formed in the middle half of the lattice.
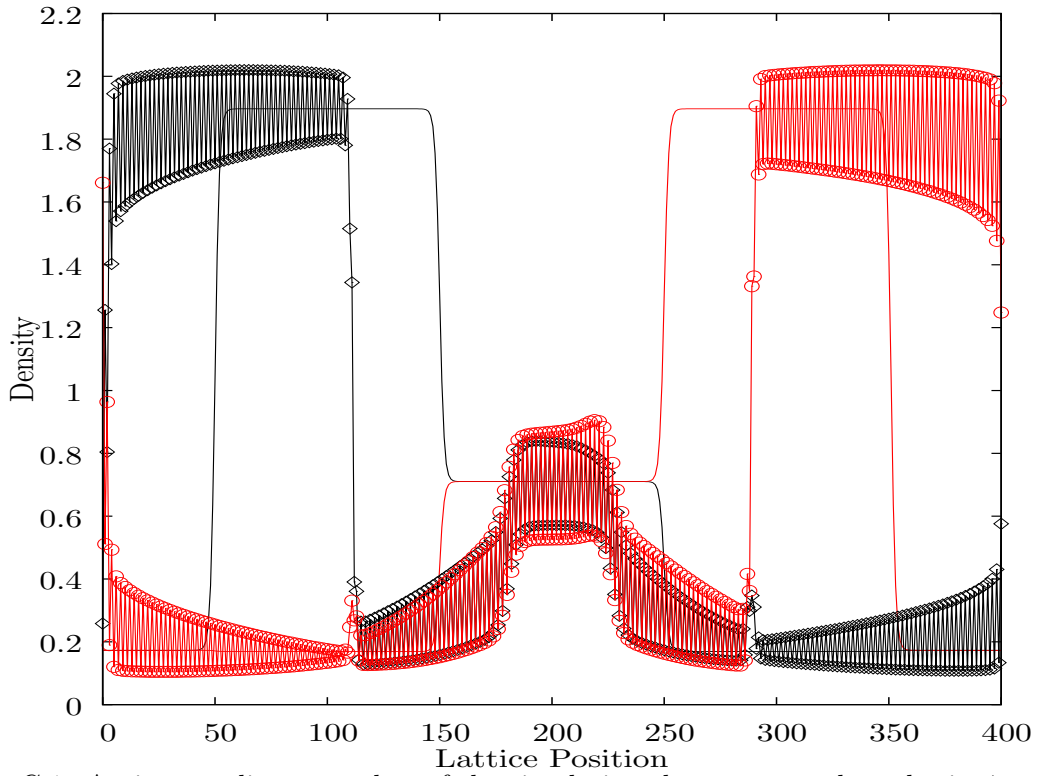
Figure C.1. An intermediate snapshot of the simulation that attempted to obtain 4 stable phases in a binary VDW mixture. We use parameters $\theta_c^A = \theta_c^B = 0.475$, $\rho_c^B = 1.0$, $\nu = 0.5636$, $\kappa^{cc'} = 0.2$, $\gamma_\mu = 0.1$, and an initial interface width equal to 2 lattice spaces.

The lines with symbols were captured at 550,000 iterations after the almost-4th phase spontaneously emerged as shown. The large noise amplitude kept the phases from ever fully forming, but the mid-point of the noise on top of the 4th phase is very near the anticipated theoretical density of that phase. The 4th phase held steady for about 100,000 iterations before the simulation destabilized.